FACULTY
OF MATHEMATICS
AND PHYSICS
Charles University

BACHELOR THESIS

Vendula Benešová

Hadron production in deep inelastic scattering of muons off protons at COMPASS experiment

Department of Low-Temperature Physics

Supervisor of the bachelor thesis: Mgr. Jan Matoušek Ph.D.
Study programme: Physics
Study branch: Physics

Prague 2023

I declare that I carried out this bachelor thesis independently, and only with the cited sources, literature and other professional sources. It has not been used to obtain another or the same degree.

I understand that my work relates to the rights and obligations under the Act No. 121/2000 Sb., the Copyright Act, as amended, in particular the fact that the Charles University has the right to conclude a license agreement on the use of this work as a school work pursuant to Section 60 subsection 1 of the Copyright Act.

In .... date ....

Author's signature

This thesis is dedicated to my parents, who have supported me through every step of my academic journey. Their unwavering love, guidance, and encouragement have been instrumental in helping me reach this milestone. I would also like to dedicate this thesis to my brother and friends, who have always been a source of inspiration and motivation for me.

In addition, I would like to express my deepest gratitude to my supervisor Jan Matoušek, whose valuable insights, guidance, and support have been indispensable in the completion of this work.

Thank you to all the individuals who have contributed to my education and growth, directly or indirectly. Your support has been crucial to my success, and I am forever grateful.

Title: Hadron production in deep inelastic scattering of muons off protons at COMPASS experiment

Author: Vendula Benešová

Department: Department of Low-Temperature Physics

Supervisor: Mgr. Jan Matoušek Ph.D., Department of Low-Temperature Physics

Abstract: The main goal of this thesis is to investigate azimuthal asymmetries in semi-inclusive deep inelastic scattering (SIDIS) of polarized muons on unpolarized nucleons using data collected by the COMPASS experiment at CERN. With a larger data sample than in previous studies, we aim towards reducing statistical errors of the results. To fully understand the azimuthal modulations, this thesis gives a brief introduction to the theory of the transverse momentum dependent parton distribution functions (TMD-PDFs). We describe SIDIS process as well as the COMPASS detector set-up for SIDIS measurements and examine the process of generating Monte Carlo simulations through beam file extraction studies. The results of our analysis contribute to ongoing efforts to better understand the quark-gluon structure of the nucleon, and the interplay between TMD-PDFs and azimuthal asymmetries in SIDIS.

Keywords: SIDIS DIS nucleon structure TMD-PDFs

Contents

Introduction

Whether nucleons are elementary particles or not has been questioned since Stern's experiments in 1932 revealed disagreement between experimentally measured and theoretical proton's magnetic moment [1]. Scattering experiments with high-energy lepton beams such as MIT-SLAC (experiment with an electron beam and unpolarized liquid hydrogen target) discovered that the electrical charge within the proton is concentrated in smaller components of negligible size. Leptons were chosen as projectiles over composite particles for being point-like which is a useful property that eliminates extra uncertainty in the data interpretation [2]. The nucleon's structure was unclear until theoreticians R.P. Feynman and J.D. Bjorken devised an interpretation – parton model. Partons were later identified with quarks from the Gell-Man's quark model.

Since then understanding the nucleon structure has become one of the main challenges in Quantum ChromoDynamics (QCD) and hadronic physics and as more and more powerful accelerators were built and different types of targets were used, the quark structure of nucleon was proven to be correct [3].

However, spin structure and full information about a parton inside a nucleon have not been solved analytically by the theory of standard model yet due to the diverging perturbation series. Recently, a non-perturbative approach — lattice QCD — has found success in calculating parton distribution functions, however, this method demands high computing power and does not give an analytical solution [4]. For this reason, nucleon structure still needs to be probed experimentally. Generalized Parton Distributions (GPDs), which give access to the 3-dimensional nucleon structure in longitudinal momentum and impact parameter space, can be measured in Deeply Virtual Compton Scattering (DVCS) and Hard Exclusive Meson Production (HEMP). The 3-dimensional structure in momentum space is described by the Transverse Momentum Dependent Parton Distribution Functions (TMD-PDFs) and is studied through DIS and SIDIS processes [5].

The main focus of this thesis is a study of 2016 SIDIS data collected by the COMPASS experiment on unpolarized proton target. In particular, in chapter 4, we will analyze the hadron production in terms of its angular distribution modulations – azimuthal asymmetries. The previous analysis accounted only for 11% of the available statistics from both years 2016 and 2017 when COMPASS was operating with the unpolarized target [6]. A full analysis of the year 2016 provides a bigger data sample enabling us to reduce statistical error from the earlier results. The data from 2017 cannot be analyzed at this time since the essential corrections require Monte Carlo (MC) samples that have not yet been produced. In chapter 3, one of the aspects of the process of generating MC – beam file extraction – is described. Besides that we give a brief review of the theoretical background of the TMD-PDFs in chapter 1, and an overview of the COMPASS experiment apparatus in chapter 2.

1. Introduction to the theory of parton distribution functions

1.1 Deep inelastic scattering

Lepton-proton scattering is a tool for nucleon structure research. Specifically, Deep Inelastic Scattering (DIS) off nucleon N can be described with the following expression:

$$l(k) + N(P) \to l'(k') + X(P_X), \tag{1.1}$$

in which X represents the undetected hadronic part of the final state and l and l' denote initial and final leptons with their 4-momenta in affiliated parentheses. The following set of kinematic variables is usually defined to describe DIS:

1. virtual photon 4-momentum q

$$q \equiv k - k' \tag{1.2}$$

2. virtuality Q

$$Q^2 \equiv -q^2 \tag{1.3}$$

3. Bjorken scaling variable x

$$x \equiv \frac{Q^2}{2P \cdot q} \tag{1.4}$$

4. Inelasticity y

$$y \equiv \frac{q \cdot P}{k \cdot P} \tag{1.5}$$

5. Invariant mass of the hadronic final state W

$$W^2 \equiv (q + P)^2 \tag{1.6}$$

Although these quantities are independent of the reference system and thus are relativistic invariants, only two of them are independent of each other [7]. For DIS process, the energy transferred via virtual photon needs to be high enough to allow probing the single constituents of the nucleon, while the time scale of the hard interaction needs to be small enough for partons to be considered free from the binding forces. We can describe these conditions in terms of kinematic variables and nucleon mass M by the Bjorken limit [7]:

$$\begin{gathered} Q^2 \gg M^2 \\ P \cdot q \gg M^2 \ . \end{gathered} \tag{1.7}$$

1.2 Semi-inclusive deep inelastic scattering

Semi-Inclusive Deep Inelastic Scattering (SIDIS) can be described with the following expression:

$$l(k) + N(P) \to l'(k') + h(P_h) + X(P_X) \ . \tag{1.8}$$

The only difference between DIS (eq. 1.1) and SIDIS is the detection of at least one final state hadron h with 4-momentum P_h in SIDIS process. Diagram of SIDIS is shown in figure 1.1.

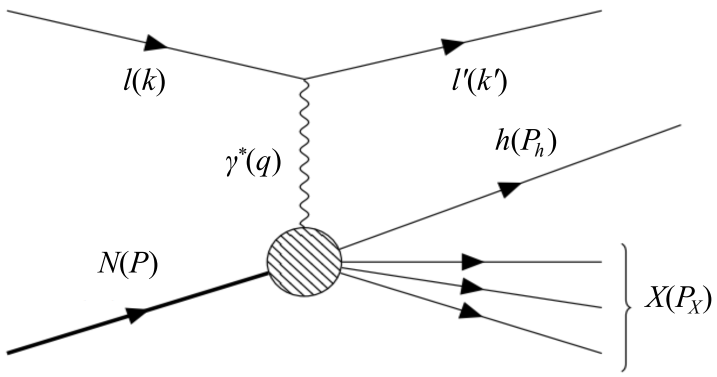

Figure 1.1: Schematic diagram of the SIDIS process in one photon approximation [8]

To describe SIDIS we introduce the Gamma Nucleon System (GNS) – a virtual photon – nucleon center-of-mass reference frame with the z direction aligned with the momentum of the virtual photon and the xz plane chosen to correspond to the lepton scattering plane. Positive x axis direction is chosen according to the scattered muon direction and the y axis is defined to complete the orthogonal right-handed system. The definition of the GNS and variables dependent on it such as transverse momentum of the hadron $\boldsymbol{P_T}$ and azimuthal angle of hadron transverse momentum (ϕ_h) are illustrated in figure 1.2.

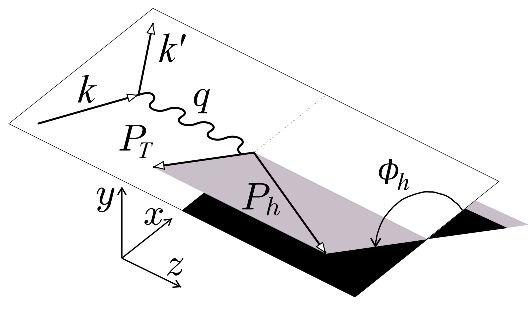

Figure 1.2: Definition of the GNS, schematic view of the SIDIS process

Transverse momentum of the hadron with respect to the virtual photon can be obtained using hadron momentum and virtual photon momentum defined in section 1.1 [7]:

$$\boldsymbol{P}_T \equiv \boldsymbol{P}_h - \frac{(\boldsymbol{P_h} \cdot \boldsymbol{q})\boldsymbol{q}}{|\boldsymbol{q}^2|} \ . \tag{1.9}$$

To fully describe the SIDIS process, another variable z expressing relative energy of the final state hadron is defined by the following expression:

$$z \equiv \frac{P \cdot P_h}{P \cdot q} \ . \tag{1.10}$$

1.2.1 SIDIS cross-section and azimuthal asymmetries

The polarized SIDIS cross-section in the one-photon-exchange approximation can be found in [9]. When the target nucleon is not polarized, the cross-section has no contribution from spin-dependent terms and simplifies to [10, 11]:

$$\begin{aligned}\frac{\mathrm{d}^5\sigma}{\mathrm{d}x\mathrm{d}y\mathrm{d}z\mathrm{d}\phi_h\mathrm{d}\boldsymbol{P_T^2}} =& \frac{2\pi\alpha^2}{xyQ^2}\frac{y^2}{2(1-\varepsilon)}(1+\frac{\gamma^2}{2x})\Big[F_{UU,T} + \varepsilon F_{UU,L} + \\ \sqrt{2\varepsilon(1+\varepsilon)}F_{UU}^{\cos\phi_h}\cos\phi_h &+ \varepsilon F_{UU}^{\cos 2\phi_h}\cos 2\phi_h + \lambda\sqrt{2\varepsilon(1+\varepsilon)}F_{LU}^{\sin\phi_h}\sin\phi_h\Big],\end{aligned} \tag{1.11}$$

in which ε is defined as:

$$\varepsilon = \frac{1-y-\frac{1}{4}\gamma^2y^2}{1-y+\frac{1}{2}y^2+\frac{1}{4}\gamma^2y^2} \ . \tag{1.12}$$

In equation 1.11 λ denotes longitudinal polarization of the incoming lepton and γ is defined using nucleon mass M as:

$$\gamma = \frac{2Mx}{Q} \ , \tag{1.13}$$

$F_{UU,T}$, $F_{UU,L}$, $F_{UU}^{\cos\phi_h}$, $F_{LU}^{\sin\phi_h}$ and $F_{UU}^{\cos 2\phi_h}$ are quark flavor, type of hadron, x, z, Q^2 and $\boldsymbol{P_T^2}$ dependent structure functions for specific modulation $f(\phi_h)$ in the superscript. Letters in the subscript denote polarization of the lepton beam (first letter), target (second letter), and photon (optional third letter).

Up to twist 4[1], we can neglect the contribution of $F_{UU,L}$ and define azimuthal asymmetries, while denoting $F_{UU,T} + \varepsilon F_{UU,L} \approx F_{UU,T} \equiv F_{UU}$:

$$A_{UU}^{\cos\phi_h} \equiv \frac{F_{UU}^{\cos\phi_h}}{F_{UU}} \quad , \quad A_{UU}^{\cos 2\phi_h} \equiv \frac{F_{UU}^{\cos 2\phi_h}}{F_{UU}} \quad , \quad A_{LU}^{\sin\phi_h} \equiv \frac{F_{LU}^{\sin\phi_h}}{F_{UU}}, \tag{1.14}$$

or more generally:

$$A_{XY}^{f(\phi_h)} \equiv \frac{F_{XY}^{f(\phi_h)}}{F_{UU}}, \tag{1.15}$$

the cross-section in equation 1.11 can be rewritten as [11, 13]:

$$\frac{\mathrm{d}^5\sigma}{\mathrm{d}x\mathrm{d}y\mathrm{d}z\mathrm{d}\phi_h\mathrm{d}\boldsymbol{P_T^2}} \propto (1+\varepsilon_1 A_{UU}^{\cos\phi_h}\cos\phi_h + \varepsilon_2 A_{UU}^{\cos 2\phi_h}\cos 2\phi_h + \lambda\varepsilon_3 A_{LU}^{\sin\phi_h}\sin\phi_h), \tag{1.16}$$

where $\varepsilon_i, \quad i \in \{1,2,3\}$ represent following expressions:

$$\varepsilon_1 = \frac{2(2-y)\sqrt{1-y}}{1+(1-y)^2}, \qquad \varepsilon_2 = \frac{2(1-y)}{1+(1-y)^2}, \qquad \varepsilon_3 = \frac{2y(\sqrt{(1-y)})}{1+(1-y)^2}. \tag{1.17}$$

[1] Twist is a number related to mass dimension and spin, which determines the $\frac{1}{Q}$ scale order at which TMD-PDFs appear in the factorization [12]

1.2.2 Transverse Momentum Dependent PDFs and Fragmentation Functions

When the scattering approaches the *Bjorken limit* (idealized case when $Q^2 \to \infty$ and $P \cdot q \to \infty$, but $x = \frac{Q^2}{2P \cdot q}$ is finite [7, 14]) the structure functions can be described at tree level (not including loops) in terms of convolutions $\mathscr{C}$ of Transverse Momentum Dependent Parton Distribution Functions (TMD-PDFs) denoted as $f^q(x, \boldsymbol{k_T}, Q^2)$ and Transverse Momentum Dependent Fragmentation Functions (TMD-FFs) denoted as $D^{q \to h}(z, \boldsymbol{P}_\perp, Q^2)$ [15]:

$$\begin{aligned} \mathscr{C}[\omega f D] =& x \sum_q e_q^2 \int \mathrm{d}^2\boldsymbol{k_T} \mathrm{d}^2\boldsymbol{p}_\perp \\ & \delta^{(2)}(z\boldsymbol{k_T} + \boldsymbol{P}_\perp - \boldsymbol{P_T}) w(\boldsymbol{k_T}, \boldsymbol{P}_\perp) f^q(x, \boldsymbol{k_T}, Q^2) D^{q \to h}(z, \boldsymbol{P}_\perp, Q^2) \ , \end{aligned} \tag{1.18}$$

where $w(\boldsymbol{k_T}, \boldsymbol{P}_\perp)$ is a weight, $\boldsymbol{k_T}$ denotes the transverse momentum of a struck quark inside the unpolarized nucleon, $\boldsymbol{P}_\perp$ is a transverse momentum acquired by the fragmenting parton during the hadronization and q runs over quark flavours. The complete description of the nucleon at leading twist requires eight TMD-PDFs and eight TMD-FFs. However, for unpolarized nucleon these numbers are reduced to 2: TMD-PDFs unpolarized f_1 and *Boer-Mulders* function $h_1^\perp$ together with TMD-FFs unpolarized D_1 and *Collins* function $H_1^\perp$. Using these functions we can express non-trivial unpolarized SIDIS structure functions at leading twist as follows [9]:

$$\begin{aligned} F_{UU,T} &\approx \mathscr{C}[f_1 D_1] \ , \\ F_{UU}^{\cos 2\phi_h} &\approx \mathscr{C}\left[\frac{2(\hat{\boldsymbol{h}} \cdot \boldsymbol{k_T})(\hat{\boldsymbol{h}} \cdot \boldsymbol{P}_\perp) - (\boldsymbol{k_T} \cdot \boldsymbol{P}_\perp)}{zMM_h} h_1^\perp H_1^\perp\right] \ , \end{aligned} \tag{1.19}$$

where M_h is hadron mass and $\hat{\boldsymbol{h}} \equiv \frac{\boldsymbol{P_T}}{|\boldsymbol{P_T}|}$. $F_{LU}^{\sin\phi_h}$ and $F_{UU}^{\cos\phi_h}$ have its first non trivial contribution at twist 3. If the quark-gluon-quark twist 3 TMD-FFs are neglected (also called Wandzura-Wilczek-type approximation [15]) and assuming the factorization from equation 1.18 holds also at twist 3, $F_{UU}^{\cos\phi_h}$ can be expressed in terms of D_1, f_1, $H_1^\perp$ and $h_1^\perp$ according to [9] as:

$$F_{UU}^{\cos\phi_h} \approx \frac{2M}{Q} \mathscr{C}\left[-\frac{(\hat{\boldsymbol{h}} \cdot \boldsymbol{k_T})}{M} f_1 D_1 + \frac{\boldsymbol{k_T^2}(\hat{\boldsymbol{h}} \cdot \boldsymbol{P}_\perp)}{z^2 M^2 M_h} h_1^\perp H_1^\perp + \ldots\right] \ . \tag{1.20}$$

The twist 3 approximation of $F_{UU}^{\cos\phi_h}$ can be also rewritten as a sum of two terms:

$$F_{UU}^{\cos\phi_h} = F_{UU}^{\cos\phi_h}\Big|_{\mathrm{Cahn}} + F_{UU}^{\cos\phi_h}\Big|_{\mathrm{BM}} \ , \tag{1.21}$$

which can be expressed in terms of convolutions 1.18 as:

$$\begin{aligned} F_{UU}^{\cos\phi_h}\Big|_{\mathrm{Cahn}} &= -\frac{2M}{Q} \mathscr{C}\left[\frac{(\hat{\boldsymbol{h}} \cdot \boldsymbol{k_T})}{M} f_1 D_1\right] \\ F_{UU}^{\cos\phi_h}\Big|_{\mathrm{BM}} &= \frac{2M}{Q} \mathscr{C}\left[\frac{\boldsymbol{k_T^2}(\hat{\boldsymbol{h}} \cdot \boldsymbol{P}_\perp)}{z^2 M^2 M_h} h_1^\perp H_1^\perp\right] \end{aligned} \tag{1.22}$$

First of the terms ($F_{UU}^{\cos\phi_h}\big|_{\mathrm{Cahn}}$) proportional to the convolution of the unpolarized TMDs f_1 and D_1 is associated with the *Cahn effect*. R.N. Cahn discovered that the probability of given interaction between parton and lepton is dependent on the relative orientation of the parton and leptonic scattering planes (non-coplanarity of the planes has its origin in the struck quark intrinsic momentum $\boldsymbol{k_T}$) and derived the result of this effect – a negative $\cos\phi_h$ modulation for the hadron after fragmentation [16]. The second term $F_{UU}^{\cos\phi_h}\big|_{\mathrm{BM}}$ is proportional to the convolution of *Boer-Mulders* function $h_1^\perp$ and *Collins* function $H_1^\perp$. For the reason of the $F_{UU}^{\cos\phi_h}\big|_{\mathrm{BM}}$ being suppressed by a factor $\left(\frac{\boldsymbol{k_T}}{M}\right)^2$, the *Cahn effect* is expected to dominate [10, 11].

1.2.3 TMDs in Gaussian Ansatz

Assuming we can factorize TMD-PDFs (TMD-FFs), into an x-dependent (z-dependent) collinear part and $\boldsymbol{k_T}$-dependent ($\boldsymbol{P}_\perp$-dependent) part, the convolution 1.18 can have an analytical solution. In particular, a convinient choice is the Gaussian Ansatz [17]:

$$\begin{aligned} f(x, \boldsymbol{k_T}, Q^2) &= f(x, Q^2)\frac{\exp(\frac{-\boldsymbol{k_T^2}}{\langle \boldsymbol{k_T^2}\rangle})}{\pi\langle \boldsymbol{k_T^2}\rangle} \ , \\ D(z, \boldsymbol{P}_\perp, Q^2) &= D(z, Q^2)\frac{\exp(\frac{-\boldsymbol{P}_\perp^2}{\langle \boldsymbol{P}_\perp^2\rangle})}{\pi\langle \boldsymbol{P}_\perp^2\rangle} \ , \end{aligned} \tag{1.23}$$

where $\langle \boldsymbol{k_T^2}\rangle$ and $\langle \boldsymbol{P}_\perp^2\rangle$ are mean values of $\boldsymbol{k_T^2}$ and $\boldsymbol{P_\perp^2}$ respectively. In equation 1.23, quark flavor dependence was neglected for brevity. The Gaussian Ansatz provides independent access from the structure function F_{UU} to the mean value of the intrinsic transverse momentum $\langle \boldsymbol{k_T^2}\rangle$ as well as from the $F_{UU}^{\cos 2\phi_h}$ to the Boer-Mulders function $h_1^\perp$. Full calculations can be found in [11].

2. The COMPASS spectrometer

COmmon Muon Proton Apparatus for Structure and Spectroscopy (COMPASS) is a high-energy physics experiment at the M2 beamline of the Super Proton Synchrotron (SPS) at CERN[1] designed to study nucleon spin structure and hadron spectroscopy. Results are obtained through recording and analyzing the scattering of muon and hadron beams off fixed targets.

The basic layout of the 60 m long experimental hall with COMPASS two-stage spectrometer is shown in figure 2.1. The scheme shows the 2004 muon beam setup. In the meantime, ECAL1 was added in front of HCAL1 and several tracking detectors were replaced, but the overall picture has not changed. Specifically for the 2016–2017 runs, ECAL0 calorimeter and a recoil proton detector CAMERA were built. More artistic view of the detector 2016–2017 setup is in figure 2.2. In the following sections, we will describe the whole COMPASS setup with an emphasis on the setup for the 2016 μ beam, since the data from this year have been analyzed in chapter 4.

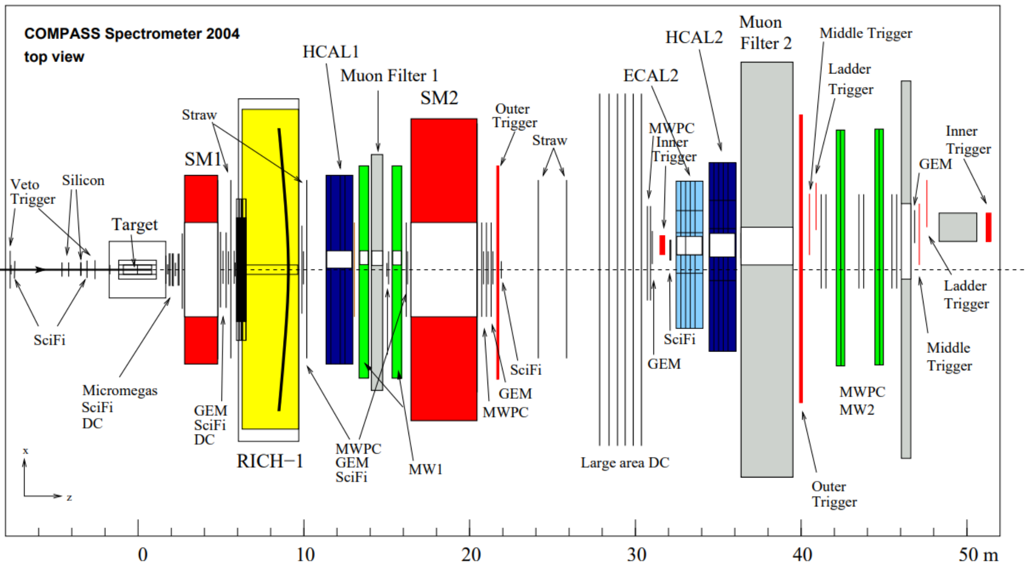

Figure 2.1: Top view of the 2004 layout of the COMPASS spectrometer [18]

[1]European Organization for Nuclear Research (from the French 'Conseil Européen pour la Recherche Nucléaire') (CERN)

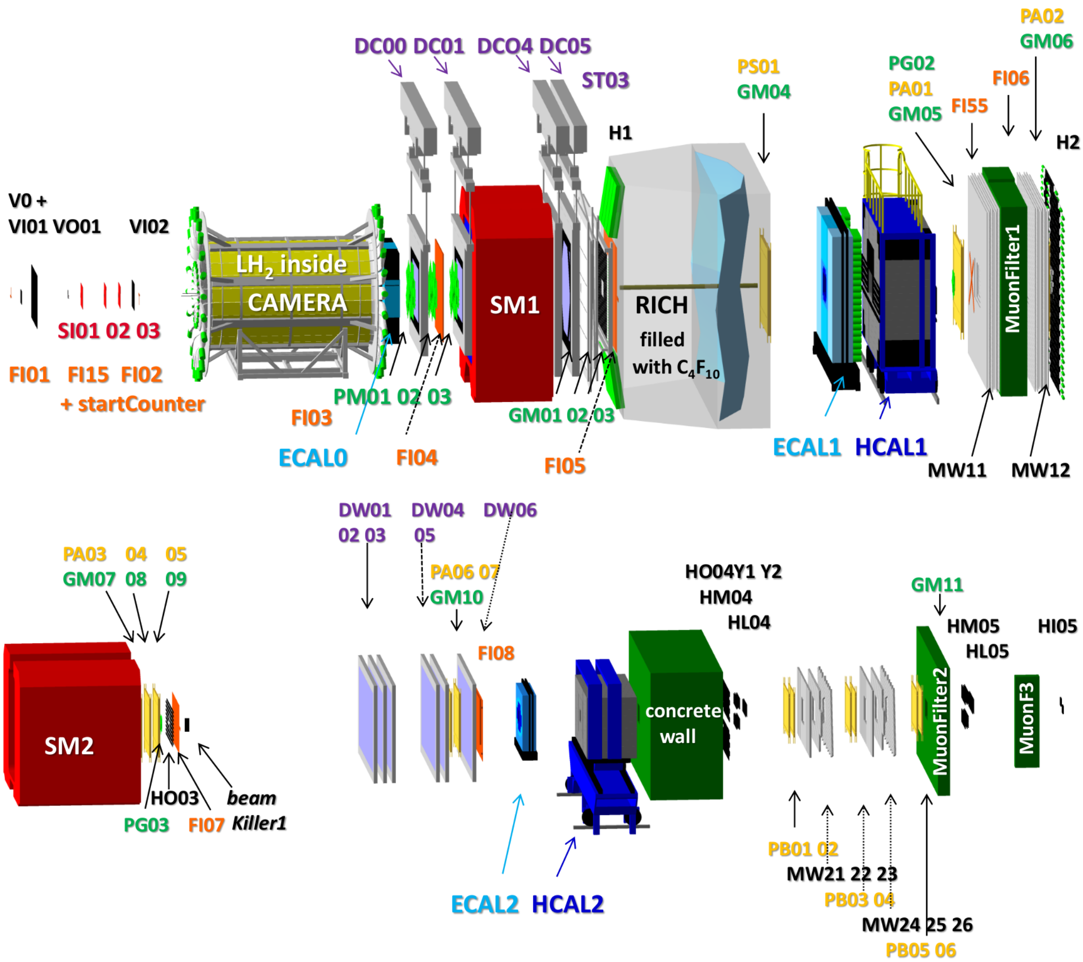

Figure 2.2: Artistic view of the complete 2016–2017 COMPASS detector setup, source: COMPASS collaboration

The laboratory reference frame of the COMPASS experiment is defined with its origin as a set point on the spectrometer axis in the target region. Positions in this thesis are given in the reference frame with X, Y, and Z coordinates, which can be identified with the x and z axes in the figure 2.1 while Y axis aims towards the reader.

2.1 Beam and the beam momentum station

The approximately 1 km long M2 beamline provides a beam of muons or hadrons to the COMPASS target. First, a proton beam is slowly extracted from the SPS. The extraction of protons from SPS is not a continuous process. There is a time window in which COMPASS receives constant beam intensity from SPS – the *spill*. Super cycles are time-periodic intervals of acceleration and proton extraction in SPS. The length of the super cycle is usually 30–45 s depending on the occupancy of the SPS and it may contain one or two spills of about 5 s. An example of proton intensity profile in the super cycle as provided by the CERN Control Center (CCC) is shown in figure 2.3.

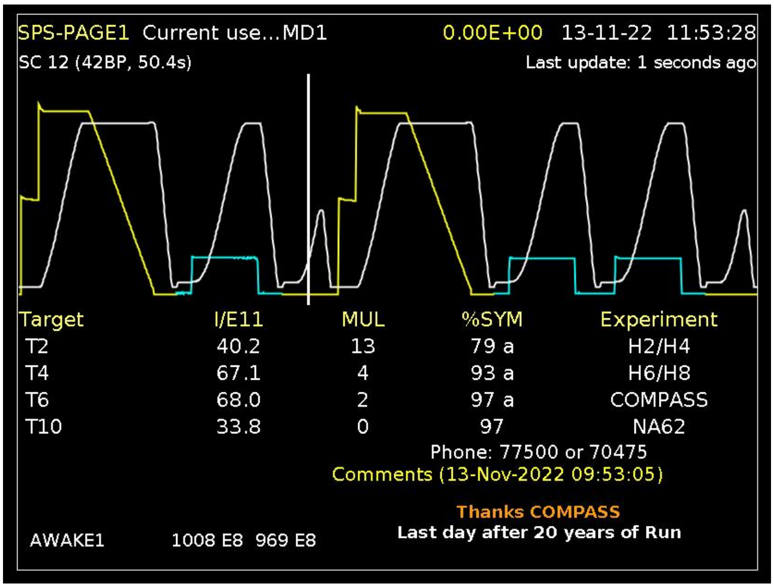

Figure 2.3: SPS proton beam intensity (yellow curve) in 50.4 s long super cycle with two spills as provided by the SPS control centre at the end of data taking of experiment COMPASS. During the spill, the beam intensity in SPS is linearly decreasing, source: COMPASS collaboration

The whole process of producing and transferring μ beam to the COMPASS target is depicted in figure 2.4. Beam muons (or pions) are produced with a process, in which a proton beam from SPS hits the beryllium target (T6) while creating a secondary hadron beam with the collision. The momentum and charge of the secondary products are chosen by an array of quadrupoles and dipoles, which are in the case of a pion beam also used to filter out muons, which are produced mainly in the decay of secondary hadrons thus with lower momentum than pions. On the contrary, in the case of the muon beam, the hadron component is removed from the beam by a series of absorbers. Due to the nature of the decay process, the muon beam is polarized. After this process, the beam reaches a series of detectors and magnets called the Beam Momentum Station (BMS), which is still located downstream of the target, outside the experimental hall. To reach the experimental hall, the beam is bent horizontally by the three dipole magnets (B6). Six scintillator-based detectors (BM01–06) with spatial resolution $\sigma_s = 0.12$–2.5 mm and time resolution $\sigma_t = 0.3$–0.5 ns positioned around B6 provide a measurement of the momentum of each passing muon [18].

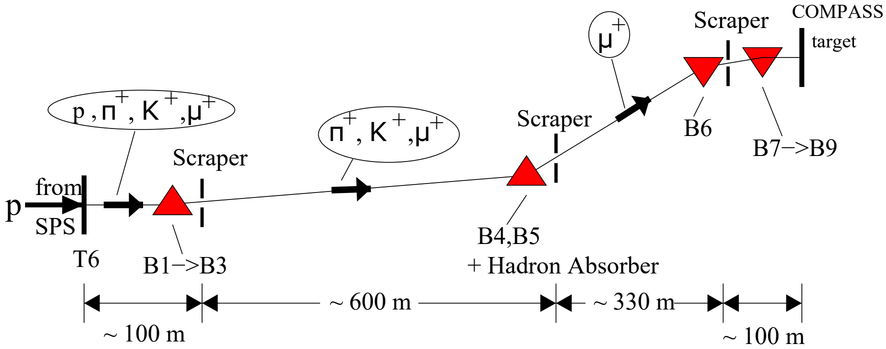

Figure 2.4: Schematic view of the M2 beam line and μ beam production [19]

2.1.1 Beam parameters

To maximize the statistical significance of nucleon structure studies, an energy[2] of 160 GeV was chosen as a compromise between a high flux and a high polarization. Longitudinal polarization of the SPS beam is $\lambda = 0.8$ for μ^- and $\lambda = -0.8$ for μ^+ [20]. The beam is focused on the target with a variance of its Gaussian core at the target $\sigma = 7$ mm, has a momentum spread of $\frac{\sigma_p}{p} = 0.05$ and divergence 1 mrad (measurements from 2004 [21]). The typical momentum distribution and horizontal profile at the target are shown in figure 2.5.

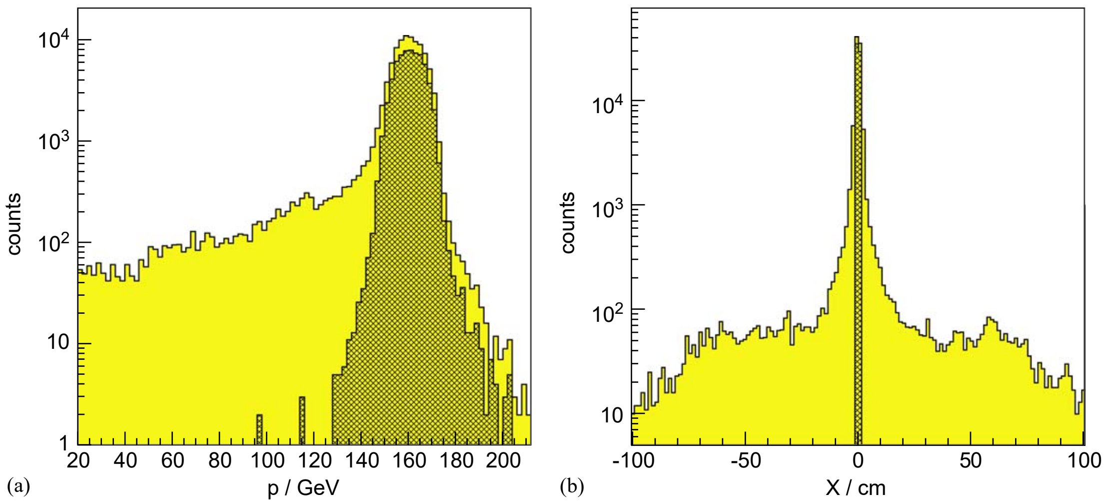

Figure 2.5: Distribution of (left) beam momentum and (right) horizontal profile at the target position, grey part corresponds to the *true beam* and the yellow part to the *beam halo*[21]

In the figure 2.5, Gaussian core called *true beam* and the non-Gaussian tail, called *near halo* are clearly visible. Generally, the *near halo* has about 30% of the whole beam intensity. Lower energy muons at larger distances from the beam make up so-called *outer halo*.

2.2 Target region

To probe nucleon structure, the COMPASS experiment has been using various types of targets including polarized solid targets, heavy nuclear targets, and liquid hydrogen targets. In 2016 – the year of origin of the data analyzed in chapter 4 of this thesis, an unpolarized liquid hydrogen target was used. A schematic view of the target cell is in figure 2.6

[2]In the whole thesis, natural units are used ($c = 1$ and $\hbar = 1$)

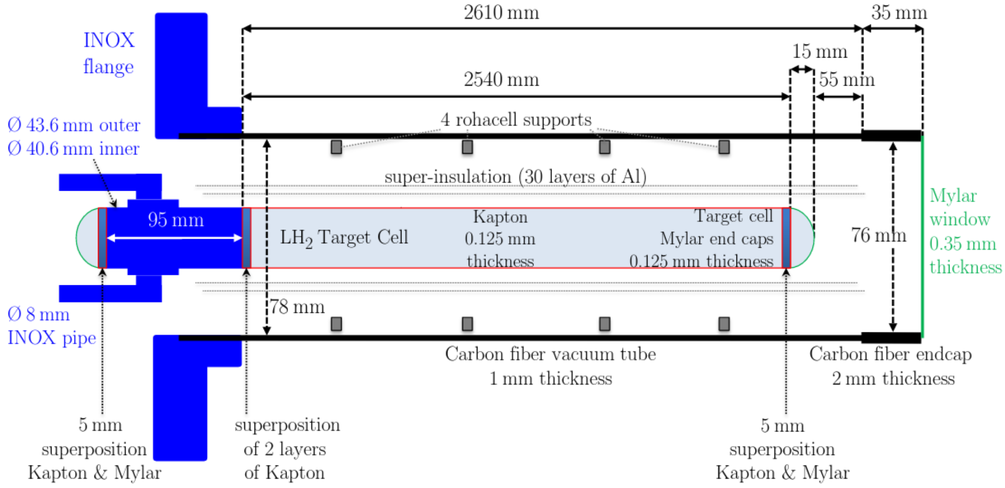

Figure 2.6: A schematic side view of the target cell [22]

The target region also comprises the detectors surrounding the target. Recoil Proton Detector (RPD) is a time-of-flight detector, which determines the exclusivity of processes under investigation by measuring the recoil of the protons in the target. Three silicon stations and Scintillating Fibre (SciFi) counters were installed upstream of the target to determine the trajectory of the incoming beam particle with the resolutions $\sigma_s \approx 10$ µm, $\sigma_t = 2.5$ ns and $\sigma_s = 130$ µm, $\sigma_t = 0.4$ ns, respectively. Another SciFi station is downstream of the target in the RPD CAMERA.

2.3 Large and small area spectrometer

Detectors located downstream of the target region comprise a series of electromagnetic and hadronic calorimeters, tracking detectors, and particle identification detectors, that are either components of Large Angle Spectrometer (LAS) or Small Angle Spectrometer (SAS). LAS surrounds dipole Spectrometer Magnet (SM) 1 and is designed to have ±180 mrad acceptance [23] (in this context acceptance is defined as the maximum angle between prolonged beam track and reconstructable track). SAS corresponds to detectors located downstream of the dipole magnet SM2 and detects particles scattered at small polar angles.

2.3.1 Tracking detectors

Different tracking techniques are employed in regions at different distances from the beam axis, in order to match the requirements concerning rate capability, space and time resolution as well as the size of the surface to be instrumented. The tracking detectors measure at least one of X, Y, U, V coordinates. SciFis and microstrip detectors are considered as so-called Very Small Area Trackers (VSAT) which are characterized by small size and excellent space (σ_s = 130–210 µm for SciFis, σ_s = 10 µm for microstrips) or time resolution (σ_t = 0.4 ns). For distances from the beam larger than 2.5 cm we require high spatial resolution and minimum material budget, which is provided by Small Area Trackers (SAT) such as 3 Micromesh Gaseous Structures (Micromegas) ($\sigma_s = 90$ µm, $\sigma_t = 9$ ns) and 11 Gas Electron Multipliers (GEMs) ($\sigma_s = 70$ µm, $\sigma_t = 12$ ns). Lastly, Large Area Trackers (LAT) provide good spatial resolution and cover the large areas defined by the experimental setup acceptance. In this group of detectors belongs Drift Chambers (DCs) ($\sigma_s = 190$ µm), that surround SM1. At the very end of the setup, Multi-Wire Proportional Chambers (MWPCs) ($\sigma_s = 1.6$ mm) track particles scattered at small angles [18].

2.3.2 Particle identification

Particle identification allows us to distinguish between different types of particles that are produced in the desired observed process. Various techniques, which were implemented in COMPASS spectrometer to identify scattered particles are described in the following subsections.

RICH

As a particle identification detector, COMPASS uses a Ring Imaging CHerenkov (RICH) located downstream SM1 dipole magnet. Charged hadrons with momenta from a few GeVs to 43 GeV can be recognized by measuring the emission angle of Cherenkov radiation. Single photon resolution of COMPASS RICH is $\sigma_{\mathrm{ph}} = 1.2$ mrad and ring resolution $\sigma_{\mathrm{r}} = 0.55$ mrad. The principle of the RICH detector is shown in figure 2.7 [18].

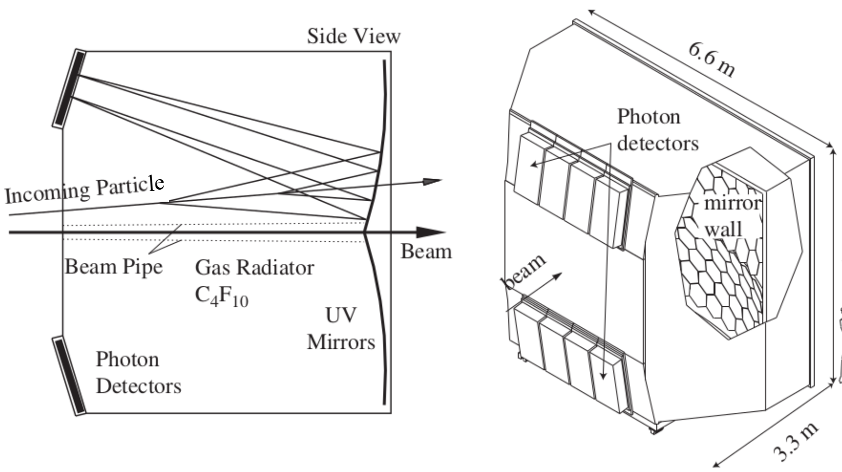

Figure 2.7: Principle and artistic view of RICH detector used in COMPASS setup [18]

Scattered muon identification

The SIDIS process cannot be analyzed without measuring the scattered muon momentum and correctly identifying the scattered muon in the first place. To identify scattered muons, two Muon Filter (MF) stations with absorbers thick enough to stop incoming hadrons are implemented at the very ends of LAS and

SAS together with the Muon Wall (MW), which consists of trackers with moderate space resolution situated downstream the MFs. Particles with trajectory reconstructed through the MF are identified as muons.

Calorimeters

The COMPASS setup includes both types of calorimeters: Hadronic CALorimeter (HCAL) and Electromagnetic CALorimeter (ECAL). Two hadron calorimeters implemented in the spectrometer are sampling calorimeters using stacks of iron and scintillator plates and their purpose in the setup is to measure the energy of hadrons produced in the target and provide an unbiased trigger used to measure the efficiency of the physics triggers. ECALs 0, 1, 2 are homogeneous or sampling calorimeters. The ECALs are used to measure photons from DVCS and π^0 decays.

2.4 Trigger system

The trigger system is a tool to determine whether the readout electronics should record an event. COMPASS uses signals from calorimeters and scintillating hodoscopes with horizontal and vertical strips as triggers for physical processes. Target-pointing triggers (Middle Trigger (MT), Outer Trigger (OT) and Large Angle Spectrometer Trigger (LAST)) as well as energy-loss triggers (Ladder Trigger (LT)), use a coincidence of signals from two hodoscopes, which are positioned to distinguish scattered muon that interacted with the target. A muon track that has not interacted will fail the coincidence. Target-pointing triggers are unable to determine good event candidates at small vertical scattered muon angles and in these cases, energy-loss triggers are used.

Inner and outer veto system, consisting of scintillating hodoscopes positioned in the target region, is used to prevent acquisition of events containing near and far halo tracks, which would otherwise fire the physics triggers.

Specifically to trigger SIDIS events, one of the following triggers: LT, MT, OT, or LAST, needs to be fired. This selection determines the trigger mask cut, which is made later, in the data analysis.

For other purposes COMPASS uses two random triggers. *TRand* is triggering on decays of radioactive source. This so-called true random trigger is used to measure the beam flux (and the luminosity of the experiment), to study detector properties, or to extract a representative sample of beam tracks for a beam file. A *NRand* is a random trigger based on a pseudo-random number generator used for setting up the spectrometer and Data Acquisition System (DAQ) tests, where a higher trigger rate is necessary [21].

2.5 Data acquisition

DAQ takes care of data reading, taking, and storing. If at least one of the triggers is fired, detector readout electronics send the data through concentrator modules to the DAQ computers. Optical links are used for the transfer and the CERN developed *S-Link* standard is followed throughout the whole process [24]. The event building used to be done by distributing data between online computers connected through an Ethernet Gigabit network. Since 2013–2014 COMPASS uses Field Programmable Gate Arrays (FPGAs) technology to be able to encode the event-building algorithm in the hardware, which has been found a faster and more reliable in comparison to the previous one [25]. After this procedure, the so-called *raw* data are transferred to CERN's central data recording system - CERN Advanced STORage manage (CASTOR).

Data taking is split into periods. Periods consist of runs that are composed of a series of spills. Conventionally the complete run consists of 200 spills, but the data-taking can be interrupted earlier by the shift crew in case of beam loss, detector problems, etc. in order to have the largest amount of useful data of the best quality possible. To monitor detector activity Detector Control System (DCS) and COMPASS Object-Oriented OnLine (COOOL) software tools are used.

2.6 Event reconstruction

The raw data are reconstructed offline using an object-oriented package called COMPASS Reconstruction and AnaLysis (CORAL), which is performing fits through the measured hits in detectors with a result in the form of a reconstructed track and reconstructed vertices – points of interaction. CORAL also identifies primary vertices (defined as vertices with an incoming muon track). Essential information for the reconstruction includes detector positions, calibration, efficiencies, and material maps.

The first rough estimation of a detector position is done physically in the experimental hall by optical measurements. In order to fully profit from the detector spatial resolution, CORAL needs the detector positions measured more precisely than the physical optical measurement is able to provide. To improve the rough first estimation, the so-called *alignment* procedure is used. In the process of *alignment* detector planes are digitally moved over small distances in such a way, that minimizes the global χ^2 of the tracks. Special data taken in special conditions called *alignment runs* are used for the *alignment*. Before the digital changes in detector positions are implemented, the effect on the reconstruction of the real data needs to be checked.

Reconstructed data are stored in mini Data Summary Trees (mDSTs) and are analyzed using the already mentioned ROOT-based framework – PHysics Analysis Software Tools (PHAST).

2.7 Process of generation of Monte Carlo simulation

A Monte Carlo (MC) simulation is generated for each data-taking period and beam charge setting. The whole process consists of extracting beam file[3], trigger efficiencies and detector positions for the given period and beam charge, then generating hard scattering events and the last step is to propagate the products

[3]Beam file provides a sample of beam tracks reconstructed from the real data. These tracks with their parameters describe incoming beam particle properties such as momentum at the vertex, which are essential inputs for the MC generator.

of the generated event through the spectrometer. Generated MC data are then reconstructed with CORAL in the same manner as the real data and both generated and reconstructed MC samples are later used for acceptance correction or background evaluation.

In COMPASS experiment various event generators are used to produce simulations of various processes including *LEPTO* for DIS (SIDIS) and *HEPGEN* for exclusive processes, for example the deep virtual vector meson production, which constitutes a background for SIDIS [26, 27]. Other generators *DJANGOH* and *SOPHIA*, which are also accounting for electroweak radiative effects in DIS, are being tested.

The event-generating process is followed by a simulation of the passage of particles through the spectrometer, which is provided by *TGeant* software package based on *Geant4*. As an input *TGeant* requires detector positions and trigger efficiencies. The output of *TGeant* are, besides the generated MC data, also material maps mentioned earlier while describing event reconstruction in section 2.6 [28].

3. Beam file production

As was stated in the section 2.7, the production of MC samples is an important task, which is essential for various corrections made on the real data. 2022 and 2017 MC samples have not been generated yet. In the next sections, we will prepare for extracting the 2017 and 2022 muon beam files through an investigation of the process of beam file production.

3.1 Introduction to the beam file production

The beam file is used as an input to the Monte Carlo event generator. The complete process of generating MC simulations was described in section 2.7 of this thesis. The COMPASS beam file specifically contains a sample of incoming beam tracks, one per line, each of them described by:

1. 1 integer for beam type
2. 2 double types for X and Y position in mm
3. 2 double types for slope $\frac{\mathrm{d}X}{\mathrm{d}Z}$,$\frac{\mathrm{d}Y}{\mathrm{d}Z}$ in mrad
4. 1 double type for momentum in GeV.

Positions, slopes and momentum values written in the beam file are extrapolated to $Z = 0$ cm without the use of the material maps. Due to the file size and type requirements of TGeant in the process of the beam file production, the file contains are rewritten from ASCII format to 4-bit binary. To meet the file size requirements only 10 million randomly selected beam tracks from the corresponding period are considered in the beam file production. Due to changing beam parameters, it is necessary to extract 2 beam files for each period, each one representing a different muon charge as the MC samples are generated for μ^+ and μ^- beam separately.

3.2 Selection of beam tracks for the beamfile

For beam file extraction, only events selected by a true random trigger are accounted. In the so-called trigger cut, we also exclude events with VETO trigger fired, because VETO signal is applied to physics triggers, but not to the true random trigger (see section 2.4).

Next, we select events that occurred only in the correct spill time window. Stable beam intensity is important for data analysis thus we only account for the flat top in the beam intensity within an SPS super-cycle called spill window. If the beam is stable, then the spill window is estimated from a two-dimensional histogram of the time dependency of the beam profile. In 2016 and 2017, the beam intensity largely varied, so the flat tops were determined by the COMPASS Mainz group for every spill and saved in so-called flux files. Figure 3.1 shows stable time dependencies of beam profiles from the 2022 week 3 data sample. The spill window range was estimated as interval (1.2 s, 5.4 s).

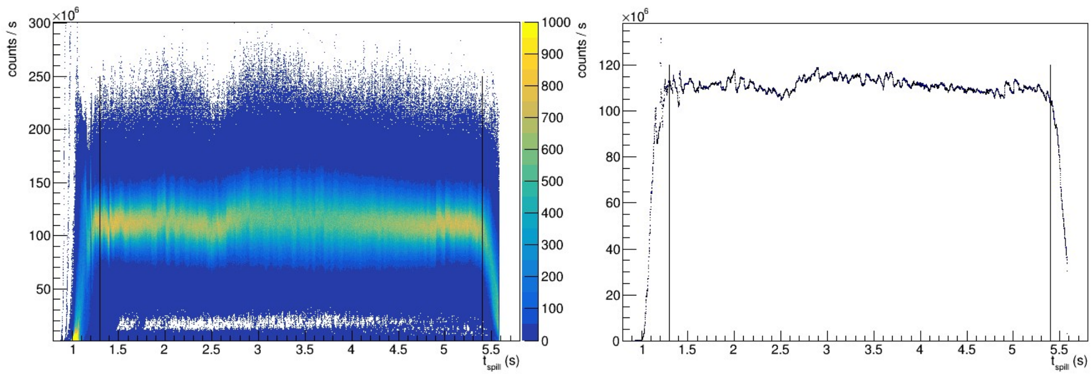

Figure 3.1: (left) 2D plot of beam intensity time dependence (color scale denotes the number of spills with given intensity at given time) and (right) average intensity as a function of time, source: COMPASS collaboration

Following cuts are made on tracks of the event. We demand $\frac{\chi^2}{n_{\mathrm{df}}} < 10$ and track time value within 15 ns around the fired trigger considering an error interval of 3σ. Then we define six beam types to be able to distinguish from *beam core* and *halo* (denoting Z_{first} and Z_{last} the positions of the first and the last hit detected by spectrometer):

Type 1: (*true beam*) $Z_{\mathrm{first}} < 0$ cm , momentum > 0 GeV

Type 2: (*near halo*) $Z_{\mathrm{last}} > 1800$ cm, $Z_{\mathrm{first}} > 0$ cm, momentum > 50 GeV

Type 3: (*outer halo*) $Z_{\mathrm{first}} > 0$ cm, 350 cm $< Z_{\mathrm{last}} <$ 1800 cm, 10 GeV $<$ momentum $<$ 50 GeV

Type 4: (*outer halo*) $Z_{\mathrm{first}} > 350$ cm, 1450 cm $< Z_{\mathrm{last}} <$ 1800 cm, hits in MW 1 ≥ 10

Type 5: (*outer halo*) $Z_{\mathrm{first}} > 1350$ cm, hits in MW 1 ≥ 12

Type 6: (*outer halo*) $Z_{\mathrm{first}} < 3800$ cm, $Z_{\mathrm{last}} > 3800$ cm

and filter out tracks that don't match any type of definition. Part of the spectrometer that is important in each beam type detection is shown in figure 3.2. In the next step, only the incoming muon (μ_0) track is selected in the so-called vertex cut, which rejects all the outcoming tracks from the primary vertex. Then the μ_0 tracks with no BMS info, which are automatically assigned 160 GeV momentum, are excluded. Then an additional cut on type 6 beam track is made on tracks with X at $Z = 10$ m in the range from -70 cm to 140 cm and simultaneously with $|Y| < 1$ cm at the same Z position. Next, tracks with $\frac{\mathrm{d}X}{\mathrm{d}Z} < 40$ mrad or $\frac{\mathrm{d}Y}{\mathrm{d}Z} < 40$ mrad are excluded together with tracks having higher momentum than 200 GeV. The effect of the applied cuts on data from 2017 period 7 is shown in the following tables 3.2 and 3.2 (variable N corresponds to the number of events/tracks after given cut). The distribution of the beam tracks between beam types is shown in table 3.3.

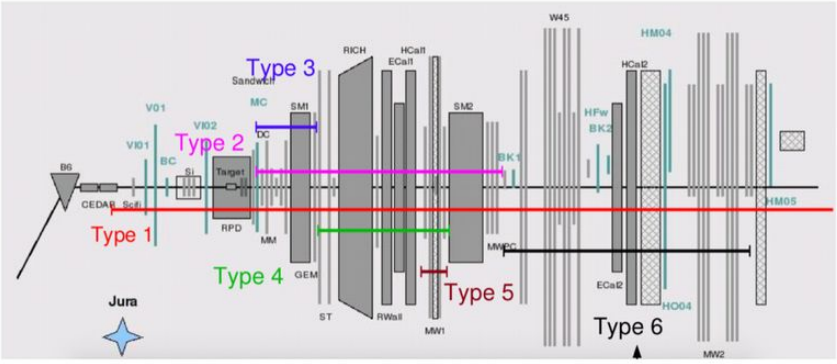

Figure 3.2: Diagram of the COMPASS spectrometer with marked parts that are important in detecting and distinguishing each beam type, source: COMPASS collaboration

Table 3.1: Effect of the applied event cuts on data from 2017 period 7 μ^+ and μ^-

	μ^+		μ^-	
event cut	percentage	N	percentage	N
All randomly selected events	1.0000	355863328	1.0000	364787072
Trigger cut	0.1117	39734660	0.1332	48583724
TiS window check	0.0754	26830564	0.0906	33051258

Table 3.2: Effect of the applied track cuts on data from 2017 period 7 μ^+ and μ^-

	μ^+		μ^-	
track cut	percentage	N	percentage	N
All tracks	1.0000	84087248	1.0000	80635024
Tracks with defined parameter	1.0000	84087248	1.0000	80635024
$\frac{\chi^2}{n_{\mathrm{df}}} < 10$	0.9919	83404112	0.9927	80043120
Trigger time window	0.7899	66422776	0.7898	63687596
6 beamtypes	0.3302	27762660	0.3434	27691468
Vertex cut	0.2425	20395160	0.2501	20170206
Tracks with BMS info	0.1363	11464599	0.1430	11530453
Additional type 6 selection	0.1363	11462792	0.1430	11528851
Slope cut	0.1363	11461379	0.1430	11527839
Momentum<200 GeV	0.1358	11415352	0.1424	11485173

Table 3.3: Distribution of the beam tracks between beam types for 2017 period 7 μ^+ and μ^- beam file (number on top of each row corresponds to the number of beam tracks, number on the bottom is a percentage)

	type 1	type 2	type 3	type 4	type 5	type 6	all beam tracks
μ^-	8854934	2570050	7214	57961	0	439	11485173
	0.77	0.2238	0.0006	0.0050	0.0000	0.0000	1.0000
μ^+	8703505	2639401	5512	68444	0	528	11415352
	0.7624	0.2312	0.0005	0.0060	0.0000	0.0000	1.0000

3.3 Vizualization of the beam profile and comparison of the beam parameters

To check whether the beam track for the beam file were chosen correctly, we need to check histograms of momenta, errors of momenta, χ^2, X, $\frac{\mathrm{d}X}{\mathrm{d}Z}$, $\frac{\mathrm{d}Y}{\mathrm{d}Z}$ and Y extrapolated to different Z reference positions (as relevant reference points were chosen $Z = 0$ cm, $Z = 1000$ cm, $Z = 3000$ cm, and $Z = 4100$ cm) for each beam type. These quantities are compared with their expected values, some of which are given in section 2.1.1. For illustration, a few of the histograms for 2017 data period 7 μ^+ and μ^- beam are shown in the following figures.

Starting with the momentum distributions in figure 3.3[1]. We can see the expected $p = 160$ GeV peak and identify the *beam halo* as the non-Gaussian tail of the distribution.

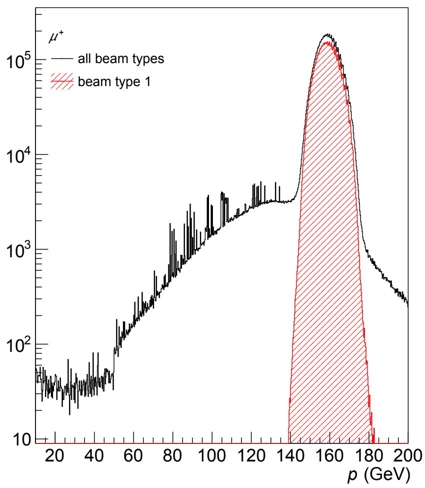

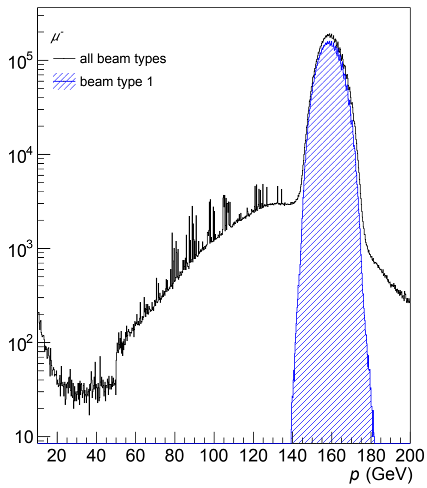

Figure 3.3: Beam type 1 momentum distribution extrapolated to $Z = 0$ cm (denoted p) with expected peaks at $p = 160$ GeV for (left) μ^+ and (right) μ^-

The 2D XY profiles of the *true beam* (beam type 1) extrapolated to reference points $Z = 0$ cm and $Z = 3000$ cm are given in figures 3.4 and 3.5 respectively. The 2D Gaussian fit with function

$$f(X, Y) = I_0 \exp\left(-\frac{(X - X_0)^2}{2\sigma_X^2} - \frac{(Y - Y_0)^2}{2\sigma_Y^2}\right) \tag{3.1}$$

was performed on the histograms and the results of the fit are given in table 3.4. The beam is at $Z = 3000$ cm slightly shifted towards positive x due to the magnetic field.

[1] Histograms of momentum distributions are normalized to the number of all beam tracks (for statistics see table 3.3 with the distribution of beam types)

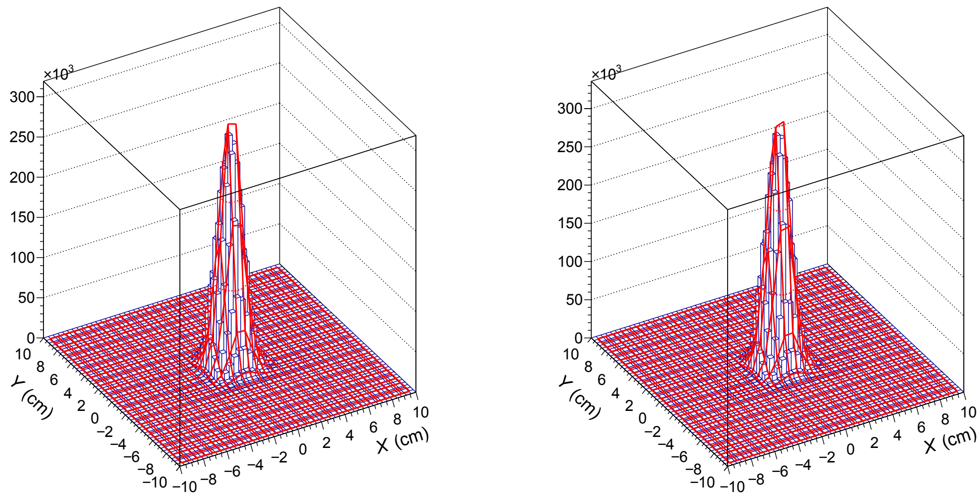

Figure 3.4: Beam type 1 counts in XY plane extrapolated to $Z = 0$ cm fitted with 2D Gaussian (red) for (left) μ^+ and (right) μ^-

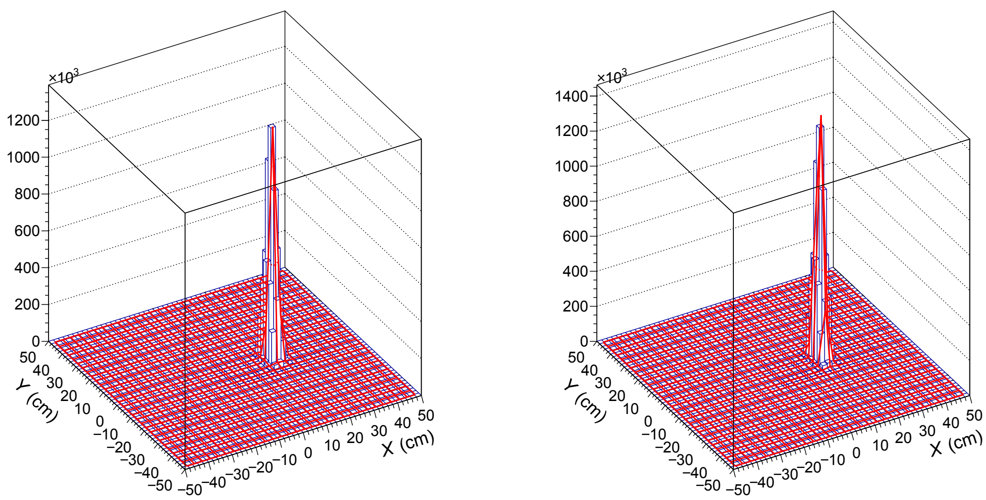

Figure 3.5: Beam type 1 counts in XY plane extrapolated to $Z = 3000$ cm fitted with 2D Gaussian (red) for (left) μ^+ and (right) μ^-

Table 3.4: Parametrs of the 2D Gaussian fit of the *beam core*

	μ^+		μ^-	
parameter	$Z = 0$ cm	$Z = 3000$ cm	$Z = 0$ cm	$Z = 3000$ cm
I_0	320480(140)	1436000(700)	338200(200)	1525400(700)
X_0/ cm	-0.0137(3)	15.1152(5)	0.0110(3)	15.0588(5)
σ_X/ cm	0.8179(2)	1.5244(3)	0.8058(2)	1.4740(3)
Y_0/ cm	-0.1643(3)	-0.6440(9)	-0.1560(3)	-0.6523(8)
σ_Y/ cm	0.8085(2)	2.4049(4)	0.7976(2)	2.3805(4)

The variance of the Gaussian for our 2017 data sample is approximately 1 mm larger than the value 7 mm given for the 2004 beam in section 2.1.1. Beam settings are slightly modified for each run and considering the dimensions of the target, 8 mm is a suitable beam variance. The results of the fitting procedure from table 3.4 were also used to calculate beam divergence D in both X and Y directions with the following equation:

$$D = 2 \arctan \left(\frac{\sigma_1 - \sigma_0}{Z_1 - Z_0} \right) , \tag{3.2}$$

denoting σ_0 and σ_1 the variances at reference points $Z_0 = 0$ cm and $Z_1 = 3000$ cm respectively. Calculated divergences for μ^+ and μ^- are given in table 3.5. The results show inhomogeneous divergence in X and Y direction, which is caused by the magnetic field. The larger divergence, which is in both cases in Y direction, matches the value 1 mrad from 2004 measurements considering that no uncertainty was provided by the source (see 2.1.1).

Table 3.5: Calculated divergences in X and Y directions of the μ^+ and μ^- beam

	D_X/ mrad	D_Y/ mrad
μ^+	0.4710(2)	1.0643(2)
μ^-	0.4455(2)	1.0553(2)

4. Measurement of the azimuthal asymmteries

4.1 Data samples

Data samples from 2016 periods 4–10 have been used in this analysis. Specifically, slot 8 data production of real data was used to extract *raw* asymmetries (denotes evaluated asymmetries before correction on acceptance). For period 10 slot 8 data production is not available, so slot 7.1 was used instead. No known changes took place between periods 8, 9 and 10.

Used datafiles in .root format can be found in CERN's storage *eos*, path to the micro Data Summary Trees (uDSTs) is ('$*$' represents period number):

```
/eos/experiment/compass/uDST_prod/dvcs2016P0*s8/
/eos/experiment/compass/uDST_prod/dvcs2016P10s7.1/
```

For acceptance correction, s7g3r3 *LEPTO* MC production was used with a few exceptions. Both μ^+ and μ^- MC samples for periods 8 and 9 were studied and due to their compatibility merged together. Merged MC samples (one for each muon charge) were used for acceptance correction of both periods 8 and 9. Period 10 was also corrected on acceptance with merged MC samples from P08 and P09, because there were no MC samples available for period 10 at the time of making this analysis and period 10 was found compatible with periods 8 and 9. Path to the MC samples is (`#` represents character `+` or `-` and `*` period number):

```
/eos/experiment/compass/mc/production/reco/2016/P0*/mu#_lepto_s7g3r3/mDST/
```

For P07, the MC sample was labeled s6g2r2, although there were no significant differences to s7g3r3. The path to this sample is:

```
/eos/experiment/compass/mc/production/reco/2016/P07/mu#_lepto_s6g2r2/mDST/
```

4.2 Selection of events and hadrons

For the DIS process, the selection of events is usually done with cuts, which are listed and briefly explained in the following paragraphs.

First, we demand the presence of a primary vertex in the event. If more than one primary vertex is found in the event, the vertex marked as *the best* by Phast (the highest number of outgoing tracks and if equal, the lower vertex χ^2) is selected. The position of the primary vertex needs to be in the target. Dimensions of the target cut are [1] -325 cm $< Z_{\mathrm{vertex}} < -71$ cm, $Y_{\mathrm{vertex}} < 1.2$ cm, $|\boldsymbol{R}_{\mathrm{vertex}}| < 1.9$ cm.

Next, the cuts on the beam are made starting with momentum cut (denoting P_μ the size of incoming muon momentum) 140 GeV $< P_\mu <$ 160 GeV. Incoming

[1] Position of the primary vertex target is given by the radius vector defined as $\boldsymbol{R}_{\mathrm{vertex}} = \big(X_{\mathrm{vertex}} - X_0(Z_{\mathrm{vertex}}), Y_{\mathrm{vertex}} - Y_0(Z_{\mathrm{vertex}})\big)$, coordinates $X_0(Z_{\mathrm{vertex}})$ and $Y_0(Z_{\mathrm{vertex}})$ represent vertex axis position

muon momentum error is acceptable only if $\sigma_{P_\mu} < 4$ GeV to avoid events with no reconstructed momentum by BMS. The condition on reduced chi-squared of the fitted μ track is $\frac{\chi^2}{n_{\mathrm{df}}} < 10$. The extrapolation of the beam track is also required to cross the whole target length.

To identify scattered muon (μ'), Phast has implemented the class PaHodoHelper with the function iMuPrim. In addition to the older iMuPrim function implementation in the PaVertex class, Hodohelper checks inactive slabs of hodoscopes to get a more precise selection. The event is rejected also if more candidates for the scattered muon are found. The scattered muon track is then required to have the first associated hit in a detector before SM1 magnet and the last hit after SM1 and the reduced chi-squared again needs to satisfy $\frac{\chi^2}{n_{\mathrm{df}}} < 10$. If another reconstructed track of particle with the same charge as the scattered muon has Z_{Last} downstream of MF2, then the event is also rejected (Z_{first} and Z_{last} denote the positions of the first and the last hit detected by spectrometer).

Cuts defining the kinematic range, where the description of the nucleon structure in terms of the TMD-PDFs is expected to be valid and where the experimental acceptance is good, are called standard DIS cuts and are given with inequalities: $Q^2 > 1$ GeV^2, $W > 5$ GeV, $0.003 < x < 0.130$, $0.1 < y < 0.9$ and condition on the angle between virtual photon momentum and incoming muon momentum in laboratory system $\theta_\gamma < 60$ mrad.

The final event cut is a trigger selection. We require at least one of the following triggers: MT, LT, OT, and LAST to be fired (for definitions see 2.4).

The effect of the event cuts on analyzed data is shown in table 4.1.

Table 4.1: Effect of the event cuts on each analysed period of 2016 data (number on the top of each row corresponds to the number of events, number on the bottom is events percentage)

cut	P10	P09	P08	P07	P06	P05	P04
All events	12773840 100.00	13017007 100.00	16617186 100.00	15737708 100.00	12223479 100.00	13009047 100.00	14290645 100.00
events with BPV	12773840 100.00	13017007 100.00	16617186 100.00	15737708 100.00	12223479 100.00	13009047 100.00	14290645 100.00
BPV in target	6803535 53.26	6970109 53.55	8874845 53.41	8497923 54.00	6607665 54.06	7034839 54.08	7725395 54.06
$\sigma_{P_\mu} < 4$ GeV	6803535 53.26	6970109 53.55	8874845 53.41	8497923 54.00	6607665 54.06	7034839 54.08	7725395 54.06
140 GeV$< P_\mu <$ 180 GeV	6803417 53.26	6969993 53.55	8874694 53.41	8497774 54.00	6607600 54.06	7034740 54.08	7725304 54.06
μ track $\frac{\chi^2}{n_{\mathrm{df}}} < 10$	6803377 53.26	6969970 53.55	8874657 53.41	8497743 54.00	6607564 54.06	7034691 54.08	7725248 54.06
μ crosses the whole target	6578928 51.50	6744182 51.81	8583811 51.66	8240408 52.36	6415555 52.49	6829021 52.49	7497076 52.46
iMuPrime (Hodohelper)	5201670 40.72	4627051 35.55	5762944 34.68	5441291 34.57	4242129 34.70	4478749 34.43	4926769 34.48
μ' track $\frac{\chi^2}{n_{\mathrm{df}}} < 10$	5199698 40.71	4625814 35.54	5761368 34.67	5439824 34.57	4240781 34.69	4477317 34.42	4924775 34.46
$Z_{\mathrm{First}} < 3, 5$ m $< Z_{\mathrm{Last}}$	5184179 40.58	4624542 35.53	5759809 34.66	5438421 34.56	4239560 34.68	4475364 34.40	4922633 34.45
$Z_{\mathrm{Last}} < 33$ m and $Q \neq Q_{\mu'}$	5184179 40.58	4624542 35.53	5748845 34.60	5438421 34.56	4239560 34.68	4475364 34.40	4922633 34.45
$Q^2 > 1$ GeV^2	4128444 32.32	3720860 28.58	4666608 28.08	4369904 27.77	3406475 27.87	3570447 27.45	3902069 27.31
W >5 GeV	2225142 17.42	1920022 14.75	2407020 14.49	2295852 14.59	1807811 14.79	1879681 14.45	2063744 14.44
$0.003 < x < 0.130$	2089992 16.36	1795766 13.80	2256755 13.58	2151357 13.67	1694044 13.86	1768066 13.59	1941317 13.58
$0.1 < y < 0.9$	1914715 14.99	1637070 12.58	2061623 12.41	1960258 12.46	1539556 12.60	1603321 12.32	1753369 12.27
$\theta < 60$ mrad	1624925 12.72	1370855 10.53	1721363 10.36	1649302 10.48	1295091 10.60	1349799 10.38	1475507 10.32
trigger cut	1624925 12.72	1370855 10.53	1721363 10.36	1649302 10.48	1295091 10.60	1349799 10.38	1475507 10.32

The event selection is followed by the hadron selection, which begins with selecting all charged particle tracks outgoing from the primary vertex and crossing material equivalent to less than 10 radiation lengths X_0 in the spectrometer (denoted as $\frac{X}{X_0} < 10$). Hadron needs to have the first hit before SM1 and the last hit after SM1 (SM1 position is at $Z = 350$ cm). Kinematic cuts on hadrons are 0.1 GeV $< P_T$ and $0.1 < z$. The 4-momentum P_h used to obtain z according to the equation 1.10 is calculated assuming pion mass for all charged hadrons. P_T is defined as a norm of $\boldsymbol{P_T}$. Effects of the hadron cuts on the analyzed data are shown in table 4.2.

Table 4.2: Effect of the hadron cuts on each analyzed period of 2016 data (number on the top of each row corresponds to the number of events, number on the bottom is events percentage)

cut	P10	P09	P08	P07	P06	P05	P04
All outcoming tracks without μ'	4732426 100.00	3864022 100.00	4850830 100.00	4666831 100.00	3666485 100.00	3793674 100.00	4092690 100.00
$\frac{X}{X_0} < 10$	4681328 98.92	3833349 99.21	4811922 99.20	4629305 99.20	3636699 99.19	3762542 99.18	4037765 98.66
hadron track $\frac{\chi^2}{n_{\mathrm{df}}} < 10$	4600165 97.21	3778105 97.78	4749528 97.91	4568905 97.90	3587414 97.84	3712649 97.86	3986797 97.41
$Z_{\mathrm{First}} > 350$ cm	4589846 96.99	3769670 97.56	4738919 97.69	4558804 97.69	3579108 97.62	3704574 97.65	3977769 97.19
$Z_{\mathrm{Last}} < 350$ cm	4454706 94.13	3661491 94.76	4604309 94.92	4430093 94.93	3474162 94.75	3595502 94.78	3857672 94.26
$0.1 < z < \infty$	2249268 47.53	1878343 48.61	2369541 48.85	2262936 48.49	1773378 48.37	1848886 48.74	2003934 48.96
$0.1 < P_T < \infty$	2130552 45.02	1777338 46.00	2241385 46.21	2141198 45.88	1678157 45.77	1749520 46.12	1895354 46.31

The same selection of events is done for reconstructed MC. For the generated MC, we apply only the selection of vertices in the target and the kinematic cuts

4.3 Contribution of exclusive processes

Apart from hadrons produced in SIDIS, we also detect hadrons, which are decay products of vector mesons produced in the following diffractive process:

$$l(k) + N(P) \to l(k') + N(P') + V(P_V), \tag{4.1}$$

in which V represents vector meson and l and l' denote initial and final leptons with their 4-momenta in affiliated parentheses. Due to the helicity conservation in the interaction, the spin of the quark-antiquark pair that makes up the produced vector meson is aligned with the direction of motion of the meson causing an anisotropic decay into hadrons with a high azimuthal modulation without origin in SIDIS [29]. Especially in the high z region, this effect influences the measured SIDIS asymmetries if only standard DIS selection is applied, because it does not distinguish products of the decay of diffractive vector mesons from the SIDIS hadrons.

Identification of events including exclusive processes instead of SIDIS is simple in the case of detection and successful reconstruction of both two (and only two) hadrons of opposite charges produced due to the process 4.1. Denoting z_{tot} as a sum of z_1 of the first hadron and z_2 of the second hadron, such exclusive events are selected requiring $z_{\mathrm{tot}} > 0.95$ and are excluded from the analysis. The effect of this cut is shown in table 4.3 and in figure 4.1.

Table 4.3: Effect of the cut on hadrons produced in exclusive processes for each analyzed period of 2016 data (number on top of each row corresponds to the number of hadrons, number on the bottom is a percentage)

	P10	P09	P08	P07	P06	P05	P04
hadrons after selection	2130552	1777338	2241385	2141198	1678157	1749520	1895354
	100.00	100.00	100.00	100.00	100.00	100.00	100.00
after cut $z_{\text{tot}} < 0.95$	2096775	1746840	2202964	2104676	1649821	1720286	1862993
	98.41	98.28	98.29	98.29	98.31	98.33	98.29
cut hadrons	33777	30498	38421	36522	28336	29234	32361
	1.59	1.72	1.71	1.71	1.69	1.67	1.71

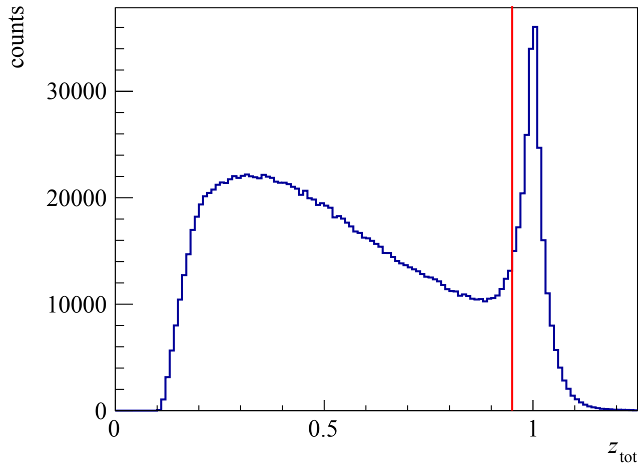

Figure 4.1: Histogram of z_{tot} of events from all analyzed periods with two detected hadrons of opposite charges, vertical line corresponds to cut $z_{\text{tot}} > 0.95$

When only 1 of the 2 hadrons is detected, the correction cannot be done on the event-by-event basis. Instead, the contribution estimated from *HEPGEN* MC could be subtracted. In theory, the cross-section of producing a diffractive vector meson in process 4.1 is significant only for the following three vector mesons: $\rho^0(770)$, $\omega(782)$ and $\phi(1020)$. However, the procedure of subtraction is usually done only for $\rho^0(770)$ and ϕ, while the contribution of $\omega(782)$ was experimentally found to be negligible [30]. Subtraction using *HEPGEN* MC samples was not done in this analysis due to time constraints. However, in about 70% of cases both hadrons are reconstructed [31], so the main part of the correction is taken into account by the aforementioned cut.

4.4 Binning and kinematic range

Binning for this analysis was chosen according to previous releases and published papers. Limits for kinematic variables for 1D and 3D analysis of the azimuthal asymmetries as well as for studies of Z_{vertex} dependence are given in tables 4.4, 4.5 and 4.6. The studies of the vertex dependence were done in bins of x, using both 1D and 3D binning in x.

Table 4.4: Binning used in 1D azimuthal asymmetries analysis

bin no.		1		2		3		4		5		6→
x	0.003	–	0.008	–	0.013	–	0.020	–	0.032	–	0.050	–
z	0.10	–	0.20	–	0.25	–	0.30	–	0.34	–	0.38	–
P_T/ GeV	0.10	–	0.20	–	0.27	–	0.33	–	0.39	–	0.46	–
bin no.	→	7		8		9		10				
x	0.080	–	0.130									
z	0.42	–	0.49	–	0.63	–	0.85					
P_T/ GeV	0.55	–	0.64	–	0.77	–	1.00	–	1.73			

Table 4.5: Binning used in 3D azimuthal asymmetries analysis

bin no.		1		2		3		4→
x	0.003	–	0.012	–	0.020	–	0.038	–
z	0.10	–	0.20	–	0.25	–	0.32	–
P_T/ GeV	0.10	–	0.30	–	0.50	–	0.64	–
bin no.	→	5		6		7		
x	0.130							
z	0.40	–	0.55	–	0.70	–	0.85	
P_T/ GeV	1.00	–	1.73					

Table 4.6: Binning in Z_{vertex} used in systematic studies

bin no.		1		2		3		4	
Z_{vertex}/ cm	-325	–	-251	–	-191	–	-131	–	-71

The kinematic range previously set by standard DIS cuts described in section 4.2 was narrowed down to match previous releases and papers with the following set of additional conditions:

1. For the study of vertex dependence:

$$\begin{aligned} 0.2 < y < 0.9 \\ 0.2 < z < 0.85 \\ 0.1\ \text{GeV} < P_T < 1.73\ \text{GeV} \\ -351\ \text{cm} < Z_{\text{vertex}} < -71\ \text{cm} \end{aligned} \tag{4.2}$$

2. For asymmetries in 3D binning:

$$\begin{aligned} 0.2 < y < 0.9 \\ 0.1 < z < 0.85 \\ 0.1\ \text{GeV} < P_T < 1.73\ \text{GeV} \\ -251\ \text{cm} < Z_{\text{vertex}} < -71\ \text{cm} \end{aligned} \tag{4.3}$$

3. For asymmetries in 1D binning

$$\begin{aligned}
0.2 < y &< 0.9 \\
0.2 < z &< 0.85 \text{ for } P_T \text{ and } x \text{ binning} \\
0.1 < z &< 0.85 \text{ for } z \text{ binning} \\
0.1 \text{ GeV} < P_T &< 1.73 \text{ GeV} \\
-251 \text{ cm} < Z_{\text{vertex}} &< -71 \text{ cm}
\end{aligned} \tag{4.4}$$

4.5 Kinematic distributions and comparison with reconstructed MC samples

To show the compatibility between real data and reconstructed MC, which is used for acceptance corrections, we provide the following figures 4.2-4.7 with a comparison between the dataset's kinematic variables for both hadron charges. The kinematic range of plotted events corresponds to standard DIS cuts described in section 4.2. Products of visible decays of exclusively produced vector mesons were not included in the plots, as described in section 4.3.

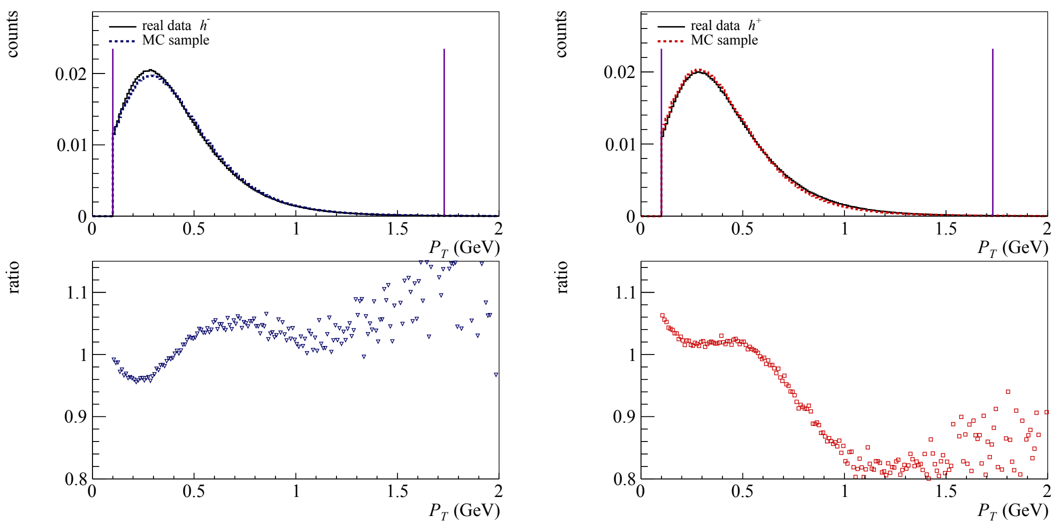

Figure 4.2: P_T distribution of positive negative (left) and positive (right), vertical lines correspond to additional cut 0.1 GeV $< P_T <$ 1.75 GeV

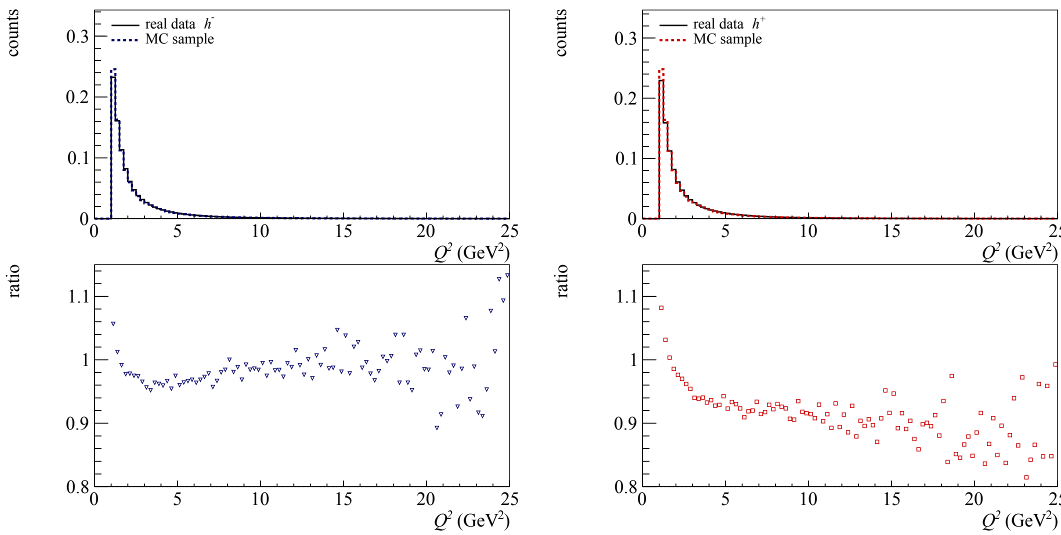

Figure 4.3: Q^2 distribution of negative (left) and positive (right) hadrons

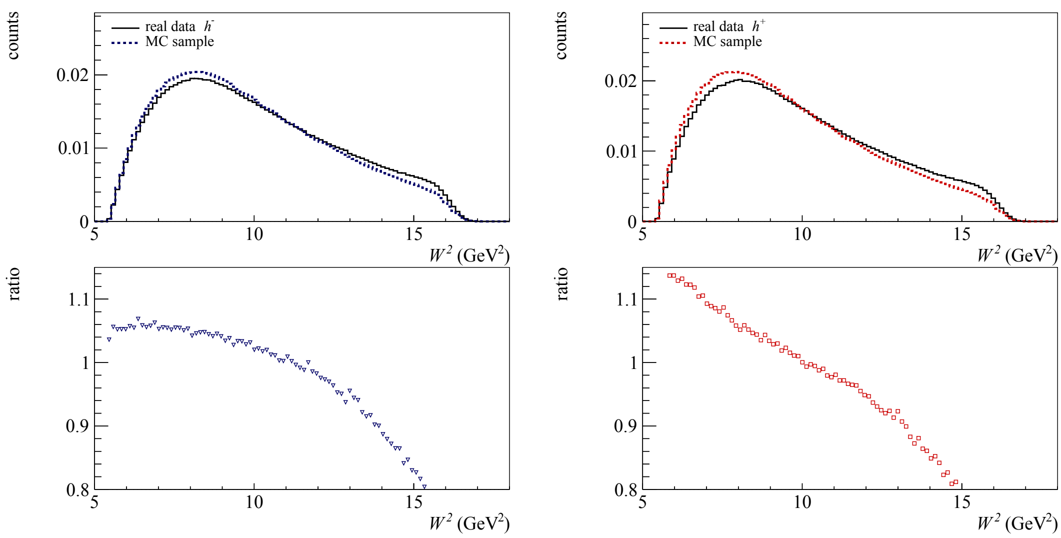

Figure 4.4: W^2 distribution of negative (left) and positive (right) hadrons

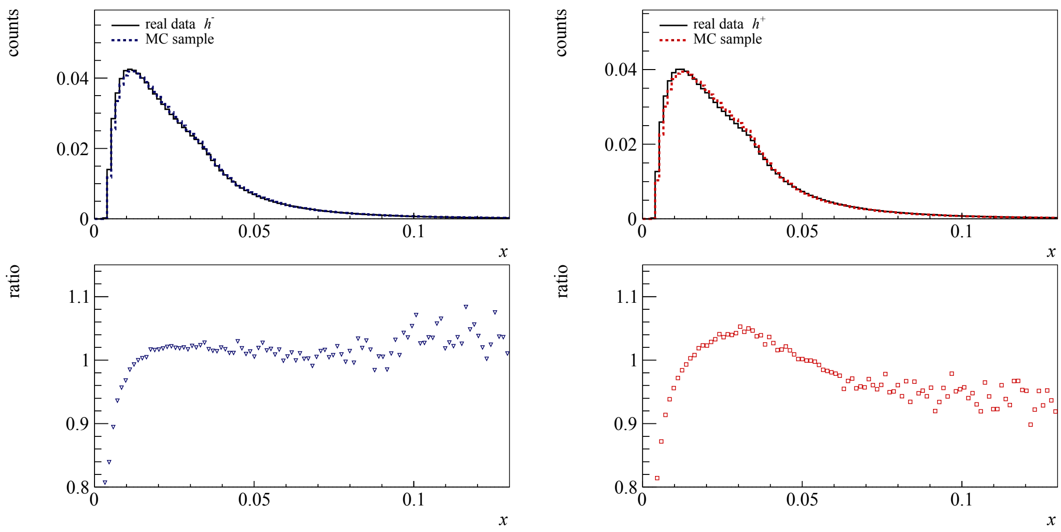

Figure 4.5: x distribution of negative (left) and positive (right) hadrons

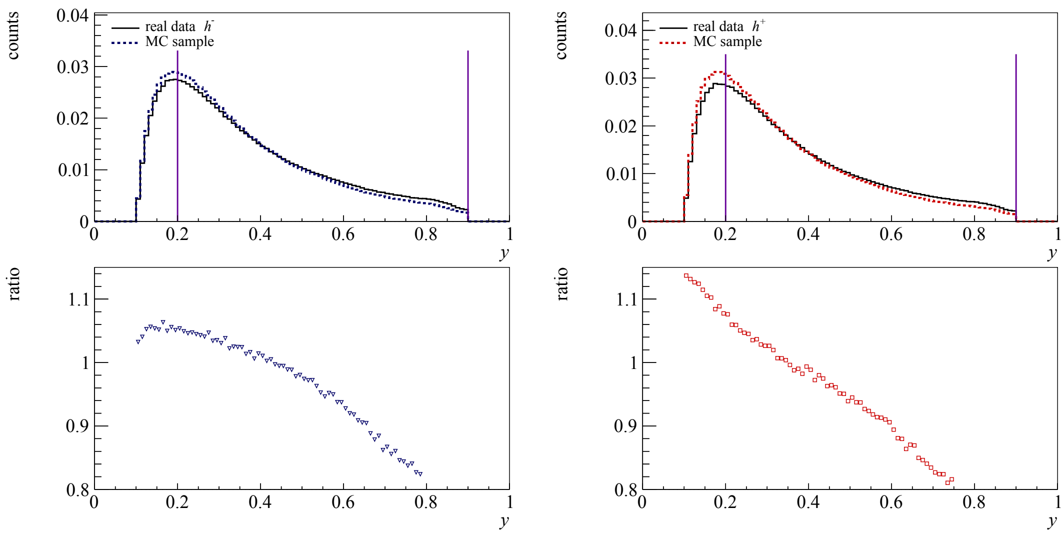

Figure 4.6: y distribution o negative (left) and positive (right) hadrons, vertical lines correspond to additional cut $0.2 < y < 0.9$

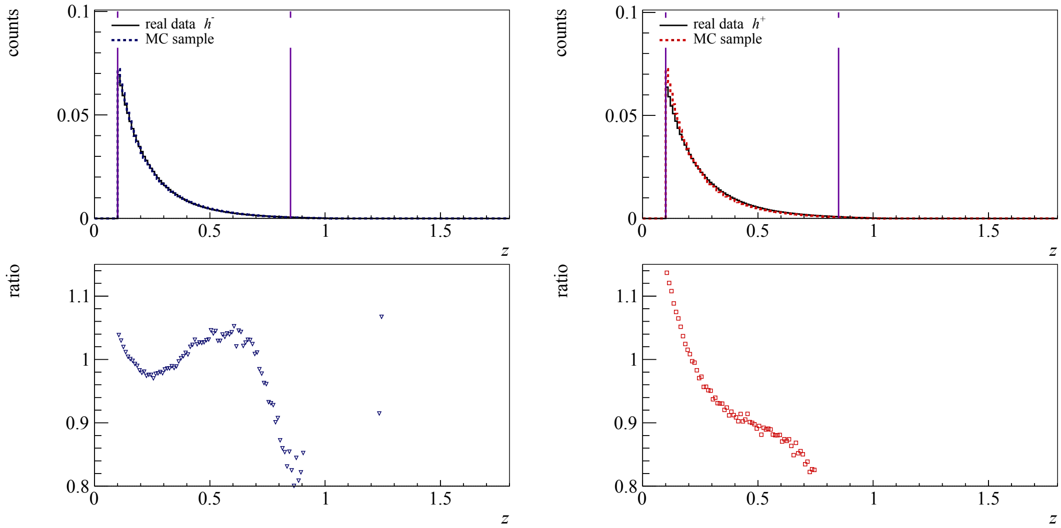

Figure 4.7: z distribution of negative (left) and positive (right) hadrons, vertical lines correspond to additional cut $0.1 < z < 0.85$

From figures 4.2-4.7 we conclude that profiles of the kinematic variables for real data and reconstructed MC are not equivalent, however, their ratios in chosen kinematic ranges are mostly between 0.9–1.1, rarely exceeding this range up to 0.8–1.2. This disagreement, which is most visible in y and W^2 distributions, can be caused by not including radiative corrections while generating the MC samples.

In figure 4.8 2D histograms showing correlation x-Q^2 and z-P_T are shown for the same kinematic range as in the previous figures 4.2-4.7.

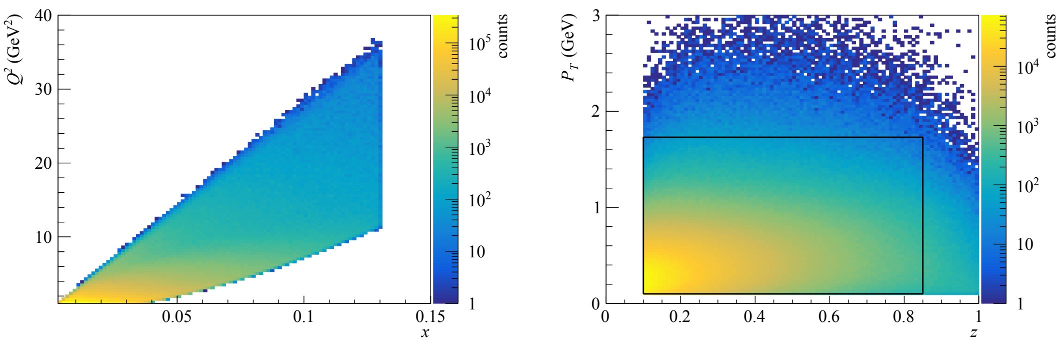

Figure 4.8: x-Q^2 (left) and z-P_T (right) correlation, rectangle corresponds to cuts $0.1 < z < 0.85$ and 0.1 GeV $< P_T < 1.75$ GeV

4.6 Acceptance correction

Acceptance correction is a method to account for the spectrometer's finite dimensions and efficiency, which cause an undetected fraction of scattered particles. This fraction is angular dependent, which results in false (non-physical) modulations of the ϕ_h distributions. Correction for the acceptance is a process that tries to evaluate this fraction (denoted a and called *acceptance*) for each ϕ_h bin and scale the bin content with $\frac{1}{a}$ removing the false asymmetries in the process.

The acceptance is obtained using MC samples. Denoting N_{rec} the bin content in ϕ_h histogram of reconstructed MC and N_{gen} the same bin content in histogram before the given MC sample was reconstructed, we can define the acceptance as:

$$a = \frac{N_{\mathrm{rec}}}{N_{\mathrm{gen}}}. \tag{4.5}$$

The error of bin content of the reconstructed MC histogram is assumed to be zero, thus the error of acceptance is given only by the error of reconstructed MC, which follows Poisson distribution with error $\sigma_{N_{\mathrm{rec}}} = \sqrt{N_{\mathrm{rec}}}$. Expression for acceptance error is therefore

$$\sigma_a = \frac{\sqrt{N_{\mathrm{rec}}}}{N_{\mathrm{gen}}}. \tag{4.6}$$

4.7 Fitting procedure

The cross-section of the SIDIS process is given in the equation 1.16. In this analysis the SIDIS cross-section as a function of ϕ_h in the following form:

$$\sigma(\phi_h) = p_0(1 + p_1 \cos\phi_h + p_2 \cos 2\phi_h + p_3 \sin\phi_h) \tag{4.7}$$

was fitted on the measured distributions of ϕ_h to evaluate coefficients $p_i,\ i \in \{0,1,2,3\}$ with corresponding errors $\sigma_{p_i},\ i \in \{0,1,2,3\}$ that are related to azimuthal asymmetries defined in section 1.2.1 in the following way:

$$A_{UU}^{\cos\phi_h} = \frac{p_1}{\varepsilon_1(y)}\ ,\ A_{UU}^{\cos 2\phi_h} = \frac{p_2}{\varepsilon_2(y)}\ ,\ A_{LU}^{\sin\phi_h} = \frac{p_3}{\lambda\varepsilon_3(y)}\ . \tag{4.8}$$

Since the statistic has been large enough, the statistical error of $\varepsilon_i(\langle y\rangle)$ has been estimated as negligible. Thus the statistical error of asymmetries derived from the errors of the fitted coefficient is given as:

$$\sigma_{A_{UU}^{\cos\phi_h}} = \frac{\sigma_{p_1}}{\varepsilon_1(y)}\ ,\ \sigma_{A_{UU}^{\cos 2\phi_h}} = \frac{\sigma_{p_2}}{\varepsilon_2(y)}\ ,\ \sigma_{A_{LU}^{\sin\phi_h}} = \frac{\sigma_{p_3}}{\lambda\varepsilon_3(y)}\ . \tag{4.9}$$

The distributions of ϕ_h in each kinematic bin defined in section 4.4 were obtained by filling histograms with 32 bins in the range from $-\pi$ to π. The central region defined by interval $(-\frac{\pi}{8}, \frac{\pi}{8})$ was excluded from the analysis due to the high contamination of the data by electrons and positrons with origin in the production of pairs $e^+\ e^-$ from bremsstrahlung photons, which were misidentified as hadrons. The effect of the central region cut is shown in figure 4.9 on full data in period 7 2016.

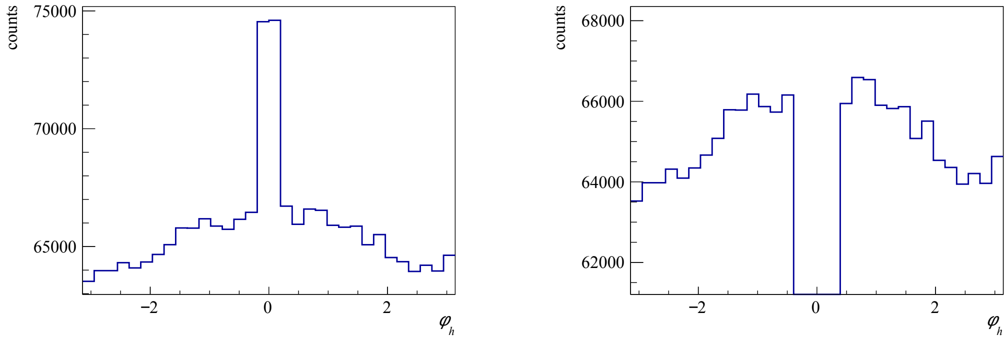

Figure 4.9: Distributions of ϕ_h for full P07 2016 before (left) and after (right) the central region cut

Distributions of y were obtained in the same manner and their mean values $\langle y\rangle$ were used to evaluate $\varepsilon_i(y),\ i \in \{1,2,3\}$. Considering the bin dependence, the mean value of the kinematic variable ($\langle x\rangle$, $\langle P_T\rangle$, or $\langle z\rangle$) in the given bin was also obtained and used in graphs as the coordinate on the abscissa. Note that for brevity the subscripts of asymmetries denoting beam and target polarizations are not written down in the following parts of this thesis.

4.8 Systematic uncertainty

To estimate the systematic uncertainty we provide the following check of the period statistical compatibility in subsection 4.8.1 and a study of the vertex dependence in subsection 4.8.2. A significant contribution to the systematic uncertainty was estimated from both studied systematic effects. In the final evaluation of the total uncertainty, these contributions are added in quadrature.

4.8.1 Period compatibility in 1D and 3D binning

To give an estimation of the contribution to the systematic uncertainty from the period incompatibility, several tests to check the statistical compatibility of measured asymmetries were performed.

First, the compatibility among the results[2] A_i obtained in each period with each μ charge setting in every studied bin has been checked using *pulls* defined as:

$$\Delta A_i = \frac{A_i - A}{\sqrt{\sigma^2_{A_i} - \sigma^2_A}}\ . \tag{4.10}$$

As the data are expected to be normally distributed around their statistically-weighted average, the pulls are also expected to follow the normal distribution with a mean value of 0 and variance of 1. Histograms of the pulls from all the x, z or P_T bins separately in 1D binning or only x bins in 3D binning were therefore

[2] A represents all three asymmetries $A^{\cos\phi_h}$, $A^{\cos 2\phi_h}$ and $A^{\sin\phi_h}$ which are processed in the same manner

fitted with Gaussians. Parameters of the fits (mean value $\mu = \mu_{\text{pulls}}$ and variance $\sigma = \sigma_{\text{pulls}}$) were written directly in the histogram plots.

The second tool to check the compatibility of the results in the periods is p-value, which was obtained from Pearson's χ^2 test of a constant fit through the asymmetries A_i obtained in the specific bin for all 7 periods or for each vertex bin. The p-value represents the probability that obtaining the result with a given or higher χ^2 occurs just by chance. For larger data samples we expect the p-values to be uniformly distributed between 0 and 1 and if we choose a level of significance as $p = 0.05$, the fraction of the bins satisfying $p < 0.05$ should not exceed the level of significance for the data to be considered compatible.

The results of the compatibility check are shown in the following subsections. The final contribution to the systematic uncertainty from the period incompatibility was estimated as:

$$\frac{\sigma_{A,\text{sp}}}{\sigma_{A,\text{stat}}} = \sqrt{\max(\{0, \sigma^2_{\text{pulls}} - 1\})} + |\mu_{\text{pulls}}| \; . \tag{4.11}$$

Period compatibility in 1D binning

In 1D binning, we checked the compatibility of the results in periods. Graphs of p-values are in figure 4.10 and table 4.7 evaluates compatibility according to the number of bins under the chosen level of significance $p = 0.05$. The distribution of p-values is uniformly distributed between values 0 and 1 with a maximum (in P_T binning) of 12% bins satisfying $p < 0.05$. Pulls calculated for positive hadrons are in figure 4.11 and for negative hadrons in figure 4.12. Contribution of the period compatibility to the systematic error is evaluated for x, z or P_T bins separately and listed in tables 4.8–4.10. We consider the observed compatibility to be good, which is reflected in the maximum value of the systematic uncertainty assigned by the formula 4.11 of $\sigma_{A,\text{sp}} = 0.78\sigma_{A_i,\text{stat}}$. The correlation between bad p-value statistics and larger systematic error contribution in a given bin is also visible.

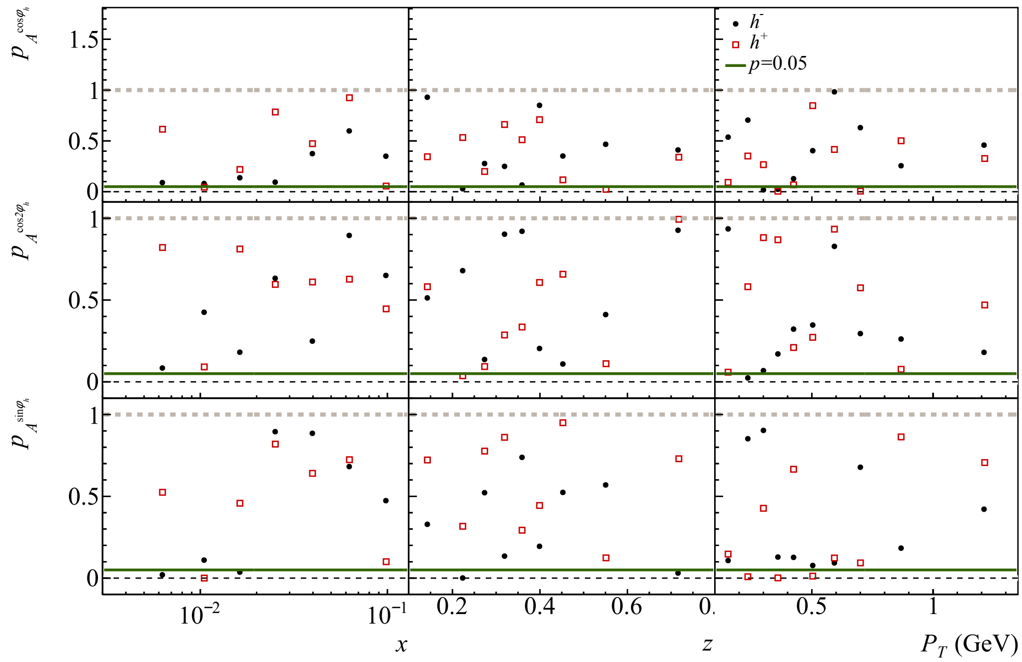

Figure 4.10: p-value for positive and negative hadrons in 1D binning

Table 4.7: $p < 0.05$ statistics in 1D binning (number on the top of each row corresponds to the number of bins, number on the bottom is bins percentage)

binning / hadron charge	x h^-	x h^+	z h^-	z h^+	P_T h^-	P_T h^+	sum
$A^{\cos\phi_h}$	0 0.00	1 0.14	1 0.11	1 0.11	2 0.20	2 0.20	7 0.13
$A^{\cos 2\phi_h}$	0 0.00	0 0.00	0 0.00	1 0.11	1 0.10	0 0.00	2 0.04
$A^{\sin\phi_h}$	2 0.29	1 0.14	2 0.22	0 0.00	0 0.00	3 0.30	8 0.15
sum	4 0.10		5 0.09		7 0.12		

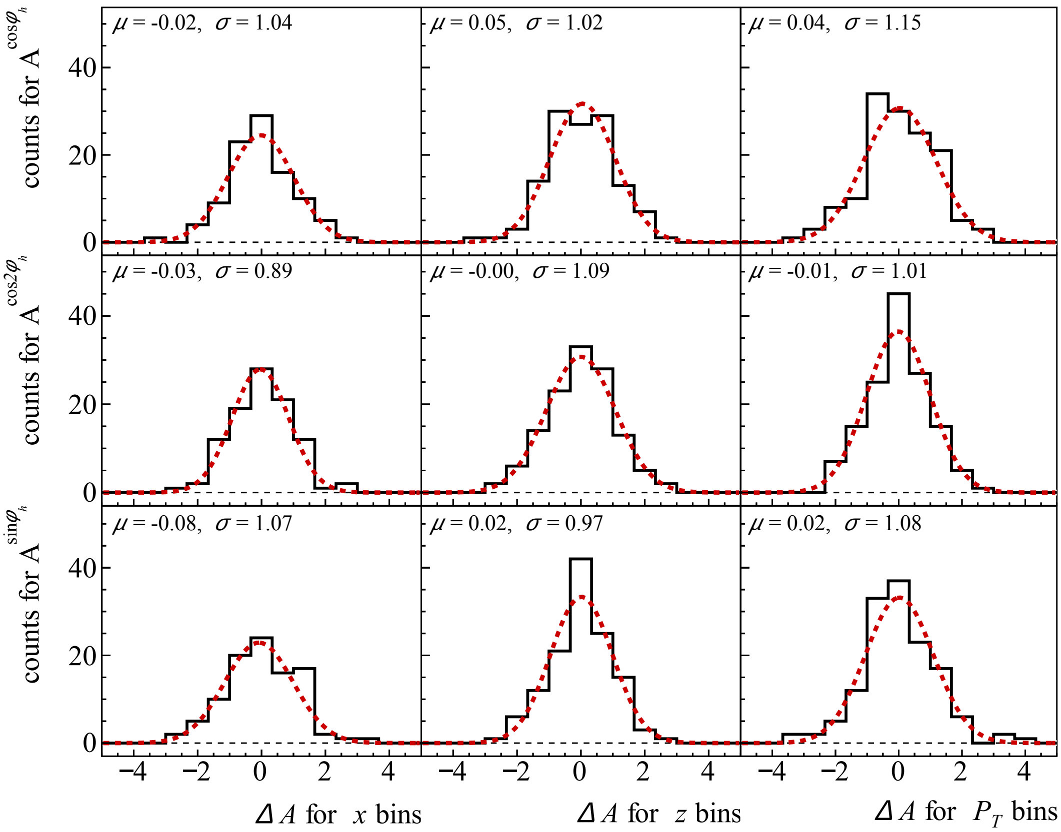

Figure 4.11: Pulls fitted with Gaussian (red-dashed) for positive hadrons in 1D binning

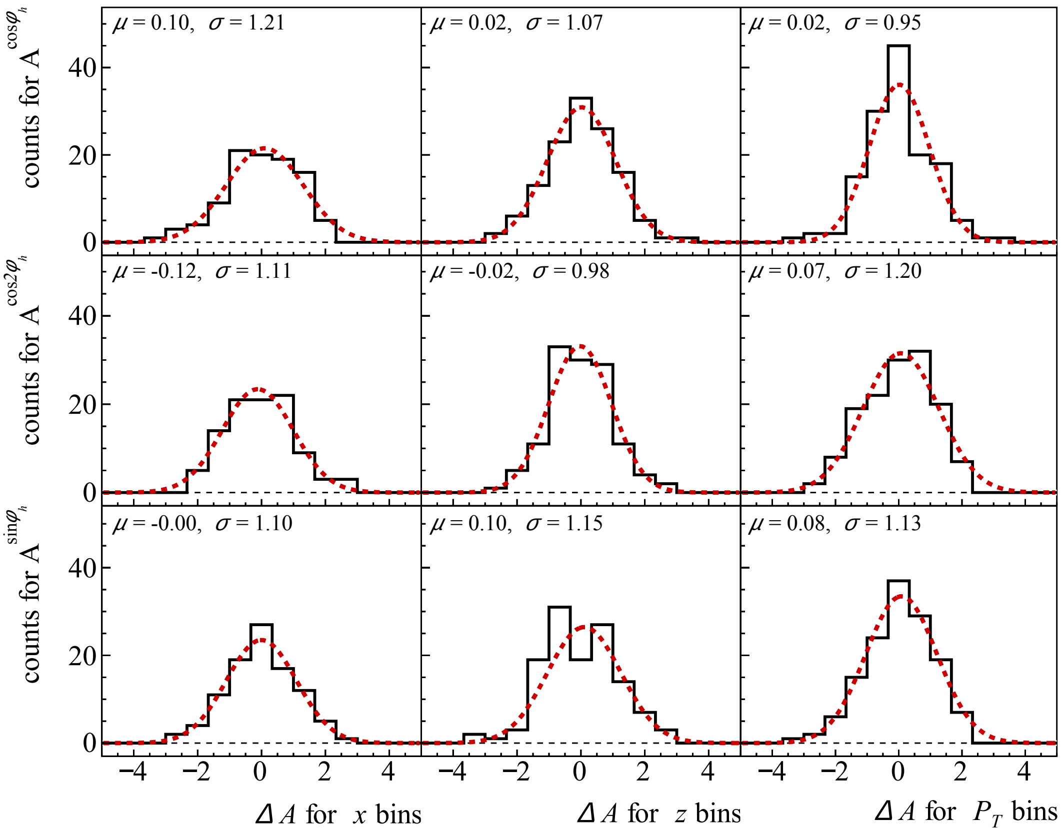

Figure 4.12: Pulls fitted with Gaussian (red-dashed) for negative hadrons in 1D binning

Table 4.8: Contribution of the period incompatibility to the systematic error for each 1D x bin ($\sigma_{A,\mathrm{sp}}$ rounded to 4 decimals)

x bin no.	1		2		3		4	
A	$\sigma_{A,\mathrm{sp}}$		$\sigma_{A,\mathrm{sp}}$		$\sigma_{A,\mathrm{sp}}$		$\sigma_{A,\mathrm{sp}}$	
	h^-	h^+	h^-	h^+	h^-	h^+	h^-	h^+
$A^{\cos\phi_h}$	0.0026	0.0009	0.0015	0.0005	0.0012	0.0004	0.0013	0.0004
$A^{\cos 2\phi_h}$	0.0044	0.0002	0.0023	0.0001	0.0018	0.0001	0.0020	0.0001
$A^{\sin\phi_h}$	0.0023	0.0022	0.0020	0.0019	0.0023	0.0021	0.0027	0.0024

x bin no.	5		6		7		all bins	
A	$\sigma_{A,\mathrm{sp}}$		$\sigma_{A,\mathrm{sp}}$		$\sigma_{A,\mathrm{sp}}$		$\frac{\sigma_{A,\mathrm{sp}}}{\sigma_{A_i,\mathrm{stat}}}$	
	h^-	h^+	h^-	h^+	h^-	h^+	h^-	h^+
$A^{\cos\phi_h}$	0.0017	0.0006	0.0021	0.0007	0.0034	0.0011	0.78	0.30
$A^{\cos 2\phi_h}$	0.0025	0.0001	0.0031	0.0002	0.0051	0.0002	0.58	0.03
$A^{\sin\phi_h}$	0.0035	0.0030	0.0044	0.0037	0.0061	0.0050	0.46	0.47

Table 4.9: Contribution of the period incompatibility to the systematic error for each 1D z bin ($\sigma_{A,\mathrm{sp}}$ rounded to 4 decimals)

z bin no.	1		2		3		4		5	
A	$\sigma_{A,\mathrm{sp}}$		$\sigma_{A,\mathrm{sp}}$		$\sigma_{A,\mathrm{sp}}$		$\sigma_{A,\mathrm{sp}}$		$\sigma_{A,\mathrm{sp}}$	
	h^-	h^+	h^-	h^+	h^-	h^+	h^-	h^+	h^-	h^+
$A^{\cos\phi_h}$	0.0003	0.0002	0.0006	0.0004	0.0007	0.0004	0.0009	0.0006	0.0011	0.0006
$A^{\cos 2\phi_h}$	0.0000	0.0006	0.0001	0.0012	0.0001	0.0014	0.0001	0.0018	0.0001	0.0020
$A^{\sin\phi_h}$	0.0014	0.0000	0.0027	0.0001	0.0033	0.0001	0.0043	0.0001	0.0050	0.0001

z bin no.	6		7		8		9		all bins	
A	$\sigma_{A,\mathrm{sp}}$		$\sigma_{A,\mathrm{sp}}$		$\sigma_{A,\mathrm{sp}}$		$\sigma_{A,\mathrm{sp}}$		$\frac{\sigma_{A,\mathrm{sp}}}{\sigma_{A_i,\mathrm{stat}}}$	
	h^-	h^+	h^-	h^+	h^-	h^+	h^-	h^+	h^-	h^+
$A^{\cos\phi_h}$	0.0012	0.0007	0.0011	0.0006	0.0011	0.0006	0.0014	0.0008	0.40	0.27
$A^{\cos 2\phi_h}$	0.0001	0.0022	0.0001	0.0020	0.0001	0.0019	0.0002	0.0024	0.02	0.42
$A^{\sin\phi_h}$	0.0057	0.0001	0.0051	0.0001	0.0050	0.0001	0.0054	0.0001	0.67	0.02

Table 4.10: Contribution of the period incompatibility to the systematic error for each 1D P_T bin ($\sigma_{A,\mathrm{sp}}$ rounded to 4 decimals)

P_T bin no.	1		2		3		4	
A	$\sigma_{A,\mathrm{sp}}$		$\sigma_{A,\mathrm{sp}}$		$\sigma_{A,\mathrm{sp}}$		$\sigma_{A,\mathrm{sp}}$	
	h^-	h^+	h^-	h^+	h^-	h^+	h^-	h^+
$A^{\cos\phi_h}$	0.0000	0.0013	0.0000	0.0013	0.0000	0.0014	0.0000	0.0013
$A^{\cos 2\phi_h}$	0.0036	0.0006	0.0037	0.0007	0.0037	0.0007	0.0037	0.0007
$A^{\sin\phi_h}$	0.0041	0.0026	0.0042	0.0027	0.0043	0.0027	0.0042	0.0027

P_T bin no.	5		6		7		8	
A	$\sigma_{A,\mathrm{sp}}$		$\sigma_{A,\mathrm{sp}}$		$\sigma_{A,\mathrm{sp}}$		$\sigma_{A,\mathrm{sp}}$	
	h^-	h^+	h^-	h^+	h^-	h^+	h^-	h^+
$A^{\cos\phi_h}$	0.0000	0.0013	0.0000	0.0012	0.0000	0.0013	0.0000	0.0013
$A^{\cos 2\phi_h}$	0.0035	0.0006	0.0033	0.0006	0.0037	0.0007	0.0037	0.0007
$A^{\sin\phi_h}$	0.0040	0.0026	0.0038	0.0024	0.0042	0.0027	0.0041	0.0026

P_T bin no.	9		10		all bins	
A	$\sigma_{A,\mathrm{sp}}$		$\sigma_{A,\mathrm{sp}}$		$\frac{\sigma_{A,\mathrm{sp}}}{\sigma_{A_i,\mathrm{stat}}}$	
	h^-	h^+	h^-	h^+	h^-	h^+
$A^{\cos\phi_h}$	0.0000	0.0014	0.0001	0.0017	0.02	0.60
$A^{\cos 2\phi_h}$	0.0039	0.0007	0.0051	0.0009	0.73	0.15
$A^{\sin\phi_h}$	0.0042	0.0026	0.0050	0.0032	0.60	0.42

Period compatibility in 3D binning

The following figures 4.16,4.13 and 4.19 show p-values evaluated in all 3D bins. Tables 4.15, 4.13 and 4.11 provide compatibility evaluation in the form of a number of bins under the level of significance, which was chosen as $p = 0.05$. Pulls calculated for positive hadrons are in figures 4.14,4.17,4.20 and for negative hadrons in figures 4.15,4.18,4.21[3]. We observed decreasing period compatibility in higher z bins in both p-values and pulls. No dependence on P_T was visible. Overall period compatibility in 3D bins is worse than in 1D binning with the largest contribution to the systematic error $\sigma_{A,\mathrm{sp}} = 1.49\sigma_{A,\mathrm{stat}}$ outreaching the statistical error.

[3]The order of the tables and figures was chosen to gather results of each asymmetry

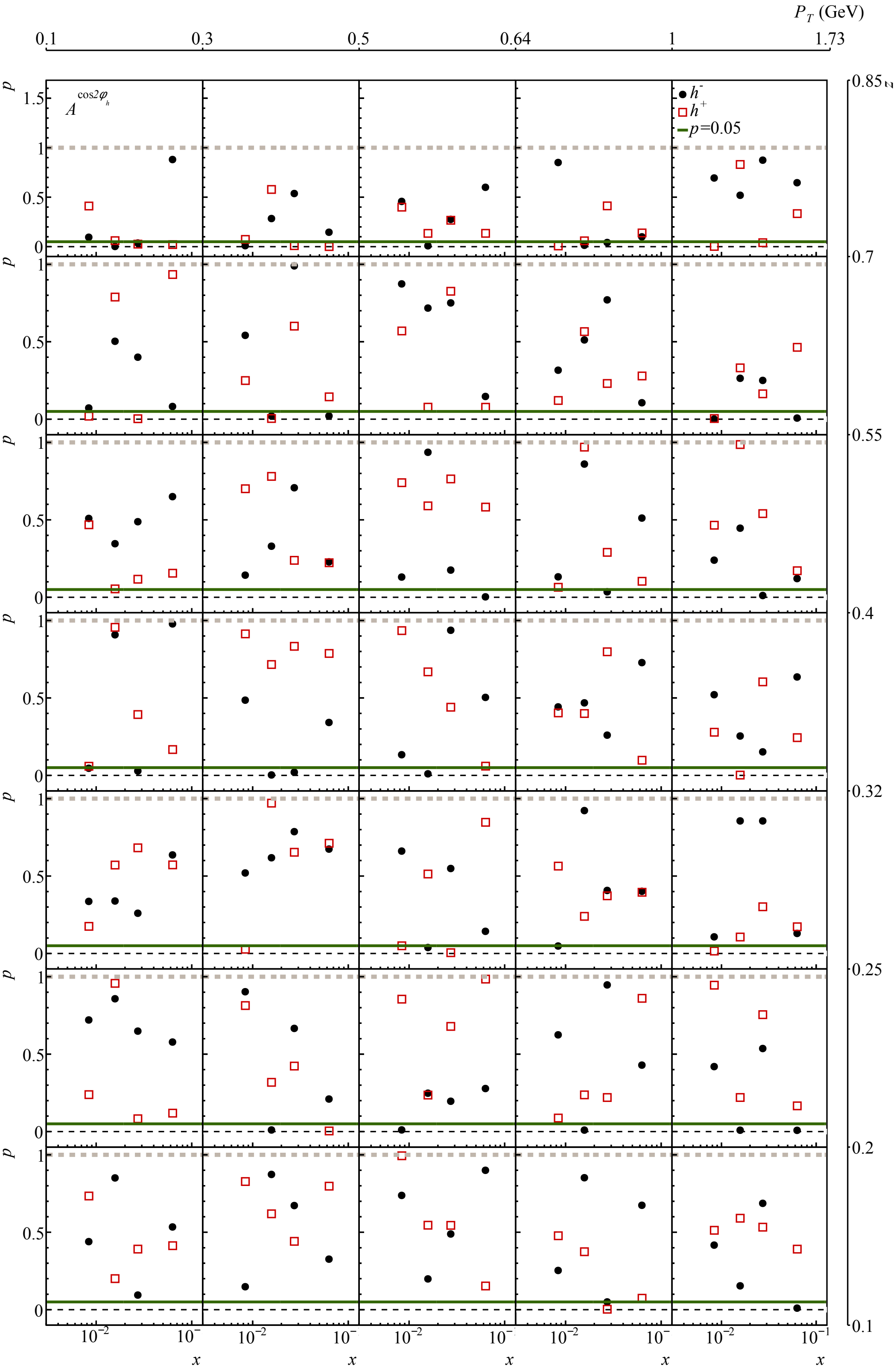

Figure 4.13: $A^{\cos 2\phi_h}$: p-value for positive and negative hadrons in 3D binning, green line corresponds to significance level $p = 0.05$

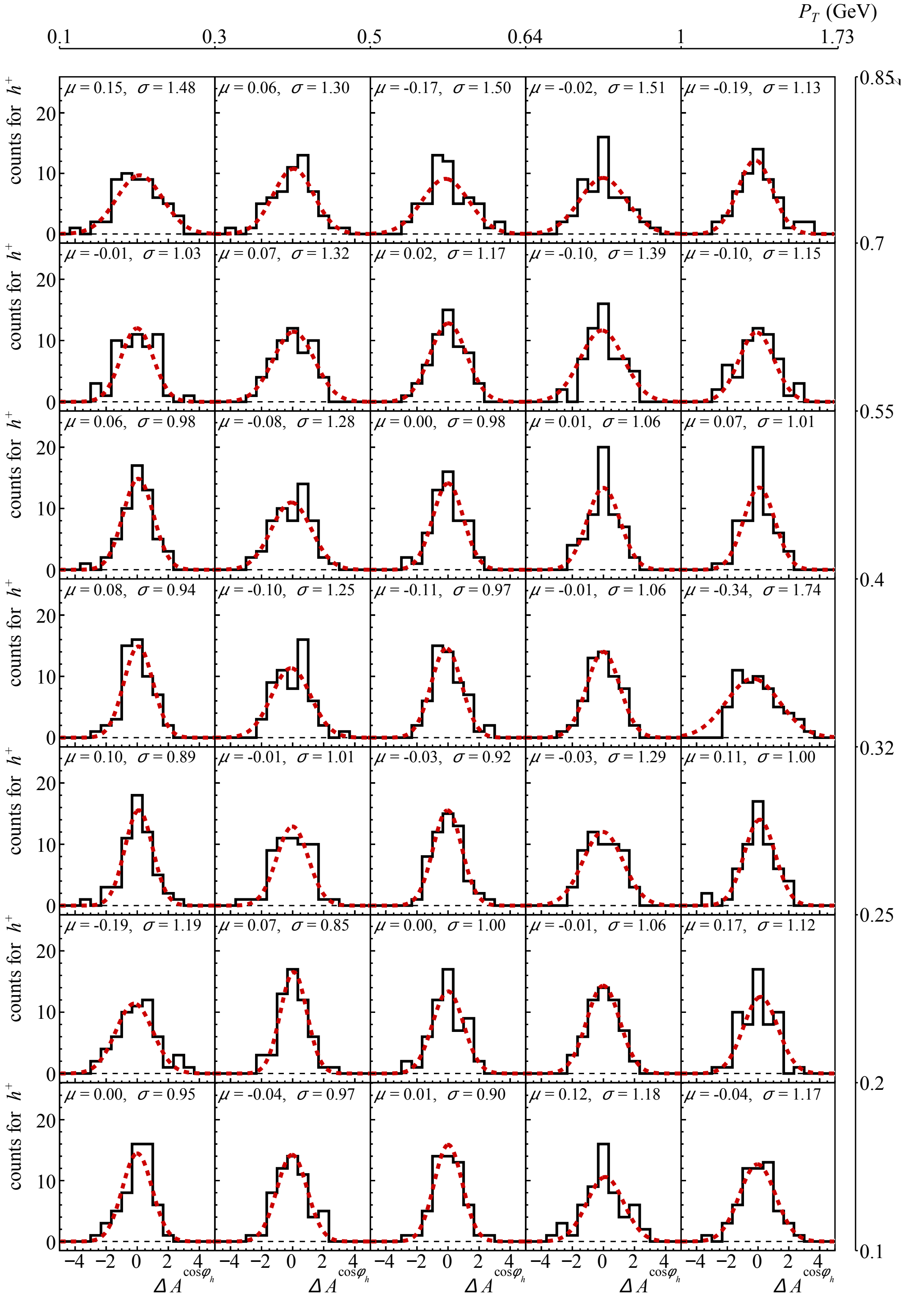

Figure 4.14: $A^{\cos\phi_h}$: pulls fitted with Gaussian (red-dashed) for positive hadrons in 3D binning

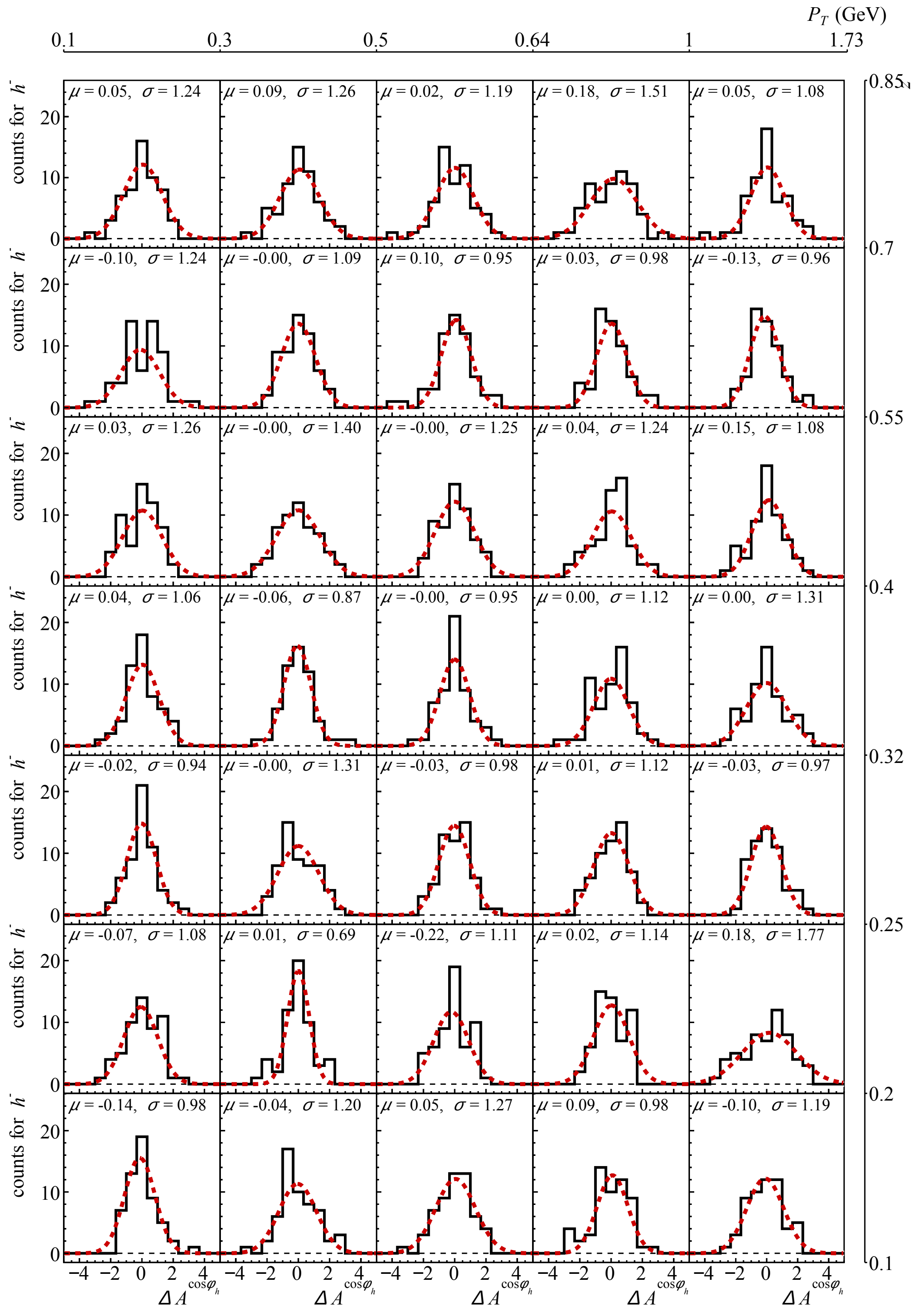

Figure 4.15: $A^{\cos\phi_h}$: pulls fitted with Gaussian (red-dashed) for negative hadrons in 3D binning

Table 4.11: $A^{\cos\phi_h}$: $p < 0.05$ statistics in 3D binning (numbers on the top of the row corresponds to the number of bins, numbers on the bottom are bins percentage)

z bin no./ P_T bin no.	1		2		3		4		5		sum
	h^-	h^+	h^-	h^+	h^-	h^+	h^-	h^+	h^-	h^+	
7	1 0.25	3 0.75	2 0.50	2 0.50	2 0.50	2 0.50	1 0.25	3 0.75	1 0.25	1 0.25	18 0.45
6	2 0.50	1 0.25	0 0.00	0 0.00	2 0.50	0 0.00	0 0.00	1 0.25	0 0.00	2 0.50	8 0.20
5	0 0.00	1 0.25	2 0.50	1 0.25	0 0.00	0 0.00	2 0.50	0 0.00	1 0.25	0 0.00	7 0.18
4	0 0.00	0 0.00	0 0.00	1 0.25	0 0.00	0 0.00	1 0.25	0 0.00	2 0.50	2 0.50	6 0.15
3	0 0.00	0 0.00	0 0.00	1 0.25	0 0.00	0 0.00	0 0.00	0 0.00	1 0.25	2 0.50	4 0.10
2	1 0.25	2 0.50	0 0.00	0 0.00	0 0.00	0 0.00	0 0.00	0 0.00	3 0.75	1 0.25	7 0.18
1	0 0.00	0 0.00	1 0.25	0 0.00	0 0.00	0 0.00	0 0.00	2 0.50	0 0.00	0 0.00	3 0.08
sum	11 0.20		10 0.18		6 0.11		10 0.20		16 0.29		

Table 4.12: Contribution of the period incompatibility to the systematic error of $A^{\cos\phi_h}$ for each 3D bin (rounded to 3 decimals)

	P_T bin		1		2		3		4		5	
z bin		x bin	h^-	h^+	h^-	h^+	h^-	h^+	h^-	h^+	h^-	h^+
7	$\frac{\sigma_{A,\text{sp}}}{\sigma_{A,\text{stat}}}$	all	0.79	1.25	0.86	0.89	0.66	1.28	1.31	1.15	0.45	0.71
	$\sigma_{A,\text{sp}}$	1	0.019	0.028	0.018	0.016	0.019	0.030	0.028	0.020	0.015	0.018
		2	0.016	0.021	0.015	0.013	0.015	0.023	0.023	0.015	0.013	0.015
		3	0.019	0.024	0.017	0.013	0.017	0.024	0.025	0.015	0.014	0.015
		4	0.027	0.030	0.025	0.017	0.023	0.029	0.034	0.018	0.016	0.016
6	$\frac{\sigma_{A,\text{sp}}}{\sigma_{A,\text{stat}}}$	all	0.83	0.25	0.44	0.94	0.10	0.63	0.03	1.06	0.13	0.66
	$\sigma_{A,\text{sp}}$	1	0.013	0.004	0.006	0.011	0.002	0.009	0.000	0.012	0.003	0.012
		2	0.011	0.003	0.005	0.009	0.001	0.007	0.000	0.009	0.002	0.010
		3	0.012	0.003	0.005	0.009	0.001	0.007	0.000	0.009	0.002	0.010
		4	0.016	0.004	0.007	0.011	0.002	0.009	0.000	0.011	0.003	0.010
5	$\frac{\sigma_{A,\text{sp}}}{\sigma_{A,\text{stat}}}$	all	0.79	0.06	0.99	0.88	0.75	0.00	0.77	0.35	0.56	0.24
	$\sigma_{A,\text{sp}}$	1	0.007	0.001	0.008	0.006	0.008	0.000	0.007	0.003	0.009	0.003
		2	0.006	0.000	0.006	0.005	0.006	0.000	0.006	0.002	0.008	0.003
		3	0.006	0.000	0.007	0.005	0.007	0.000	0.006	0.002	0.008	0.003
		4	0.008	0.001	0.009	0.006	0.008	0.000	0.007	0.002	0.009	0.003
4	$\frac{\sigma_{A,\text{sp}}}{\sigma_{A,\text{stat}}}$	all	0.38	0.08	0.06	0.85	0.00	0.11	0.50	0.35	0.85	1.76
	$\sigma_{A,\text{sp}}$	1	0.003	0.001	0.000	0.006	0.000	0.001	0.005	0.003	0.015	0.028
		2	0.003	0.000	0.000	0.004	0.000	0.001	0.004	0.002	0.013	0.024
		3	0.003	0.000	0.000	0.005	0.000	0.001	0.004	0.002	0.014	0.024
		4	0.003	0.001	0.000	0.005	0.000	0.001	0.005	0.003	0.016	0.026
3	$\frac{\sigma_{A,\text{sp}}}{\sigma_{A,\text{stat}}}$	all	0.02	0.10	0.85	0.17	0.03	0.03	0.52	0.84	0.03	0.18
	$\sigma_{A,\text{sp}}$	1	0.000	0.001	0.005	0.001	0.000	0.000	0.004	0.007	0.000	0.003
		2	0.000	0.000	0.004	0.001	0.000	0.000	0.004	0.005	0.000	0.002
		3	0.000	0.000	0.004	0.001	0.000	0.000	0.004	0.005	0.000	0.002
		4	0.000	0.001	0.005	0.001	0.000	0.000	0.004	0.006	0.001	0.003
2	$\frac{\sigma_{A,\text{sp}}}{\sigma_{A,\text{stat}}}$	all	0.48	0.83	0.01	0.07	0.72	0.00	0.57	0.37	1.64	0.66
	$\sigma_{A,\text{sp}}$	1	0.003	0.005	0.000	0.000	0.006	0.000	0.005	0.003	0.028	0.010
		2	0.002	0.004	0.000	0.000	0.005	0.000	0.004	0.002	0.026	0.009
		3	0.002	0.004	0.000	0.000	0.005	0.000	0.004	0.002	0.028	0.010
		4	0.003	0.004	0.000	0.000	0.006	0.000	0.005	0.003	0.034	0.012
1	$\frac{\sigma_{A,\text{sp}}}{\sigma_{A,\text{stat}}}$	all	0.14	0.00	0.70	0.04	0.84	0.01	0.09	0.74	0.74	0.64
	$\sigma_{A,\text{sp}}$	1	0.000	0.000	0.002	0.000	0.004	0.000	0.000	0.003	0.008	0.006
		2	0.000	0.000	0.002	0.000	0.003	0.000	0.000	0.003	0.009	0.007
		3	0.000	0.000	0.002	0.000	0.003	0.000	0.000	0.003	0.010	0.007
		4	0.000	0.000	0.002	0.000	0.004	0.000	0.000	0.004	0.011	0.008

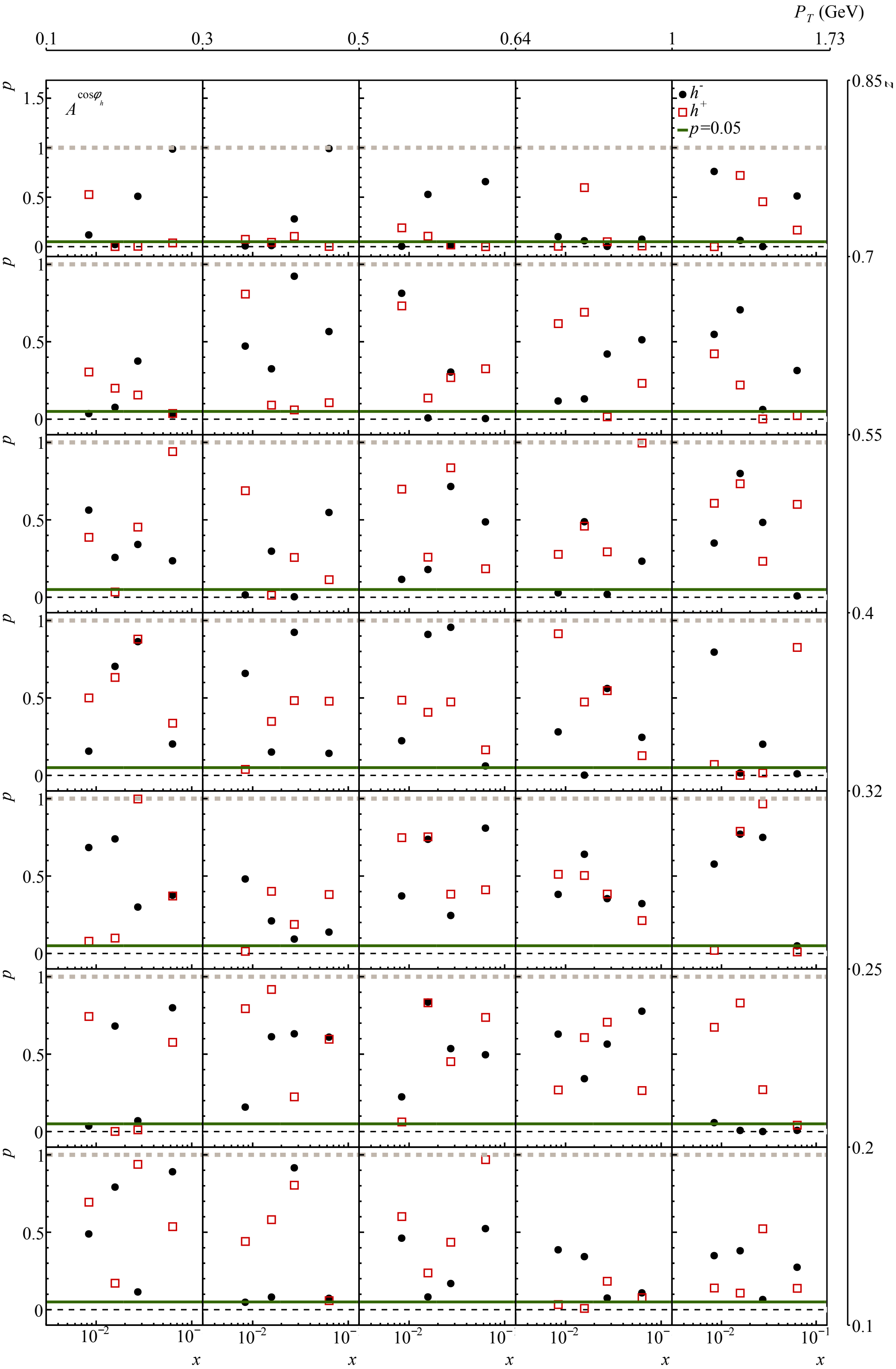

Figure 4.16: $A^{\cos\phi_h}$: p-value for positive and negative hadrons in 3D binning, green line corresponds to significance level $p = 0.05$

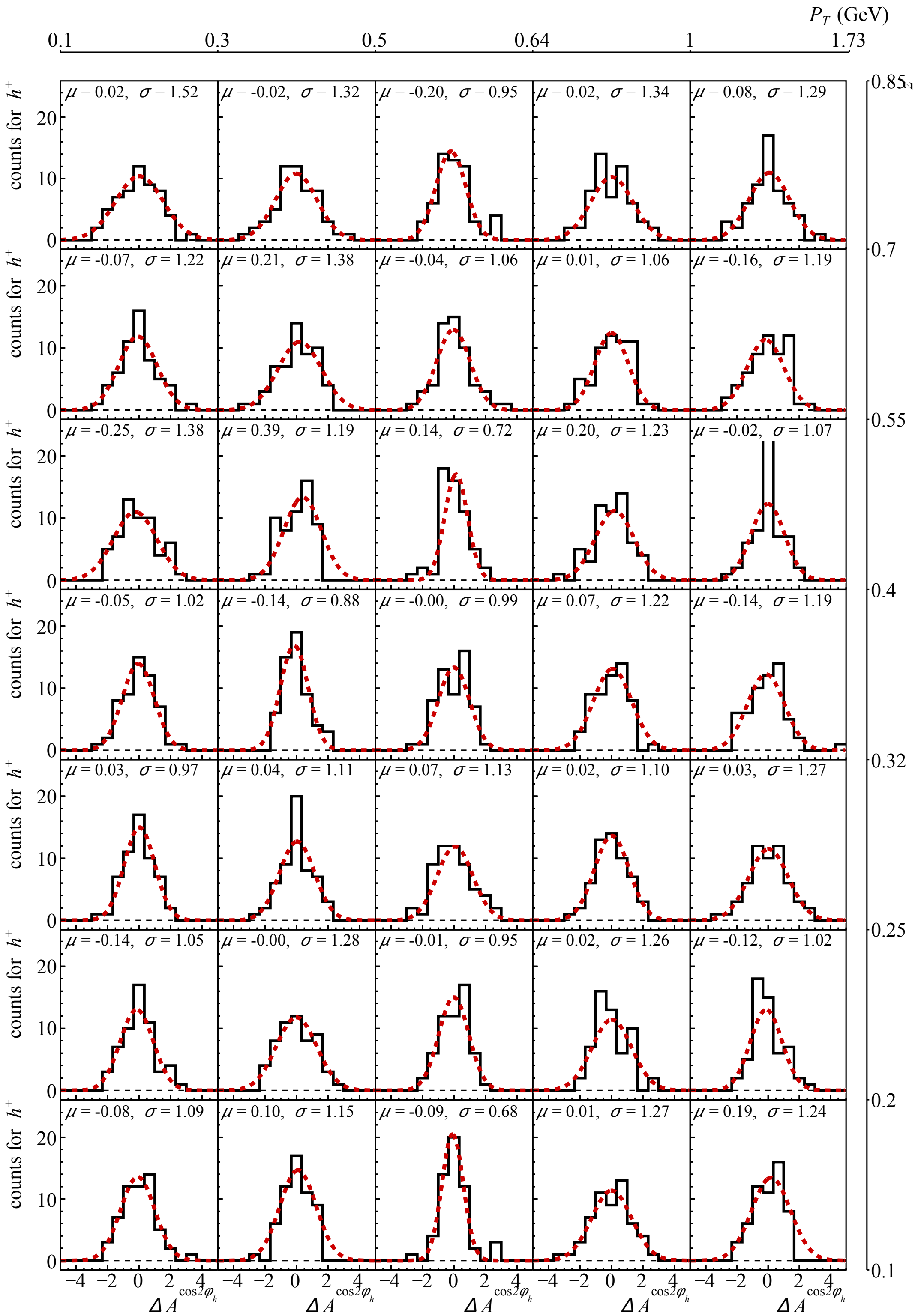

Figure 4.17: $A^{\cos 2\phi_h}$: pulls fitted with Gaussian (red-dashed) for positive hadrons in 3D binning

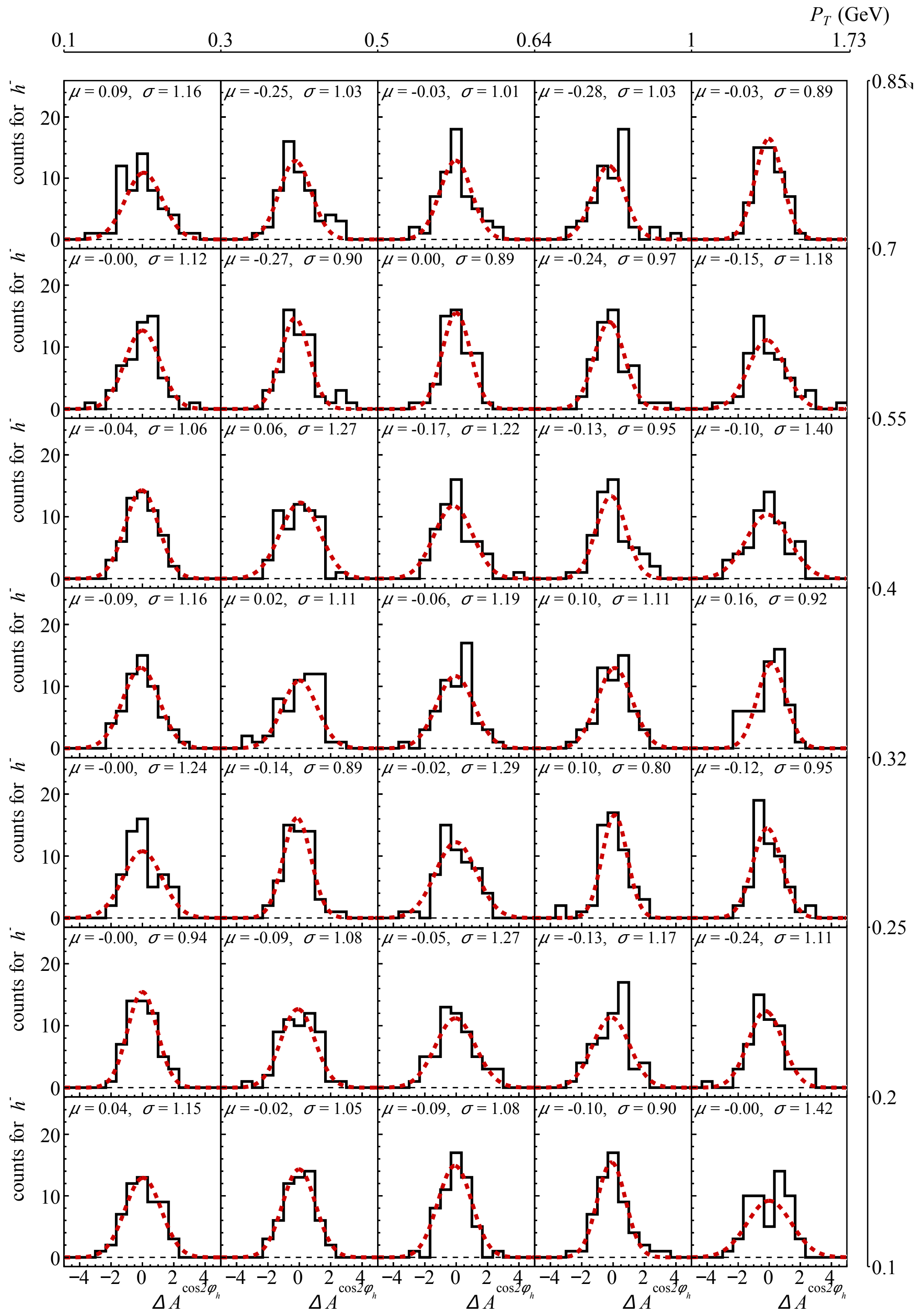

Figure 4.18: $A^{\cos 2\phi_h}$: pulls fitted with Gaussian (red-dashed) for negative hadrons in 3D binning

Table 4.13: $A^{\cos 2\phi_h}$: $p < 0.05$ statistics in 3D binning (numbers on the top of the row corresponds to the number of bins, numbers on the bottom are bins percentage)

z bin no./ P_T bin no.	1		2		3		4		5		sum
	h^-	h^+	h^-	h^+	h^-	h^+	h^-	h^+	h^-	h^+	
7	2	2	1	2	1	0	2	1	0	2	13
	0.50	0.50	0.25	0.50	0.25	0.00	0.50	0.25	0.00	0.50	0.33
6	0	2	2	1	0	0	0	0	2	1	8
	0.00	0.50	0.50	0.25	0.00	0.00	0.00	0.00	0.50	0.25	0.20
5	0	0	0	0	1	0	1	0	1	0	3
	0.00	0.00	0.00	0.00	0.25	0.00	0.25	0.00	0.25	0.00	0.08
4	2	0	2	0	1	0	0	0	0	1	6
	0.50	0.00	0.50	0.00	0.25	0.00	0.00	0.00	0.00	0.25	0.15
3	0	0	0	1	1	2	1	0	0	1	6
	0.00	0.00	0.00	0.25	0.25	0.50	0.25	0.00	0.00	0.25	0.15
2	0	0	1	1	1	0	1	0	2	0	6
	0.00	0.00	0.25	0.25	0.25	0.00	0.25	0.00	0.50	0.00	0.15
1	0	0	0	0	0	0	0	1	1	0	2
	0.00	0.00	0.00	0.00	0.00	0.00	0.00	0.25	0.25	0.00	0.05
sum	8		11		7		7		11		
	0.14		0.20		0.13		0.13		0.20		

Table 4.14: Contribution of the period incompatibility to the systematic error of $A^{\cos 2\phi_h}$ for each 3D bin (rounded to 3 decimals)

	P_T bin		1		2		3		4		5	
z bin		x bin	h^-	h^+	h^-	h^+	h^-	h^+	h^-	h^+	h^-	h^+
7	$\frac{\sigma_{A,\mathrm{sp}}}{\sigma_{A,\mathrm{stat}}}$	all	0.68	1.17	0.48	0.87	0.18	0.20	0.52	0.91	0.03	0.90
	$\sigma_{A,\mathrm{sp}}$	1	0.035	0.058	0.021	0.033	0.011	0.010	0.024	0.036	0.002	0.053
		2	0.028	0.039	0.017	0.025	0.008	0.007	0.020	0.026	0.002	0.042
		3	0.030	0.045	0.019	0.026	0.009	0.008	0.020	0.025	0.002	0.042
		4	0.046	0.057	0.028	0.033	0.012	0.009	0.026	0.030	0.002	0.043
6	$\frac{\sigma_{A,\mathrm{sp}}}{\sigma_{A,\mathrm{stat}}}$	all	0.49	0.78	0.27	1.15	0.00	0.39	0.24	0.36	0.78	0.80
	$\sigma_{A,\mathrm{sp}}$	1	0.016	0.023	0.008	0.028	0.000	0.013	0.007	0.009	0.038	0.033
		2	0.012	0.017	0.006	0.021	0.000	0.009	0.005	0.007	0.030	0.025
		3	0.014	0.018	0.006	0.022	0.000	0.009	0.006	0.007	0.031	0.024
		4	0.019	0.022	0.008	0.026	0.000	0.011	0.007	0.007	0.035	0.025
5	$\frac{\sigma_{A,\mathrm{sp}}}{\sigma_{A,\mathrm{stat}}}$	all	0.40	1.19	0.84	1.03	0.87	0.14	0.13	0.92	1.08	0.39
	$\sigma_{A,\mathrm{sp}}$	1	0.008	0.022	0.014	0.016	0.020	0.003	0.003	0.016	0.039	0.012
		2	0.006	0.016	0.011	0.012	0.015	0.002	0.002	0.012	0.029	0.009
		3	0.006	0.016	0.011	0.012	0.016	0.002	0.002	0.012	0.029	0.009
		4	0.008	0.019	0.015	0.014	0.019	0.002	0.002	0.013	0.034	0.010
4	$\frac{\sigma_{A,\mathrm{sp}}}{\sigma_{A,\mathrm{stat}}}$	all	0.67	0.23	0.52	0.14	0.71	0.00	0.59	0.76	0.16	0.78
	$\sigma_{A,\mathrm{sp}}$	1	0.012	0.004	0.008	0.002	0.015	0.000	0.012	0.014	0.006	0.027
		2	0.009	0.003	0.006	0.002	0.012	0.000	0.009	0.010	0.005	0.021
		3	0.010	0.003	0.007	0.002	0.012	0.000	0.009	0.010	0.005	0.021
		4	0.012	0.003	0.008	0.002	0.014	0.000	0.011	0.012	0.006	0.022
3	$\frac{\sigma_{A,\mathrm{sp}}}{\sigma_{A,\mathrm{stat}}}$	all	0.73	0.03	0.14	0.51	0.84	0.59	0.10	0.47	0.12	0.81
	$\sigma_{A,\mathrm{sp}}$	1	0.011	0.000	0.002	0.006	0.016	0.010	0.002	0.008	0.004	0.026
		2	0.008	0.000	0.001	0.005	0.012	0.008	0.001	0.006	0.004	0.021
		3	0.008	0.000	0.001	0.005	0.012	0.007	0.001	0.006	0.004	0.021
		4	0.010	0.000	0.002	0.005	0.014	0.009	0.002	0.007	0.004	0.023
2	$\frac{\sigma_{A,\mathrm{sp}}}{\sigma_{A,\mathrm{stat}}}$	all	0.00	0.47	0.50	0.80	0.83	0.01	0.74	0.78	0.72	0.32
	$\sigma_{A,\mathrm{sp}}$	1	0.000	0.006	0.006	0.009	0.015	0.000	0.014	0.014	0.027	0.011
		2	0.000	0.004	0.005	0.007	0.011	0.000	0.010	0.010	0.024	0.009
		3	0.000	0.004	0.005	0.007	0.011	0.000	0.011	0.010	0.025	0.010
		4	0.000	0.005	0.005	0.008	0.013	0.000	0.013	0.012	0.030	0.011
1	$\frac{\sigma_{A,\mathrm{sp}}}{\sigma_{A,\mathrm{stat}}}$	all	0.61	0.52	0.34	0.65	0.49	0.09	0.10	0.80	1.01	0.93
	$\sigma_{A,\mathrm{sp}}$	1	0.004	0.003	0.002	0.004	0.005	0.001	0.001	0.008	0.025	0.020
		2	0.003	0.002	0.002	0.003	0.004	0.001	0.001	0.007	0.025	0.020
		3	0.003	0.002	0.002	0.003	0.004	0.001	0.001	0.007	0.027	0.022
		4	0.003	0.003	0.002	0.003	0.005	0.001	0.001	0.008	0.030	0.024

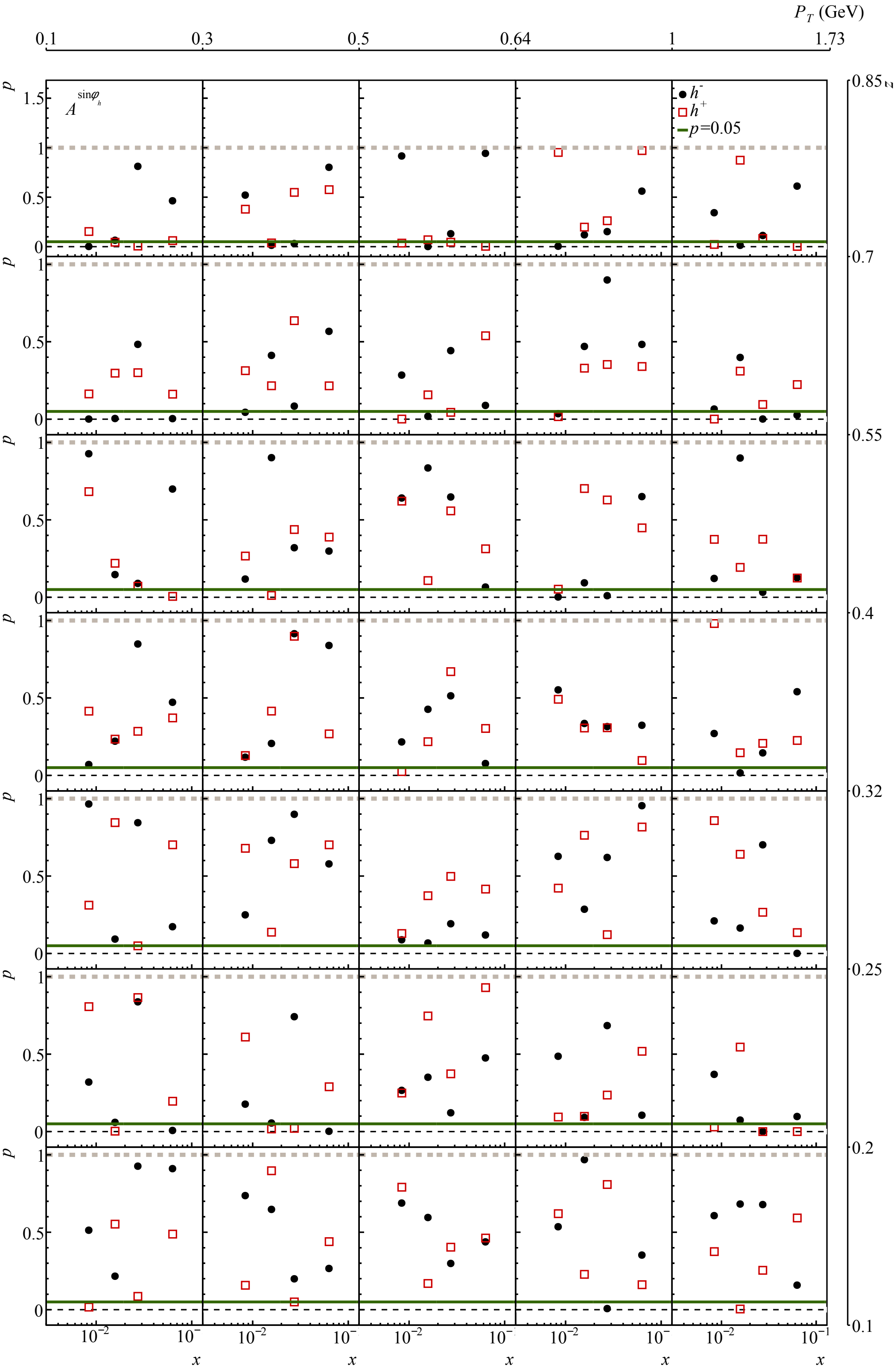

Figure 4.19: $A^{\sin\phi_h}$: p-value for positive and negative hadrons in 3D binning, green line corresponds to significance level $p = 0.05$

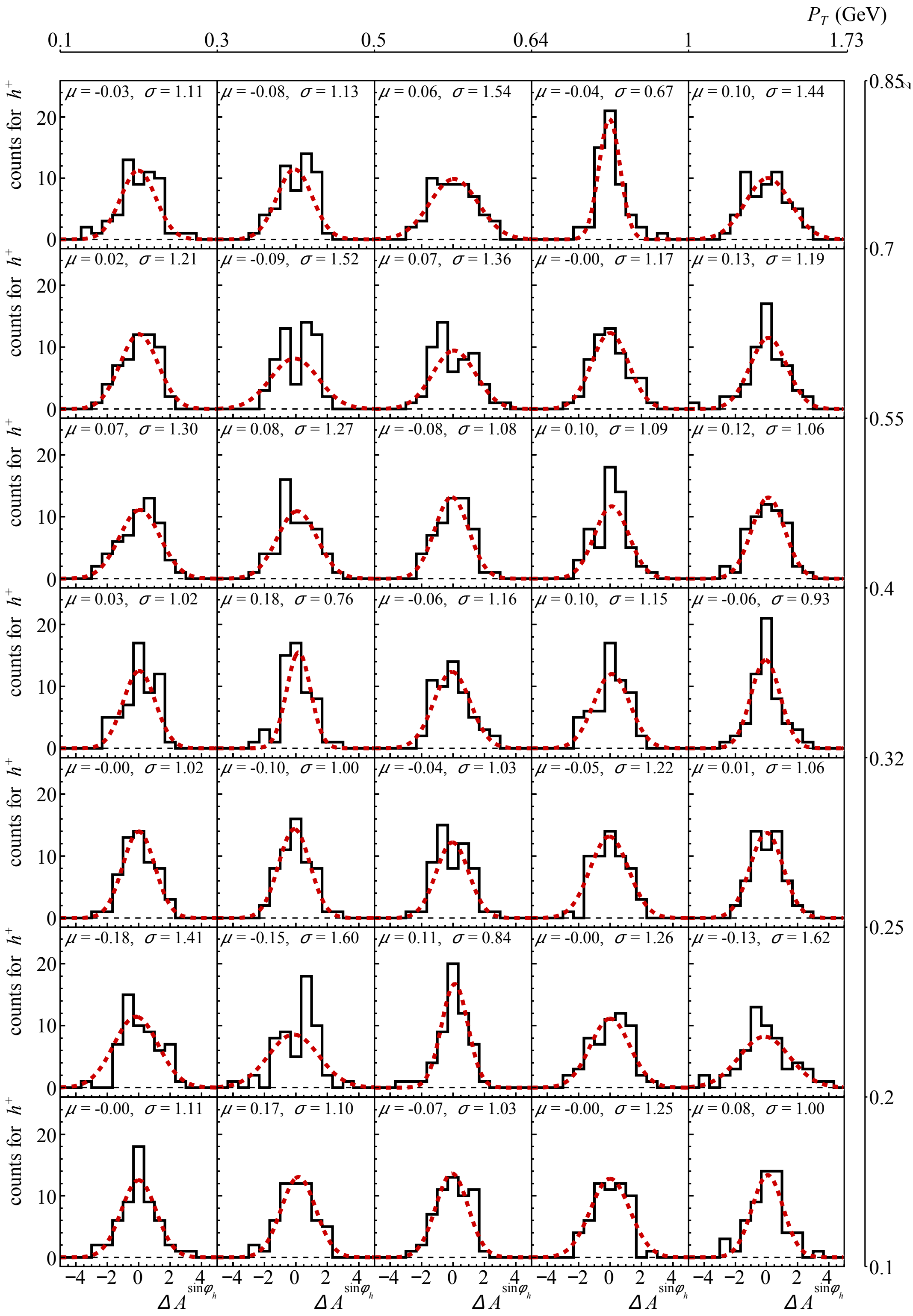

Figure 4.20: $A^{\sin\phi_h}$: pulls fitted with Gaussian (red-dashed) for positive hadrons in 3D binning

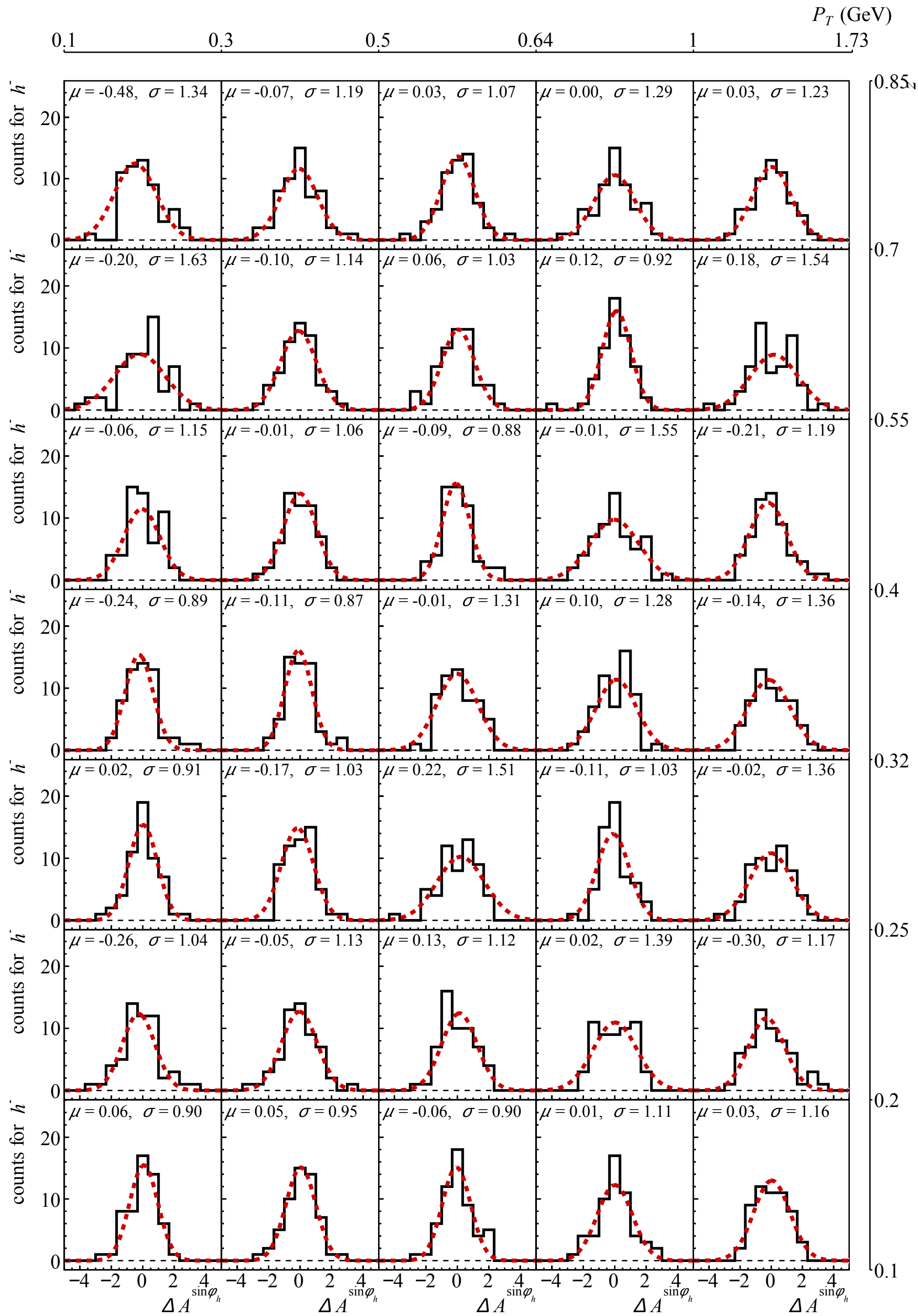

Figure 4.21: $A^{\sin\phi_h}$: pulls fitted with Gaussian (red-dashed) for negative hadrons in 3D binning

Table 4.15: $A^{\sin\phi_h}$: $p < 0.05$ statistics in 3D binning (numbers on the top of the row correspond to the number of bins, numbers on the bottom are bins percentage)

z bin no./ P_T bin no.	1		2		3		4		5		sum
	h^-	h^+	h^-	h^+	h^-	h^+	h^-	h^+	h^-	h^+	
7	1 0.25	2 0.50	2 0.50	1 0.25	1 0.25	3 0.75	1 0.25	0 0.00	1 0.25	2 0.50	14 0.35
6	3 0.75	0 0.00	1 0.25	0 0.00	1 0.25	2 0.50	1 0.25	1 0.25	2 0.50	1 0.25	12 0.30
5	0 0.00	1 0.25	0 0.00	1 0.25	0 0.00	0 0.00	2 0.50	0 0.00	1 0.25	0 0.00	5 0.13
4	0 0.00	0 0.00	0 0.00	0 0.00	0 0.00	1 0.25	0 0.00	0 0.00	1 0.25	0 0.00	2 0.05
3	0 0.00	1 0.25	0 0.00	0 0.00	0 0.00	0 0.00	0 0.00	0 0.00	1 0.25	0 0.00	2 0.05
2	1 0.25	1 0.25	1 0.25	2 0.50	0 0.00	0 0.00	0 0.00	0 0.00	1 0.25	3 0.75	9 0.23
1	0 0.00	1 0.25	0 0.00	0 0.00	0 0.00	0 0.00	1 0.25	0 0.00	0 0.00	1 0.25	3 0.08
sum	11 0.20		8 0.14		8 0.14		6 0.10		14 0.25		

Table 4.16: Contribution of the period incompatibility to the systematic error of $A^{\sin\phi_h}$ for each 3D bin (rounded to 3 decimals)

z bin	P_T bin	x bin	1 h^-	1 h^+	2 h^-	2 h^+	3 h^-	3 h^+	4 h^-	4 h^+	5 h^-	5 h^+
7	$\frac{\sigma_{A,\mathrm{sp}}}{\sigma_{A,\mathrm{stat}}}$	all	1.36	0.53	0.71	0.60	0.40	1.23	0.81	0.04	0.75	1.14
	$\sigma_{A,\mathrm{sp}}$	1	0.059	0.022	0.028	0.020	0.022	0.056	0.033	0.001	0.049	0.062
		2	0.095	0.031	0.041	0.030	0.032	0.079	0.049	0.002	0.070	0.087
		3	0.115	0.040	0.053	0.035	0.038	0.088	0.055	0.002	0.076	0.089
		4	0.176	0.047	0.078	0.043	0.049	0.107	0.071	0.002	0.083	0.086
6	$\frac{\sigma_{A,\mathrm{sp}}}{\sigma_{A,\mathrm{stat}}}$	all	1.49	0.70	0.65	1.23	0.32	0.99	0.12	0.61	1.35	0.77
	$\sigma_{A,\mathrm{sp}}$	1	0.042	0.018	0.016	0.027	0.010	0.029	0.003	0.014	0.056	0.028
		2	0.063	0.026	0.023	0.033	0.015	0.038	0.004	0.018	0.076	0.036
		3	0.080	0.030	0.028	0.044	0.017	0.044	0.005	0.020	0.084	0.037
		4	0.098	0.031	0.037	0.051	0.023	0.049	0.006	0.022	0.091	0.036
5	$\frac{\sigma_{A,\mathrm{sp}}}{\sigma_{A,\mathrm{stat}}}$	all	0.63	0.89	0.36	0.86	0.09	0.48	1.19	0.54	0.86	0.48
	$\sigma_{A,\mathrm{sp}}$	1	0.011	0.014	0.005	0.012	0.002	0.009	0.021	0.008	0.026	0.013
		2	0.016	0.020	0.008	0.016	0.002	0.012	0.027	0.011	0.033	0.016
		3	0.019	0.023	0.009	0.018	0.003	0.013	0.031	0.012	0.035	0.017
		4	0.024	0.026	0.011	0.021	0.003	0.015	0.036	0.013	0.040	0.018
4	$\frac{\sigma_{A,\mathrm{sp}}}{\sigma_{A,\mathrm{stat}}}$	all	0.24	0.23	0.11	0.18	0.85	0.65	0.91	0.66	1.07	0.06
	$\sigma_{A,\mathrm{sp}}$	1	0.003	0.003	0.002	0.002	0.017	0.012	0.016	0.011	0.035	0.002
		2	0.005	0.004	0.002	0.003	0.022	0.015	0.021	0.014	0.046	0.002
		3	0.006	0.005	0.002	0.004	0.025	0.017	0.024	0.015	0.052	0.002
		4	0.008	0.006	0.003	0.004	0.030	0.019	0.028	0.017	0.056	0.002
3	$\frac{\sigma_{A,\mathrm{sp}}}{\sigma_{A,\mathrm{stat}}}$	all	0.02	0.18	0.41	0.10	1.34	0.28	0.35	0.75	0.95	0.36
	$\sigma_{A,\mathrm{sp}}$	1	0.000	0.002	0.005	0.001	0.022	0.004	0.005	0.011	0.028	0.010
		2	0.000	0.003	0.006	0.001	0.029	0.006	0.007	0.014	0.038	0.013
		3	0.000	0.003	0.007	0.002	0.033	0.006	0.008	0.015	0.042	0.014
		4	0.001	0.004	0.009	0.002	0.038	0.007	0.009	0.017	0.047	0.015
2	$\frac{\sigma_{A,\mathrm{sp}}}{\sigma_{A,\mathrm{stat}}}$	all	0.54	1.17	0.57	1.39	0.62	0.11	0.98	0.76	0.91	1.41
	$\sigma_{A,\mathrm{sp}}$	1	0.005	0.013	0.005	0.014	0.010	0.002	0.015	0.009	0.028	0.040
		2	0.005	0.011	0.006	0.019	0.013	0.002	0.020	0.015	0.037	0.044
		3	0.010	0.019	0.009	0.015	0.015	0.002	0.021	0.016	0.046	0.063
		4	0.011	0.022	0.011	0.024	0.017	0.003	0.027	0.018	0.053	0.067
1	$\frac{\sigma_{A,\mathrm{sp}}}{\sigma_{A,\mathrm{stat}}}$	all	0.06	0.48	0.05	0.62	0.06	0.30	0.50	0.75	0.62	0.08
	$\sigma_{A,\mathrm{sp}}$	1	0.000	0.002	0.000	0.003	0.001	0.002	0.004	0.006	0.012	0.001
		2	0.000	0.003	0.000	0.004	0.001	0.003	0.006	0.009	0.020	0.002
		3	0.001	0.004	0.000	0.005	0.001	0.004	0.007	0.011	0.024	0.003
		4	0.001	0.004	0.000	0.005	0.001	0.004	0.008	0.012	0.026	0.003

4.8.2 Vertex dependance studies and compatability in vertex binning

The aim of vertex dependency studies of the azimuthal asymmetries is to verify that acceptance correction with *LEPTO* MC sample is done correctly. If any dependence on vertex position is observed, it must have its origin in spectrometers acceptance, because the azimuthal asymmetries should be independent of their vertex positions after acceptance correction.

The effect of the acceptance correction on the final asymmetries in vertex binning was studied in detail in x dependence with the use of 1D x bins (see 4.4) and the plotted graphs demonstrating this effect are shown in figures 4.22–4.24[4]. Whether the asymmetries are compatible is checked in section 4.8.2.

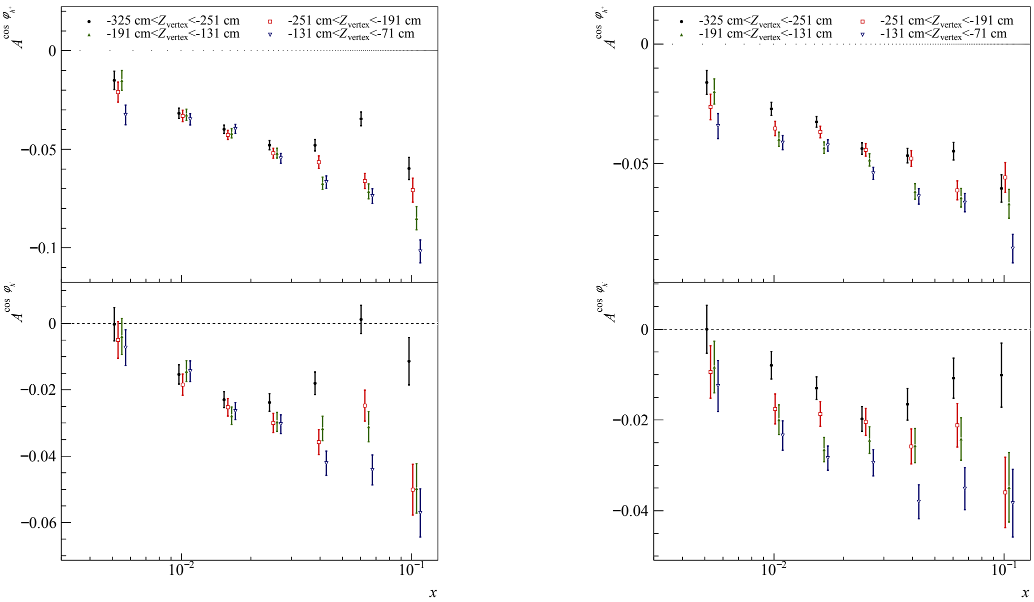

Figure 4.22: $A^{\cos\phi_h}$ for positive (top) and negative (bottom) hadrons in vertex binning before acceptance correction (left) and after acceptance correction (right)

[4]Displacement is set in graphs in the figures 4.24-4.22 to make the value of each point more distinguieshable

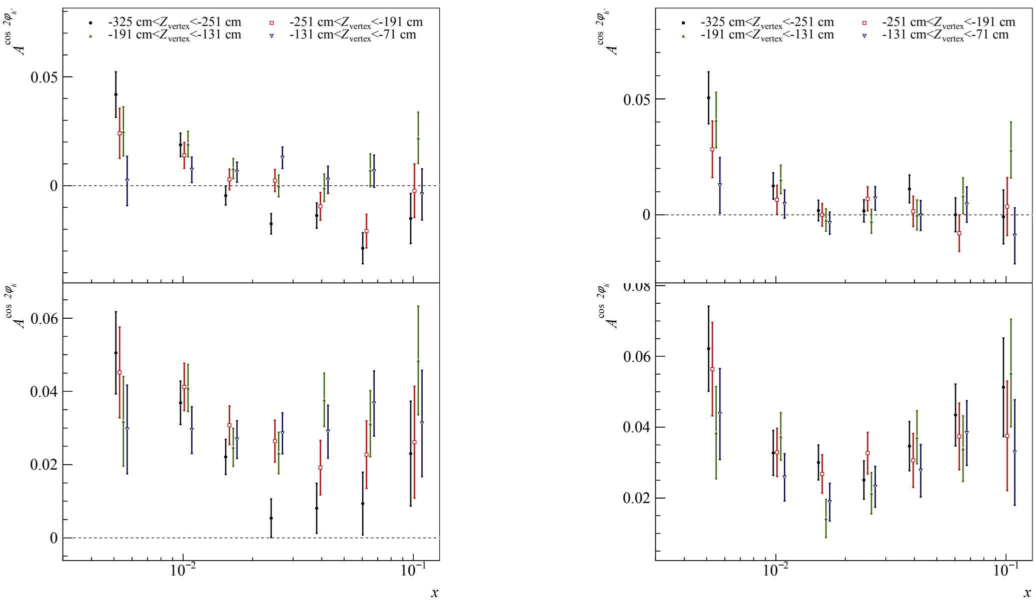

Figure 4.23: $A^{\cos 2\phi_h}$ for positive (top) and negative (bottom) in vertex binning before acceptance correction (left) and after acceptance correction (right)

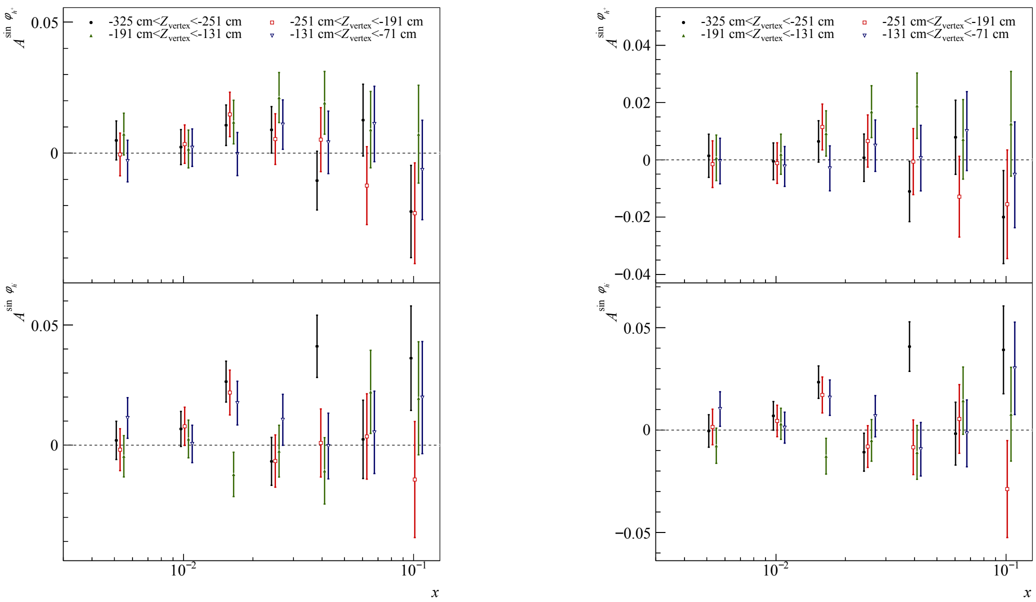

Figure 4.24: $A^{\sin \phi_h}$ for positive (top) and negative (bottom) in vertex binning before acceptance correction (left) and after acceptance correction (right)

The compatibility in the vertex binning was checked for results in each x bin before and after acceptance correction. The expected outcome was a higher p value (better compatibility) for results after the correction. Results of the compatibility check are shown in figures 4.25–4.26 and it is visible, that the expected outcome wasn't fulfilled for $\cos \phi_h$ modulation.

In the result graphs shown in previous figures 4.22–4.24 a deviation from the expected trivial vertex dependency, mainly for the most upstream target bin, is visible. Habitually, shortened target length (with the exclusion of targets the most upstream part in range -325 cm$<Z_{\text{vertex}}<-251$ cm) is used to obtain azimuthal asymmetries in both 1D and 3D binning. For this reason, we also performed the compatibility tests while excluding the most upstream part of the target, and the graph of p-values of each asymmetry after this process is shown in figure 4.27. We evaluate the compatibility according to the number of bins with $p<0.05$ in table 4.17.

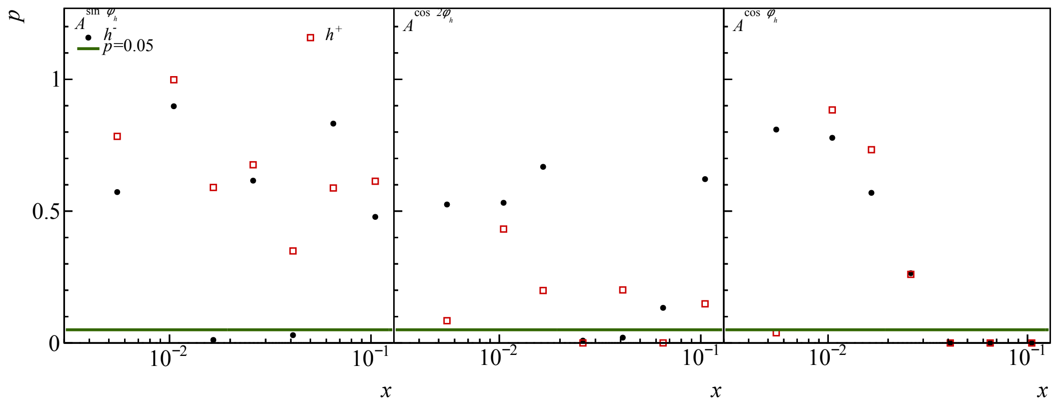

Figure 4.25: p-value for $A^{\sin\phi_h}$ (left) $A^{\cos 2\phi_h}$ (middle) and $A^{\cos\phi_h}$ (right) of positive and negative hadrons in vertex binning before acceptance correction

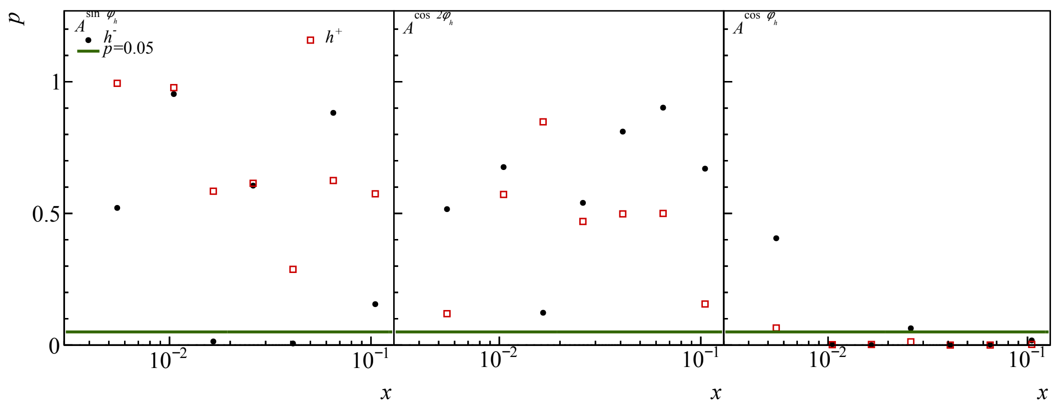

Figure 4.26: p-value for $A^{\sin\phi_h}$ (left) $A^{\cos 2\phi_h}$ (middle) and $A^{\cos\phi_h}$ (right) of positive and negative hadrons in vertex binning after acceptance correction

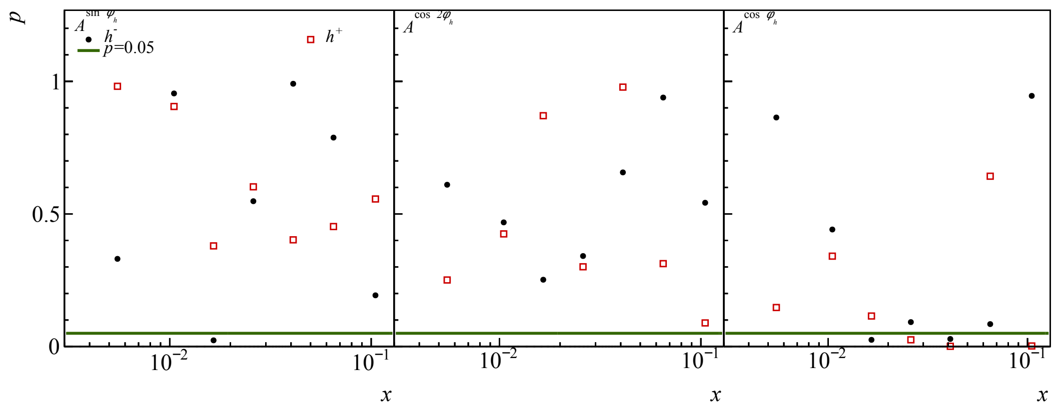

Figure 4.27: p-value for $A^{\sin\phi_h}$ (left) $A^{\cos 2\phi_h}$ (middle) and $A^{\cos\phi_h}$ (right) of positive and negative hadrons in vertex binning after acceptance correction and 1st vertex bin exclusion

Table 4.17: $p < 0.05$ statistics in vertex 3D binning

asymmetry	$A^{\sin\phi_h}$		$A^{\cos 2\phi_h}$		$A^{\cos\phi_h}$	
data sample conditions	number of bins with $p < 0.05$					
	h^-	h^+	h^-	h^+	h^-	h^+
before acceptance correction	2	0	2	2	3	4
after acceptance correction	2	0	0	0	5	6
1st vertex bin exclusion	1	0	0	0	2	3

From the results of the compatibility check in vertex binning was concluded, that acceptance correction provided through the *LEPTO* MC samples shows a significant systematic effect, which needs to be accounted for in systematic error. Further investigating the vertex dependence brought us to the conclusion, that we expect a growing tendency for the value of the contribution in its dependence on x and simultaneously no rapid changes in adjacent x bins. To meet these expectations and reduce the statistical influence on the error contribution, the final estimation of the systematic contribution was calculated as the average of the given bin and its nearest bin neighbour's errors, specifically with the following formula:

$$\sigma_{A_i,\mathrm{sv}} = \frac{1}{K}\sum_k \max_{j\in V}\left(|A_i - A_{j,k}|\right) \ , \tag{4.12}$$

where the sum runs over the adjacent bins, K represents their number, set V contains all vertex bins in the shortened target length, which were used in the 1D and 3D analysis (i.e. bins 1–3, see section 4.4), index i runs over x bins, A_i is the final asymmetry in i-th x bin and $A_{j,i}$ is the same x bin asymmetry in j-th vertex bin.

Vertex position dependence of the asymmetries in z and P_T was not studied in this thesis. In this case, the contribution of the vertex incompatibility to the systematic error was estimated as the average $\sigma_{A_i,\mathrm{sv}}$ over x bins. To demonstrate the relative size of the systematic error, the table 4.18 evaluates systematic uncertainty in x binning using equation 4.12 as well as the average error value $\sigma_{A_i,\mathrm{sv}}$

used for error estimation in z and P_T (bold numbers), and tables 4.9–4.10 show the relative size of the vertex contribution to the systematic error in z and P_T bins towards their statistical error.

Table 4.18: Contribution of the vertex incompatibility to the systematic error for each 1D x bin (number on the top of the row is $\frac{\sigma_{A,\mathrm{sv}}}{\sigma_{A,\mathrm{stat}}}$ rounded to 2 decimals, number on the bottom is $\sigma_{A_i,\mathrm{sv}}$ rounded to 3 decimals)

x bin no.	1		2		3		4	
A	h^-	h^+	h^-	h^+	h^-	h^+	h^-	h^+
$A^{\cos\phi_h}$	0.73	2.38	1.58	1.81	3.81	2.97	2.73	3.45
	0.002	0.007	0.003	0.003	0.006	0.004	0.005	0.005
$A^{\cos 2\phi_h}$	1.49	2.11	1.54	1.84	2.25	0.83	2.19	2.14
	0.011	0.015	0.006	0.007	0.007	0.002	0.007	0.006
$A^{\sin\phi_h}$	1.83	0.31	0.54	0.59	3.84	1.88	1.41	1.48
	0.009	0.001	0.002	0.002	0.019	0.009	0.008	0.008
x bin no.	5		6		7		average	
A	h^-	h^+	h^-	h^+	h^-	h^+	h^-	h^+
$A^{\cos\phi_h}$	3.81	5.24	3.11	1.22	0.65	4.94	2.34	3.17
	0.008	0.010	0.008	0.003	0.003	0.017	**0.005**	**0.007**
$A^{\cos 2\phi_h}$	1.31	0.29	0.51	2.11	1.57	2.86	1.56	1.79
	0.006	0.001	0.003	0.009	0.014	0.020	**0.008**	**0.009**
$A^{\sin\phi_h}$	0.27	2.15	0.97	1.85	2.29	1.42	1.56	1.40
	0.002	0.014	0.009	0.015	0.030	0.015	**0.011**	**0.009**

Table 4.19: Contribution of the vertex incompatibility to the systematic error for each 1D z bin (rounded to 2 significant digits)

x bin no.	1		2		3		4		5	
A	$\frac{\sigma_{A,\mathrm{sv}}}{\sigma_{A,\mathrm{stat}}}$		$\frac{\sigma_{A,\mathrm{sv}}}{\sigma_{A,\mathrm{stat}}}$		$\frac{\sigma_{A,\mathrm{sv}}}{\sigma_{A,\mathrm{stat}}}$		$\frac{\sigma_{A,\mathrm{sv}}}{\sigma_{A,\mathrm{stat}}}$		$\frac{\sigma_{A,\mathrm{sv}}}{\sigma_{A,\mathrm{stat}}}$	
	h^-	h^+	h^-	h^+	h^-	h^+	h^-	h^+	h^-	h^+
$A^{\cos\phi_h}$	6.64	9.88	3.43	5.19	2.84	4.39	2.16	3.40	1.92	3.05
$A^{\cos 2\phi_h}$	4.93	5.99	2.56	3.14	2.12	2.66	1.62	2.07	1.43	1.84
$A^{\sin\phi_h}$	5.54	4.64	2.84	2.40	2.34	2.01	1.78	1.55	1.54	1.36
x bin no.	6		7		8		9			
A	$\frac{\sigma_{A,\mathrm{sv}}}{\sigma_{A,\mathrm{stat}}}$		$\frac{\sigma_{A,\mathrm{sv}}}{\sigma_{A,\mathrm{stat}}}$		$\frac{\sigma_{A,\mathrm{sv}}}{\sigma_{A,\mathrm{stat}}}$		$\frac{\sigma_{A,\mathrm{sv}}}{\sigma_{A,\mathrm{stat}}}$			
	h^-	h^+	h^-	h^+	h^-	h^+	h^-	h^+		
$A^{\cos\phi_h}$	1.67	2.69	1.82	3.01	1.90	3.21	1.42	2.53		
$A^{\cos 2\phi_h}$	1.24	1.63	1.38	1.82	1.42	1.94	1.05	1.50		
$A^{\sin\phi_h}$	1.35	1.21	1.50	1.35	1.55	1.42	1.42	1.08		

Table 4.20: Contribution of the vertex incompatibility to the systematic error for each 1D P_T bin (rounded to 2 significant digits)

x bin no.	1		2		3		4		5	
A	$\frac{\sigma_{A,\mathrm{sv}}}{\sigma_{A,\mathrm{stat}}}$		$\frac{\sigma_{A,\mathrm{sv}}}{\sigma_{A,\mathrm{stat}}}$		$\frac{\sigma_{A,\mathrm{sv}}}{\sigma_{A,\mathrm{stat}}}$		$\frac{\sigma_{A,\mathrm{sv}}}{\sigma_{A,\mathrm{stat}}}$		$\frac{\sigma_{A,\mathrm{sv}}}{\sigma_{A,\mathrm{stat}}}$	
	h^-	h^+	h^-	h^+	h^-	h^+	h^-	h^+	h^-	h^+
$A^{\cos\phi_h}$	2.08	3.23	2.04	3.20	1.99	3.12	2.01	3.16	2.11	3.33
$A^{\cos 2\phi_h}$	1.54	1.96	1.52	1.94	1.49	1.89	1.51	1.91	1.58	2.01
$A^{\sin\phi_h}$	1.67	1.45	1.64	1.43	1.60	1.39	1.63	1.40	1.71	1.49
x bin no.	6		7		8		9			
A	$\frac{\sigma_{A,\mathrm{sv}}}{\sigma_{A,\mathrm{stat}}}$		$\frac{\sigma_{A,\mathrm{sv}}}{\sigma_{A,\mathrm{stat}}}$		$\frac{\sigma_{A,\mathrm{sv}}}{\sigma_{A,\mathrm{stat}}}$		$\frac{\sigma_{A,\mathrm{sv}}}{\sigma_{A,\mathrm{stat}}}$		$\frac{\sigma_{A,\mathrm{sv}}}{\sigma_{A,\mathrm{stat}}}$	
	h^-	h^+	h^-	h^+	h^-	h^+	h^-	h^+	h^-	h^+
$A^{\cos\phi_h}$	2.24	3.54	2.00	3.19	2.01	3.22	1.90	3.08	1.47	2.45
$A^{\cos 2\phi_h}$	1.68	2.14	1.50	1.92	1.50	1.94	1.42	1.86	1.09	1.48
$A^{\sin\phi_h}$	1.82	1.59	1.64	1.44	1.68	1.47	1.63	1.45	1.37	1.21

Evaluation of the contribution to the systematic error requires knowing the vertex asymmetries $A_{j,i}$ in x dependence with the use of both 1D and 3D x bins. Missing information about 3D x bins and another demonstration of the mentioned systematic effect is provided in the following figures 4.28 and 4.29. The contribution of the vertex incompatability to the systematic error is evaluated in tables 4.21–4.23.

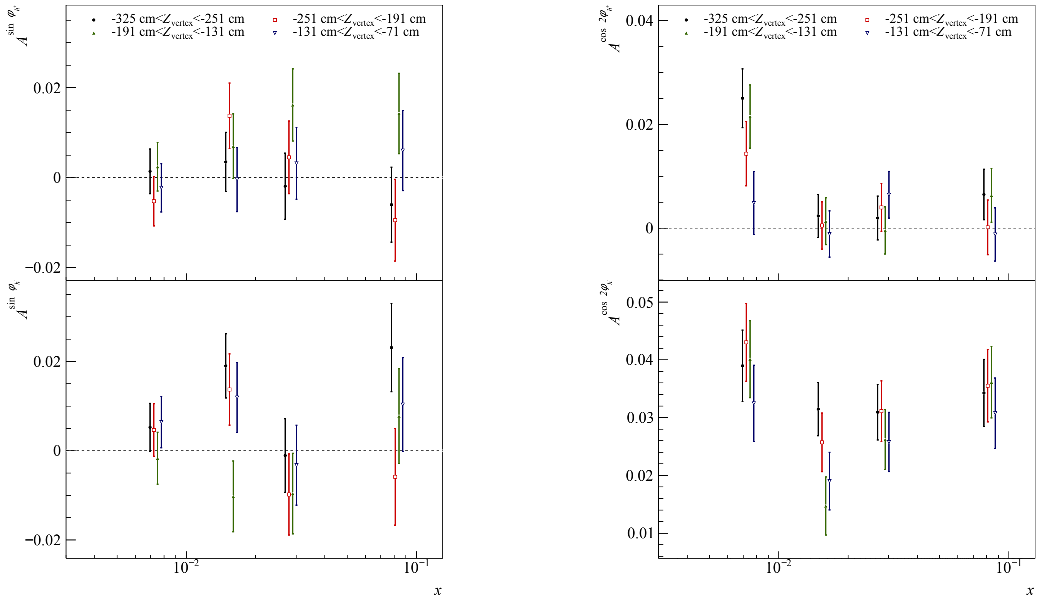

Figure 4.28: Azimuthal asymmetries $A^{\sin\phi_h}$(left) and $A^{\cos 2\phi_h}$(right) for positive (top) and negative (bottom) hadrons evaluated in 3D x bins

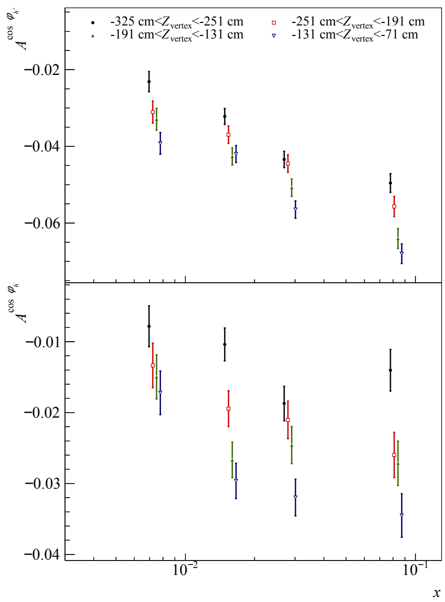

Figure 4.29: $A^{\cos\phi_h}$for positive (top) and negative (bottom) hadrons evaluated in 3D x bins

Table 4.21: Contribution of the vertex incompatibility to the systematic error of $A^{\cos\phi_h}$ for each 3D bin (number on the top of the row is $\frac{\sigma_{A,\mathrm{sv}}}{\sigma_{A,\mathrm{stat}}}$ rounded to 2 decimals, number on the bottom is $\sigma_{A,\mathrm{sv}}$ rounded to 3 decimals)

P_T bin		1		2		3		4		5	
z bin no.	x bin no.	h^-	h^+	h^-	h^+	h^-	h^+	h^-	h^+	h^-	h^+
7	1	0.16	0.18	0.19	0.24	0.14	0.18	0.18	0.24	0.12	0.16
		0.004	0.004	0.004	0.004	0.004	0.004	0.004	0.004	0.004	0.004
	2	0.23	0.29	0.27	0.34	0.20	0.27	0.26	0.37	0.16	0.23
		0.005	0.005	0.005	0.005	0.005	0.005	0.005	0.005	0.005	0.005
	3	0.24	0.29	0.28	0.38	0.22	0.30	0.30	0.42	0.19	0.27
		0.006	0.006	0.006	0.006	0.006	0.006	0.006	0.006	0.006	0.006
	4	0.17	0.27	0.19	0.35	0.16	0.30	0.22	0.42	0.16	0.29
		0.006	0.007	0.006	0.007	0.006	0.007	0.006	0.007	0.006	0.007
6	1	0.25	0.30	0.30	0.36	0.23	0.28	0.29	0.37	0.17	0.23
		0.004	0.004	0.004	0.004	0.004	0.004	0.004	0.004	0.004	0.004
	2	0.37	0.45	0.43	0.53	0.33	0.42	0.41	0.55	0.24	0.33
		0.005	0.005	0.005	0.005	0.005	0.005	0.005	0.005	0.005	0.005
	3	0.40	0.47	0.48	0.59	0.37	0.48	0.48	0.63	0.29	0.39
		0.006	0.006	0.006	0.006	0.006	0.006	0.006	0.006	0.006	0.006
	4	0.29	0.47	0.36	0.58	0.28	0.48	0.38	0.65	0.24	0.44
		0.006	0.007	0.006	0.007	0.006	0.007	0.006	0.007	0.006	0.007
5	1	0.42	0.49	0.48	0.58	0.37	0.45	0.43	0.52	0.24	0.29
		0.004	0.004	0.004	0.004	0.004	0.004	0.004	0.004	0.004	0.004
	2	0.61	0.73	0.71	0.86	0.54	0.66	0.62	0.77	0.34	0.42
		0.005	0.005	0.005	0.005	0.005	0.005	0.005	0.005	0.005	0.005
	3	0.70	0.81	0.83	0.96	0.63	0.75	0.73	0.89	0.41	0.50
		0.006	0.006	0.006	0.006	0.006	0.006	0.006	0.006	0.006	0.006
	4	0.54	0.82	0.64	0.97	0.51	0.76	0.60	0.93	0.35	0.55
		0.006	0.007	0.006	0.007	0.006	0.007	0.006	0.007	0.006	0.007
4	1	0.46	0.54	0.53	0.62	0.39	0.45	0.42	0.49	0.22	0.26
		0.004	0.004	0.004	0.004	0.004	0.004	0.004	0.004	0.004	0.004
	2	0.68	0.79	0.77	0.92	0.56	0.66	0.60	0.72	0.30	0.36
		0.005	0.005	0.005	0.005	0.005	0.005	0.005	0.005	0.005	0.005
	3	0.79	0.90	0.90	1.03	0.67	0.77	0.72	0.82	0.35	0.42
		0.006	0.006	0.006	0.006	0.006	0.006	0.006	0.006	0.006	0.006
	4	0.63	0.91	0.74	1.06	0.54	0.79	0.61	0.86	0.31	0.45
		0.006	0.007	0.006	0.007	0.006	0.007	0.006	0.007	0.006	0.007
3	1	0.58	0.67	0.65	0.74	0.45	0.52	0.47	0.54	0.24	0.28
		0.004	0.004	0.004	0.004	0.004	0.004	0.004	0.004	0.004	0.004
	2	0.87	1.00	0.95	1.10	0.66	0.77	0.68	0.78	0.32	0.37
		0.005	0.005	0.005	0.005	0.005	0.005	0.005	0.005	0.005	0.005
	3	1.03	1.14	1.13	1.25	0.80	0.88	0.81	0.89	0.37	0.42
		0.006	0.006	0.006	0.006	0.006	0.006	0.006	0.006	0.006	0.006
	4	0.84	1.16	0.93	1.28	0.67	0.91	0.69	0.94	0.32	0.44
		0.006	0.007	0.006	0.007	0.006	0.007	0.006	0.007	0.006	0.007
2	1	0.64	0.73	0.69	0.78	0.46	0.52	0.46	0.52	0.23	0.27
		0.004	0.004	0.004	0.004	0.004	0.004	0.004	0.004	0.004	0.004
	2	0.96	1.08	1.02	1.16	0.69	0.77	0.66	0.76	0.29	0.34
		0.005	0.005	0.005	0.005	0.005	0.005	0.005	0.005	0.005	0.005
	3	1.14	1.23	1.21	1.31	0.83	0.88	0.79	0.84	0.33	0.37
		0.006	0.006	0.006	0.006	0.006	0.006	0.006	0.006	0.006	0.006
	4	0.95	1.27	1.03	1.35	0.69	0.91	0.66	0.88	0.27	0.38
		0.006	0.007	0.006	0.007	0.006	0.007	0.006	0.007	0.006	0.007
1	1	1.39	1.54	1.36	1.51	0.85	0.95	0.80	0.91	0.36	0.42
		0.004	0.004	0.004	0.004	0.004	0.004	0.004	0.004	0.004	0.004
	2	2.07	2.29	1.98	2.21	1.21	1.34	1.06	1.19	0.38	0.45
		0.005	0.005	0.005	0.005	0.005	0.005	0.005	0.005	0.005	0.005
	3	2.49	2.61	2.38	2.50	1.42	1.50	1.22	1.32	0.42	0.48
		0.006	0.006	0.006	0.006	0.006	0.006	0.006	0.006	0.006	0.006
	4	2.09	2.65	2.04	2.60	1.20	1.53	1.03	1.33	0.37	0.51
		0.006	0.007	0.006	0.007	0.006	0.007	0.006	0.007	0.006	0.007

Table 4.22: Contribution of the vertex incompatibility to the systematic error of $A^{\cos 2\phi_h}$ for each 3D bin (number on the top of the row is $\frac{\sigma_{A,\mathrm{sv}}}{\sigma_{A,\mathrm{stat}}}$ rounded to 2 decimals, number on the bottom is $\sigma_{A,\mathrm{sv}}$ rounded to 3 decimals)

P_T bin		1		2		3		4		5	
z bin no.	x bin no.	h^-	h^+	h^-	h^+	h^-	h^+	h^-	h^+	h^-	h^+
7	1	0.12 0.006	0.10 0.005	0.14 0.006	0.13 0.005	0.10 0.006	0.10 0.005	0.13 0.006	0.13 0.005	0.08 0.006	0.09 0.005
	2	0.13 0.005	0.14 0.005	0.15 0.005	0.16 0.005	0.11 0.005	0.12 0.005	0.13 0.005	0.16 0.005	0.08 0.005	0.10 0.005
	3	0.10 0.004	0.08 0.003	0.10 0.004	0.11 0.003	0.08 0.004	0.08 0.003	0.11 0.004	0.12 0.003	0.07 0.004	0.07 0.003
	4	0.05 0.003	0.09 0.004	0.06 0.003	0.11 0.004	0.05 0.003	0.09 0.004	0.07 0.003	0.13 0.004	0.05 0.003	0.09 0.004
6	1	0.19 0.006	0.17 0.005	0.22 0.006	0.20 0.005	0.16 0.006	0.15 0.005	0.21 0.006	0.20 0.005	0.12 0.006	0.12 0.005
	2	0.20 0.005	0.21 0.005	0.24 0.005	0.25 0.005	0.18 0.005	0.20 0.005	0.22 0.005	0.25 0.005	0.13 0.005	0.15 0.005
	3	0.15 0.004	0.14 0.003	0.18 0.004	0.17 0.003	0.14 0.004	0.14 0.003	0.18 0.004	0.18 0.003	0.11 0.004	0.11 0.003
	4	0.09 0.003	0.15 0.004	0.11 0.003	0.19 0.004	0.08 0.003	0.15 0.004	0.12 0.003	0.20 0.004	0.08 0.003	0.14 0.004
5	1	0.30 0.006	0.28 0.005	0.35 0.006	0.32 0.005	0.26 0.006	0.25 0.005	0.30 0.006	0.29 0.005	0.17 0.006	0.16 0.005
	2	0.33 0.005	0.35 0.005	0.39 0.005	0.40 0.005	0.30 0.005	0.31 0.005	0.35 0.005	0.36 0.005	0.19 0.005	0.20 0.005
	3	0.26 0.004	0.24 0.003	0.31 0.004	0.28 0.003	0.24 0.004	0.21 0.003	0.28 0.004	0.26 0.003	0.16 0.004	0.14 0.003
	4	0.17 0.003	0.26 0.004	0.20 0.003	0.31 0.004	0.16 0.003	0.24 0.004	0.19 0.003	0.29 0.004	0.11 0.003	0.17 0.004
4	1	0.32 0.006	0.30 0.005	0.38 0.006	0.35 0.005	0.27 0.006	0.25 0.005	0.29 0.006	0.27 0.005	0.15 0.006	0.15 0.005
	2	0.37 0.005	0.38 0.005	0.43 0.005	0.43 0.005	0.31 0.005	0.31 0.005	0.33 0.005	0.34 0.005	0.16 0.005	0.17 0.005
	3	0.29 0.004	0.26 0.003	0.34 0.004	0.30 0.003	0.25 0.004	0.22 0.003	0.27 0.004	0.24 0.003	0.13 0.004	0.12 0.003
	4	0.19 0.003	0.29 0.004	0.23 0.003	0.33 0.004	0.17 0.003	0.25 0.004	0.19 0.003	0.28 0.004	0.09 0.003	0.15 0.004
3	1	0.41 0.006	0.38 0.005	0.45 0.006	0.41 0.005	0.32 0.006	0.29 0.005	0.33 0.006	0.30 0.005	0.17 0.006	0.16 0.005
	2	0.48 0.005	0.47 0.005	0.53 0.005	0.52 0.005	0.37 0.005	0.36 0.005	0.38 0.005	0.37 0.005	0.18 0.005	0.18 0.005
	3	0.38 0.004	0.33 0.003	0.42 0.004	0.36 0.003	0.30 0.004	0.26 0.003	0.31 0.004	0.26 0.003	0.14 0.004	0.12 0.003
	4	0.25 0.003	0.37 0.004	0.28 0.003	0.41 0.004	0.20 0.003	0.29 0.004	0.21 0.003	0.30 0.004	0.10 0.003	0.14 0.004
2	1	0.46 0.006	0.41 0.005	0.48 0.006	0.43 0.005	0.33 0.006	0.29 0.005	0.33 0.006	0.29 0.005	0.16 0.006	0.15 0.005
	2	0.53 0.005	0.51 0.005	0.57 0.005	0.55 0.005	0.38 0.005	0.36 0.005	0.37 0.005	0.36 0.005	0.15 0.005	0.16 0.005
	3	0.43 0.004	0.36 0.003	0.45 0.004	0.38 0.003	0.31 0.004	0.25 0.003	0.30 0.004	0.25 0.003	0.12 0.004	0.11 0.003
	4	0.29 0.003	0.40 0.004	0.31 0.003	0.43 0.004	0.21 0.003	0.29 0.004	0.20 0.003	0.28 0.004	0.08 0.003	0.12 0.004
1	1	0.98 0.006	0.86 0.005	0.96 0.006	0.84 0.005	0.59 0.006	0.53 0.005	0.56 0.006	0.51 0.005	0.25 0.006	0.24 0.005
	2	1.14 0.005	1.08 0.005	1.08 0.005	1.04 0.005	0.66 0.005	0.63 0.005	0.57 0.005	0.56 0.005	0.20 0.005	0.21 0.005
	3	0.92 0.004	0.75 0.003	0.88 0.004	0.72 0.003	0.52 0.004	0.43 0.003	0.45 0.004	0.37 0.003	0.16 0.004	0.14 0.003
	4	0.63 0.003	0.85 0.004	0.61 0.003	0.82 0.004	0.36 0.003	0.48 0.004	0.31 0.003	0.42 0.004	0.11 0.003	0.16 0.004

Table 4.23: Contribution of the vertex incompatibility to the systematic error of $A^{\sin\phi_h}$ for each 3D bin (number on the top of the row is $\frac{\sigma_{A,\mathrm{sv}}}{\sigma_{A,\mathrm{stat}}}$ rounded to 2 decimals, number on the bottom is $\sigma_{A,\mathrm{sv}}$ rounded to 3 decimals)

P_T bin		1		2		3		4		5	
z bin no.	x bin no.	h^-	h^+	h^-	h^+	h^-	h^+	h^-	h^+	h^-	h^+
7	1	0.23	0.13	0.26	0.16	0.19	0.12	0.25	0.16	0.15	0.10
		0.010	0.006	0.010	0.006	0.010	0.006	0.010	0.006	0.010	0.006
	2	0.12	0.11	0.14	0.13	0.10	0.10	0.13	0.14	0.09	0.08
		0.008	0.006	0.008	0.006	0.008	0.006	0.008	0.006	0.008	0.006
	3	0.12	0.13	0.13	0.16	0.10	0.13	0.15	0.19	0.10	0.12
		0.010	0.010	0.010	0.010	0.010	0.010	0.010	0.010	0.010	0.010
	4	0.06	0.12	0.07	0.15	0.06	0.12	0.08	0.18	0.07	0.14
		0.007	0.011	0.007	0.011	0.007	0.011	0.007	0.011	0.007	0.011
6	1	0.35	0.21	0.42	0.26	0.32	0.19	0.39	0.25	0.24	0.15
		0.010	0.006	0.010	0.006	0.010	0.006	0.010	0.006	0.010	0.006
	2	0.19	0.17	0.23	0.24	0.17	0.17	0.23	0.21	0.14	0.14
		0.008	0.006	0.008	0.006	0.008	0.006	0.008	0.006	0.008	0.006
	3	0.18	0.22	0.23	0.27	0.18	0.22	0.24	0.29	0.16	0.20
		0.010	0.010	0.010	0.010	0.010	0.010	0.010	0.010	0.010	0.010
	4	0.11	0.24	0.13	0.26	0.10	0.22	0.15	0.30	0.11	0.23
		0.007	0.011	0.007	0.011	0.007	0.011	0.007	0.011	0.007	0.011
5	1	0.58	0.35	0.67	0.40	0.50	0.31	0.59	0.36	0.33	0.21
		0.010	0.006	0.010	0.006	0.010	0.006	0.010	0.006	0.010	0.006
	2	0.32	0.29	0.39	0.34	0.29	0.27	0.36	0.32	0.21	0.19
		0.008	0.006	0.008	0.006	0.008	0.006	0.008	0.006	0.008	0.006
	3	0.33	0.37	0.40	0.44	0.32	0.35	0.38	0.43	0.24	0.27
		0.010	0.010	0.010	0.010	0.010	0.010	0.010	0.010	0.010	0.010
	4	0.19	0.37	0.23	0.44	0.19	0.35	0.24	0.44	0.15	0.29
		0.007	0.011	0.007	0.011	0.007	0.011	0.007	0.011	0.007	0.011
4	1	0.70	0.38	0.72	0.43	0.52	0.31	0.57	0.34	0.31	0.19
		0.010	0.006	0.010	0.006	0.010	0.006	0.010	0.006	0.010	0.006
	2	0.37	0.33	0.43	0.37	0.31	0.28	0.35	0.31	0.19	0.17
		0.008	0.006	0.008	0.006	0.008	0.006	0.008	0.006	0.008	0.006
	3	0.38	0.41	0.44	0.48	0.34	0.36	0.38	0.41	0.21	0.23
		0.010	0.010	0.010	0.010	0.010	0.010	0.010	0.010	0.010	0.010
	4	0.22	0.41	0.27	0.48	0.21	0.37	0.24	0.42	0.14	0.25
		0.007	0.011	0.007	0.011	0.007	0.011	0.007	0.011	0.007	0.011
3	1	0.80	0.48	0.87	0.52	0.61	0.36	0.65	0.38	0.34	0.21
		0.010	0.006	0.010	0.006	0.010	0.006	0.010	0.006	0.010	0.006
	2	0.47	0.41	0.53	0.45	0.37	0.32	0.40	0.34	0.20	0.18
		0.008	0.006	0.008	0.006	0.008	0.006	0.008	0.006	0.008	0.006
	3	0.50	0.53	0.56	0.59	0.41	0.43	0.44	0.46	0.22	0.25
		0.010	0.010	0.010	0.010	0.010	0.010	0.010	0.010	0.010	0.010
	4	0.30	0.53	0.34	0.59	0.25	0.43	0.28	0.47	0.15	0.26
		0.007	0.011	0.007	0.011	0.007	0.011	0.007	0.011	0.007	0.011
2	1	1.20	0.51	1.26	0.54	0.63	0.36	0.64	0.45	0.33	0.20
		0.010	0.006	0.010	0.006	0.010	0.006	0.010	0.006	0.010	0.006
	2	0.85	0.66	0.83	0.48	0.39	0.33	0.40	0.34	0.20	0.21
		0.008	0.006	0.008	0.006	0.008	0.006	0.008	0.006	0.008	0.006
	3	0.56	0.59	0.61	0.89	0.42	0.44	0.46	0.45	0.20	0.21
		0.010	0.010	0.010	0.010	0.010	0.010	0.010	0.010	0.010	0.010
	4	0.34	0.58	0.38	0.63	0.27	0.44	0.27	0.45	0.12	0.23
		0.007	0.011	0.007	0.011	0.007	0.011	0.007	0.011	0.007	0.011
1	1	1.91	1.09	1.86	1.07	1.17	0.67	1.13	0.67	0.52	0.32
		0.010	0.006	0.010	0.006	0.010	0.006	0.010	0.006	0.010	0.006
	2	1.16	0.96	1.14	0.95	0.70	0.59	0.63	0.54	0.25	0.23
		0.008	0.006	0.008	0.006	0.008	0.006	0.008	0.006	0.008	0.006
	3	1.24	1.26	1.21	1.23	0.75	0.76	0.67	0.68	0.26	0.28
		0.010	0.010	0.010	0.010	0.010	0.010	0.010	0.010	0.010	0.010
	4	0.77	1.24	0.77	1.23	0.47	0.76	0.42	0.69	0.17	0.29
		0.007	0.011	0.007	0.011	0.007	0.011	0.007	0.011	0.007	0.011

4.9 Results

4.9.1 Final asymmetries

The azimuthal asymmetries have been measured in 2016 periods 4–10. The final asymmetries A are calculated in each kinematic bin defined in section 4.4 as statistically-weighted averages of the asymmetries for both muon charges in the studied periods 4–10. Let us introduce the set P of pairs charge and period number to express the statistically-weighted average as a following equation:

$$A = \frac{\sum_{i\in P} A_i \sigma_{A_i}^{-2}}{\sum_{i\in P} \sigma_{A_i}^{-2}} . \tag{4.13}$$

Statistical uncertainity $\sigma_{A,\mathrm{stat}}$ is for each bin calculated using equation

$$\sigma_{A,\mathrm{stat}}^2 = \frac{1}{\sum_{i\in P} \sigma_{A_i}^{-2}} . \tag{4.14}$$

and the total error $\sigma_{A,\mathrm{tot}}$ follows the standard formula for statistical and systematical uncertainty[5] addition:

$$\sigma_{A,\mathrm{tot}} = \sigma_{A,\mathrm{stat}} \sqrt{1 + \frac{\sigma_{A,\mathrm{sv}}^2}{\sigma_{A,\mathrm{stat}}^2} + \frac{\sigma_{A,\mathrm{sp}}^2}{\sigma_{A,\mathrm{stat}}^2}} \tag{4.15}$$

The positions of the points on the abscissa of the final asymmetries were obtained in a similar way by calculating their mean value $\langle x\rangle$, $\langle P_T\rangle$, or $\langle z\rangle$ in each bin while considering all periods and both μ charges. The final asymmetries (with error bars reflecting the statistical error and a filled area representing the total error) are shown in the following figures 4.30-4.33.

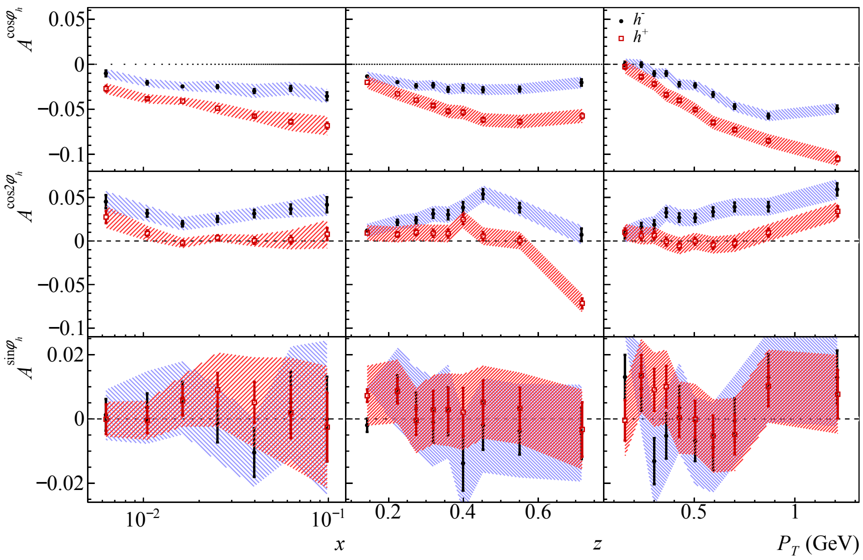

Figure 4.30: Azimuthal asymmetries for positive and negative hadrons in 1D binning

[5]Reminder of the used notation of systematic errors: contribution from the vertex incompatibility denoted $\sigma_{A,\mathrm{sv}}$ and contribution from the period incompatibility denoted $\sigma_{A,\mathrm{sp}}$

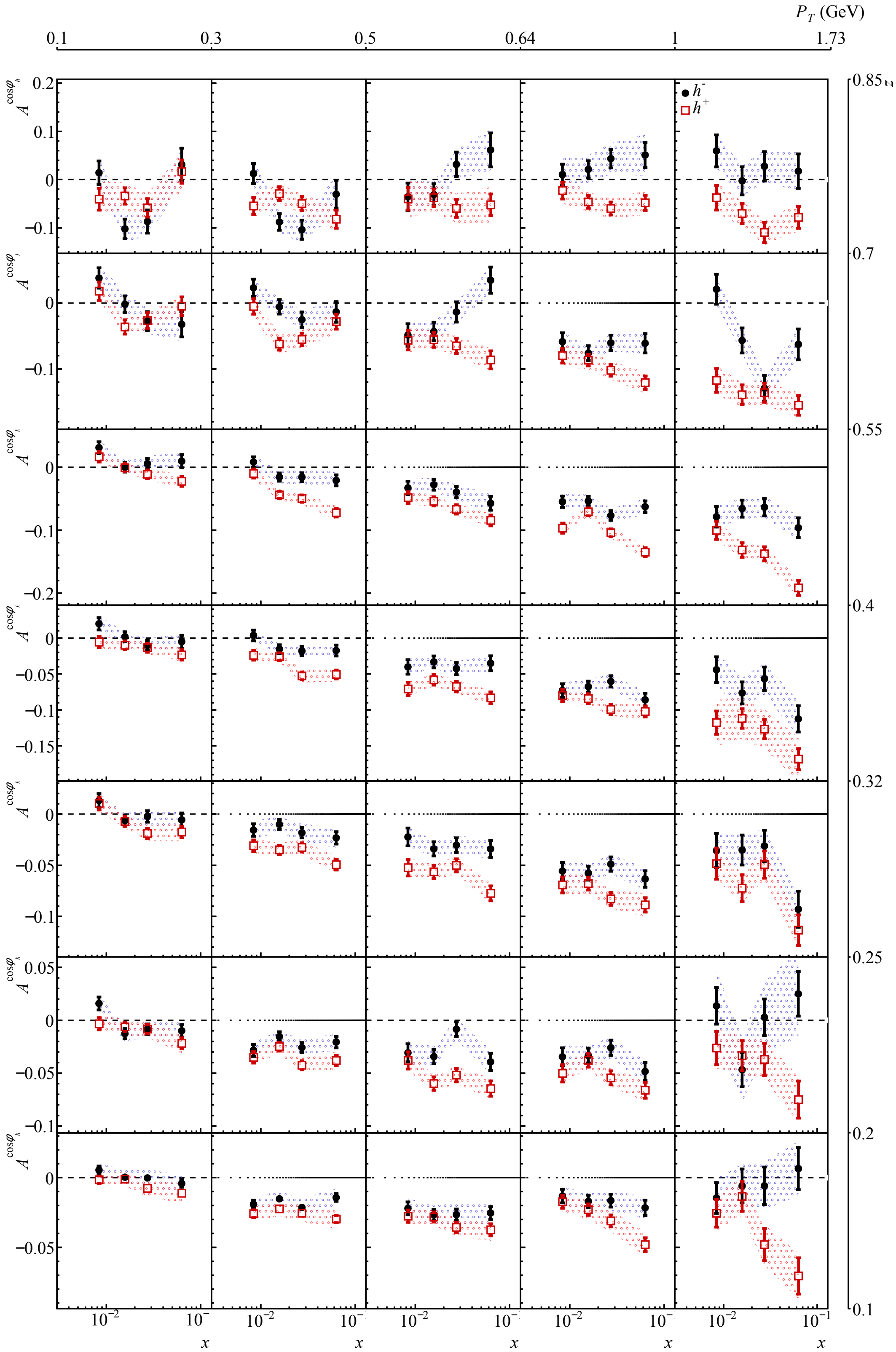

Figure 4.31: $A^{\cos\phi_h}$ for positive and negative hadrons in 3D binning

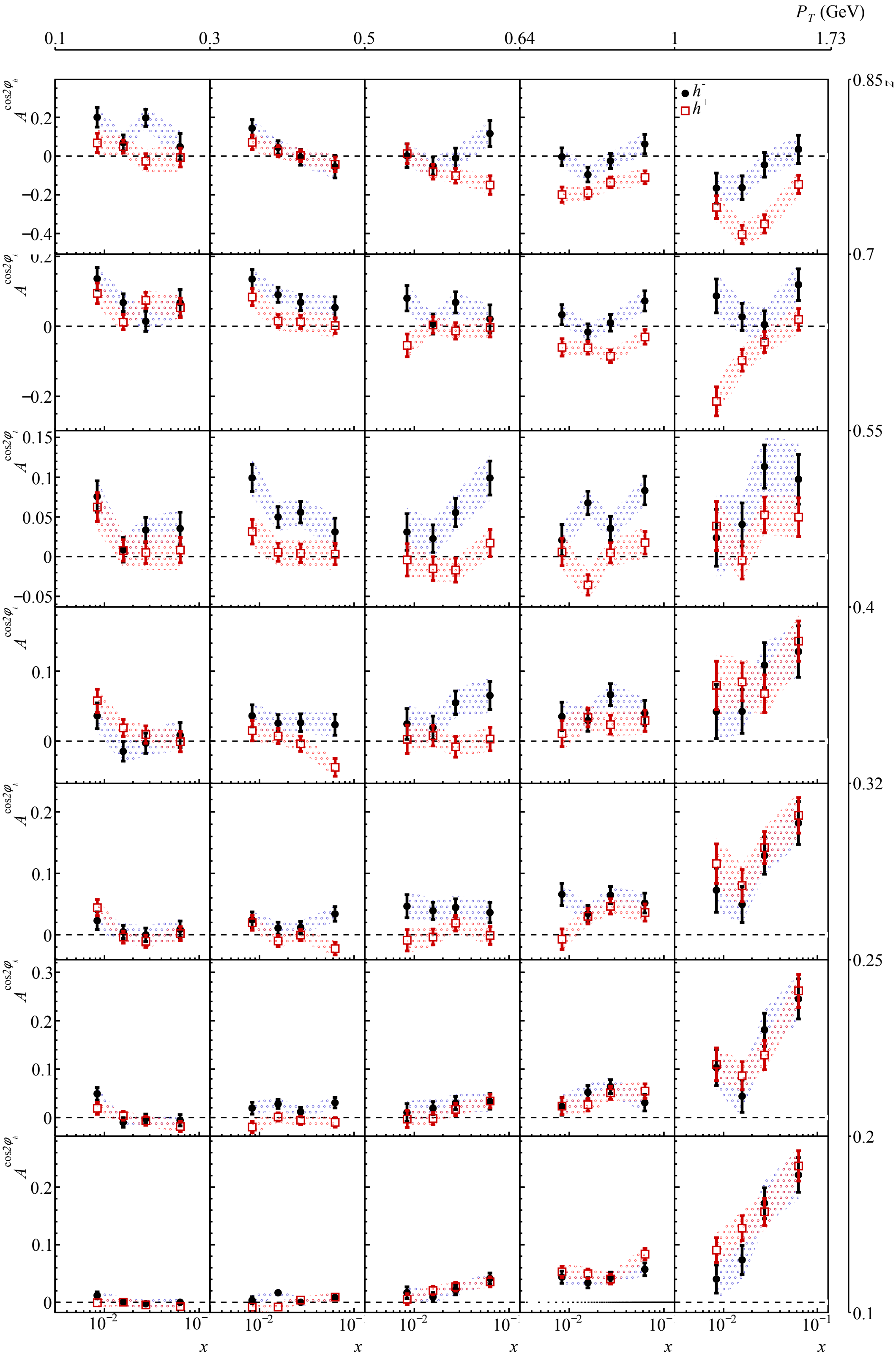

Figure 4.32: $A^{\cos 2\phi_h}$ for positive and negative hadrons in 3D binning

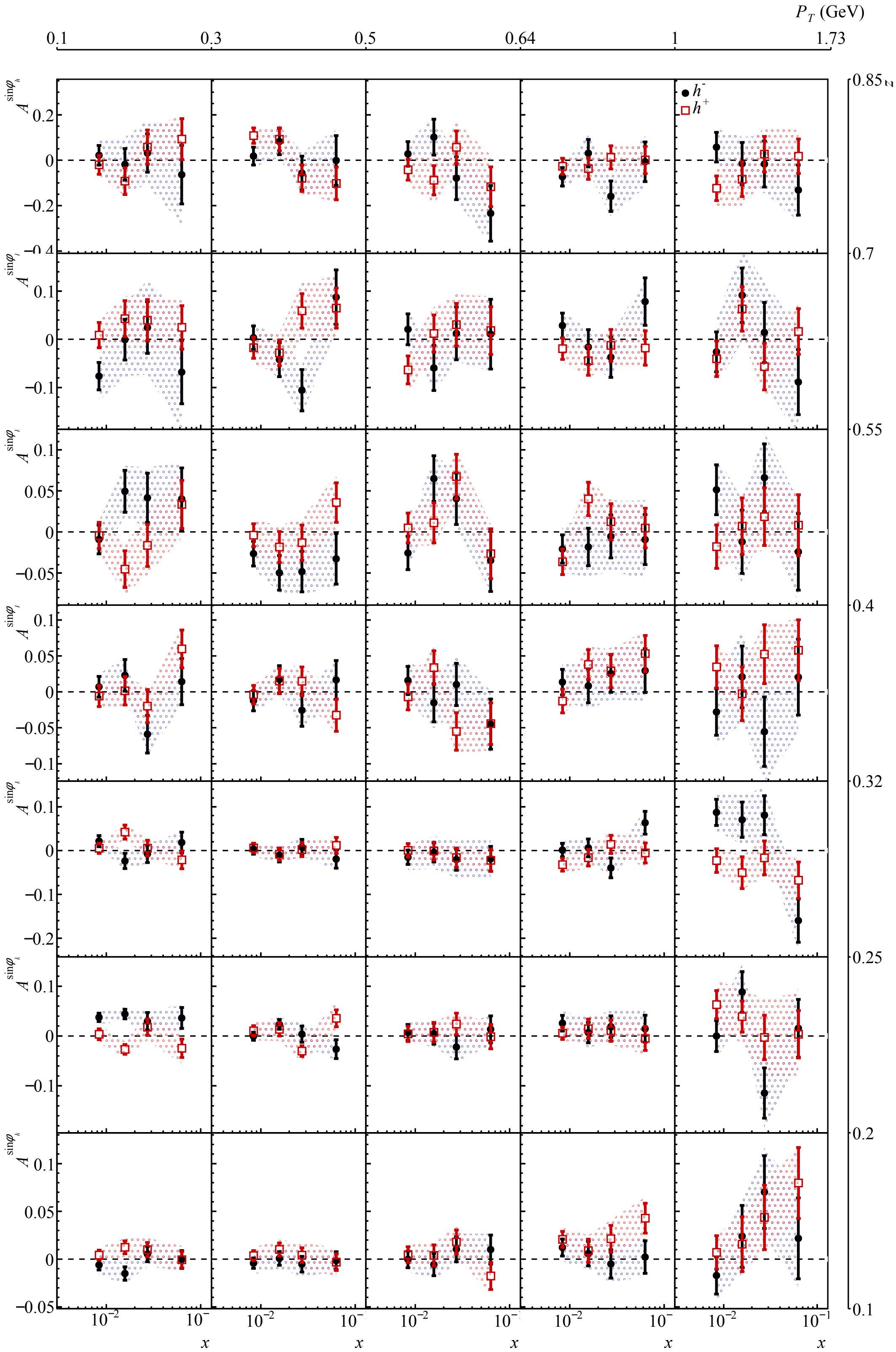

Figure 4.33: $A^{\sin\phi_h}$ for positive and negative hadrons in 3D binning

4.9.2 Comparison with previous results

Results presented in this thesis and preliminary results released by COMPASS collaboration in September 2020 were compared (can be found in [31]). The release note results accounted only for periods P08–P10 data of older production (slot 5) corrected on acceptance with older (*LEPTO* slot 5) production of MC. Compared final azimuthal asymmetries in 1D binning and 3D binning are in figures 4.34-4.41[6]. In this study, the statistics is roughly two times larger so the expected reduction in statistical error was estimated as 0.7. As acceptance correction also contributes to the statistical error, the factor is expected to be lower, because the statistic in the new MC samples improved. The results show good compatibility and the expected statistical error reduction. The statistical uncertainty reduction factor is about 0.5 in both 1D and 3D binning.

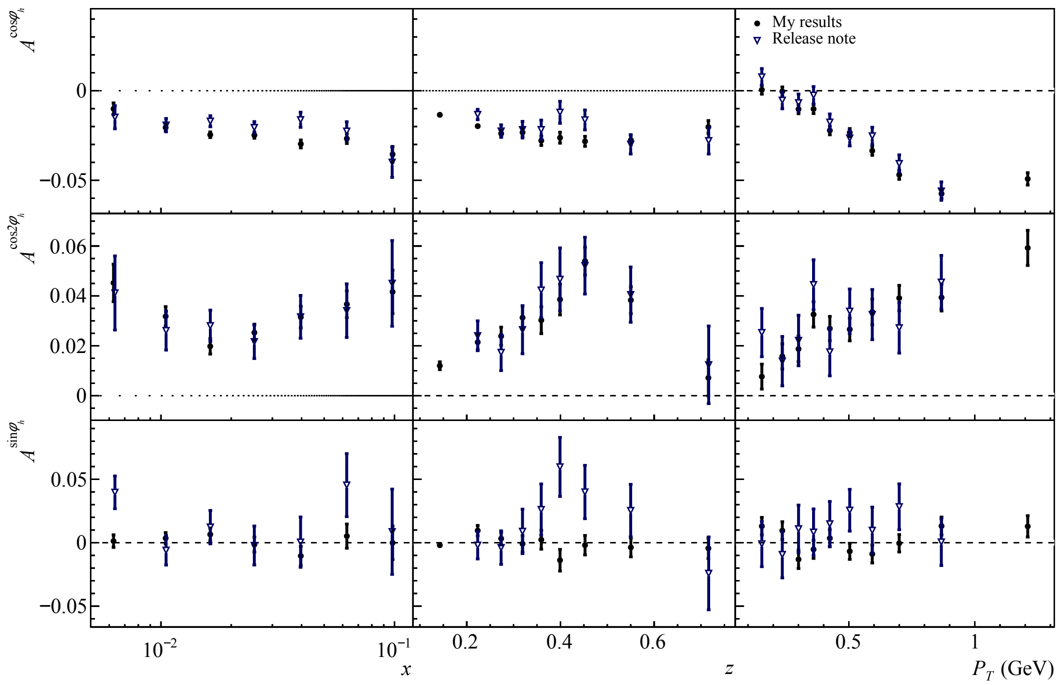

Figure 4.34: Azimuthal asymmetries for negative hadrons in 1D binning: comparison between 3D binning results of this thesis and September 2020 release note

[6]Note that the lowest z bin and the highest P_T bin were excluded from the analysis in the release note for being highly influenced by the acceptance.

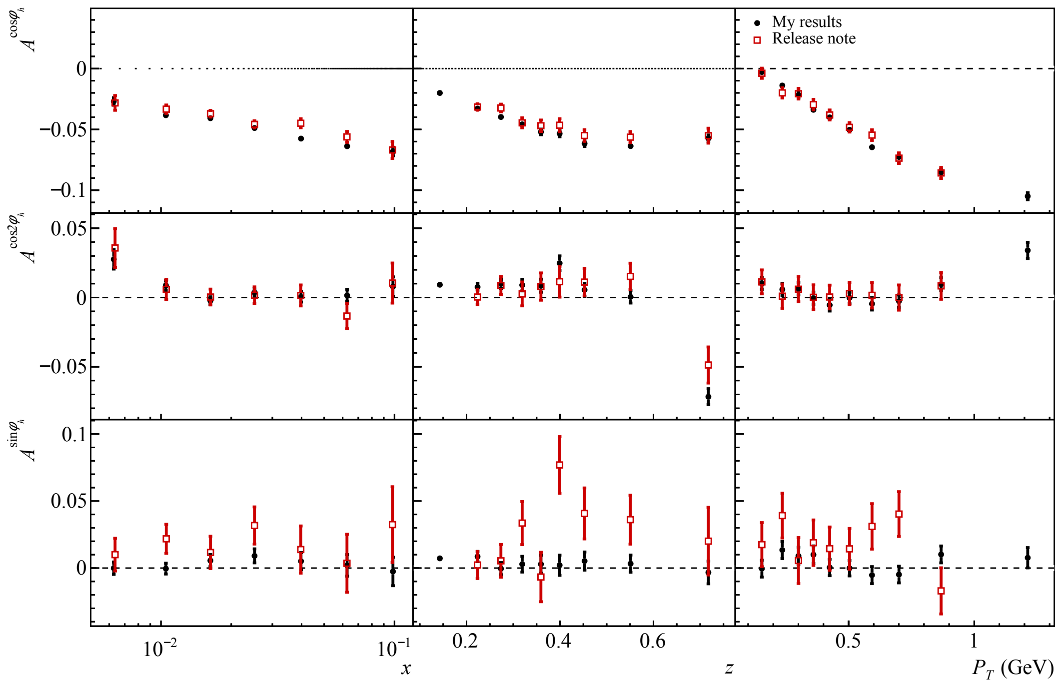

Figure 4.35: Azimuthal asymmetries for positive hadrons in 1D binning: comparison between 3D binning results of this thesis and September 2020 release note

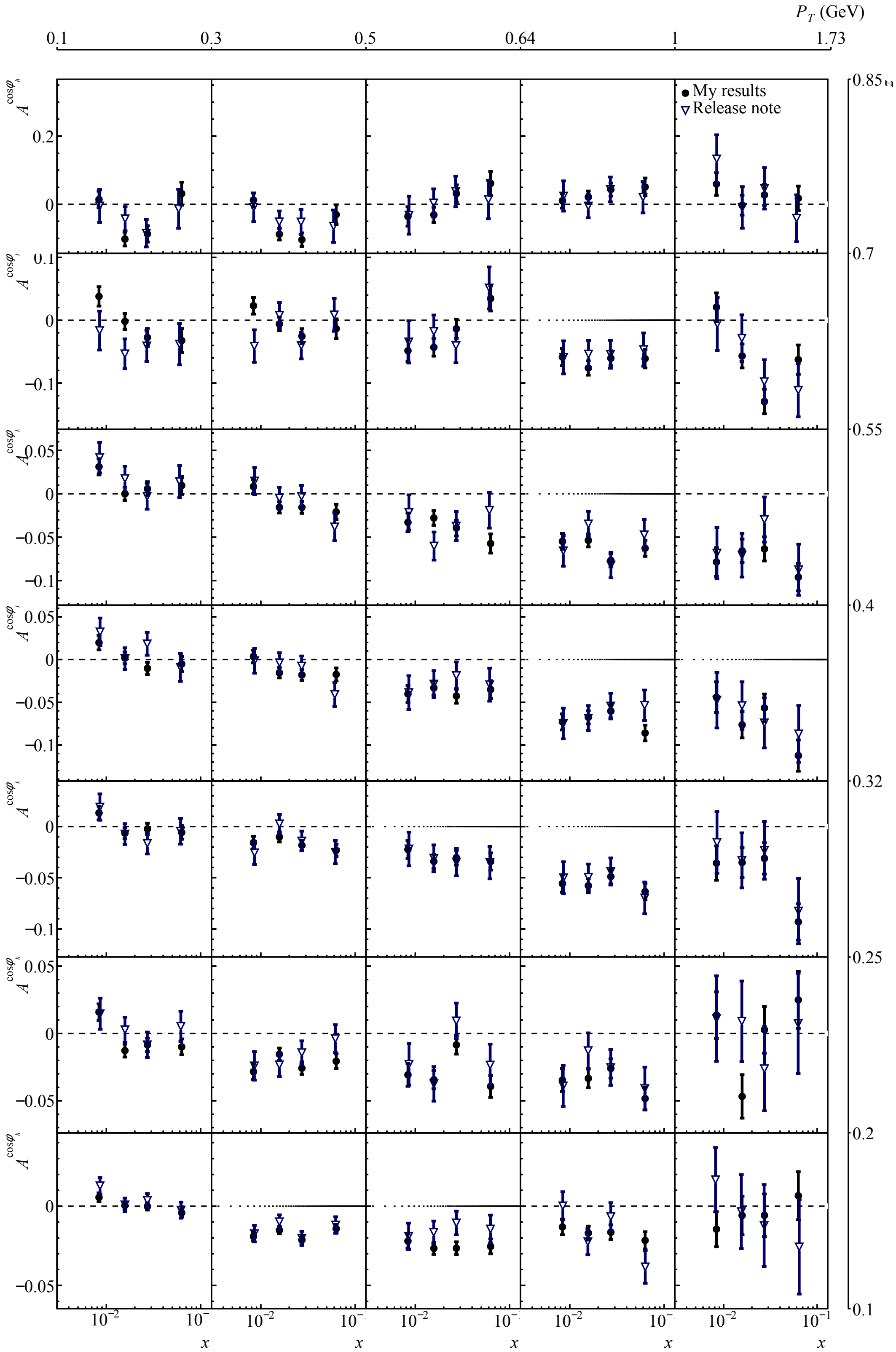

Figure 4.36: $A^{\cos\phi_h}$ for negative hadrons – comparison between 3D binning results of this thesis and September 2020 release note

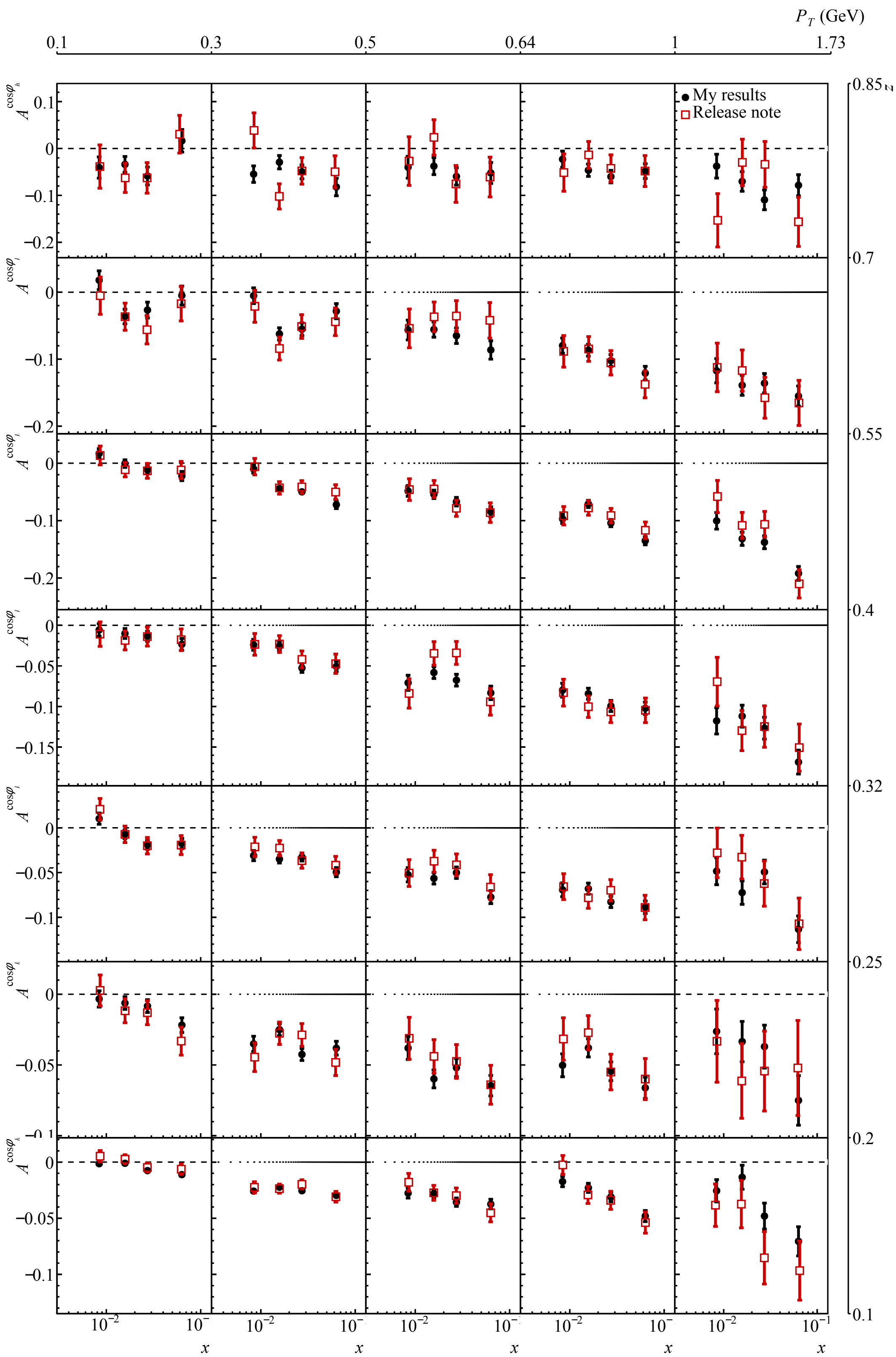

Figure 4.37: $A^{\cos\phi_h}$ for positive hadrons – comparison between 3D binning results of this thesis and September 2020 release note

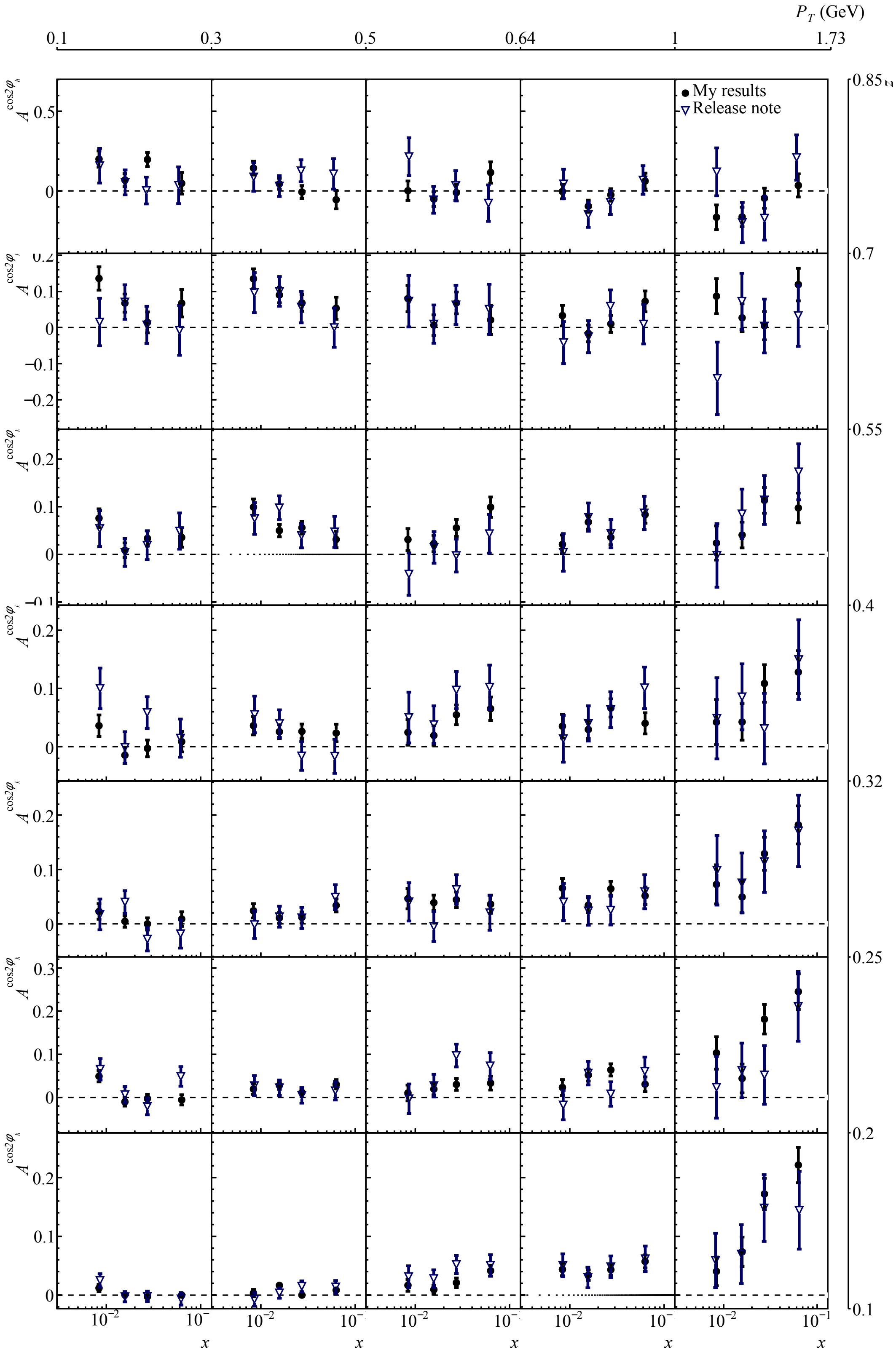

Figure 4.38: $A^{\cos 2\phi_h}$ for negative hadrons – comparison between 3D binning results of this thesis and September 2020 release note

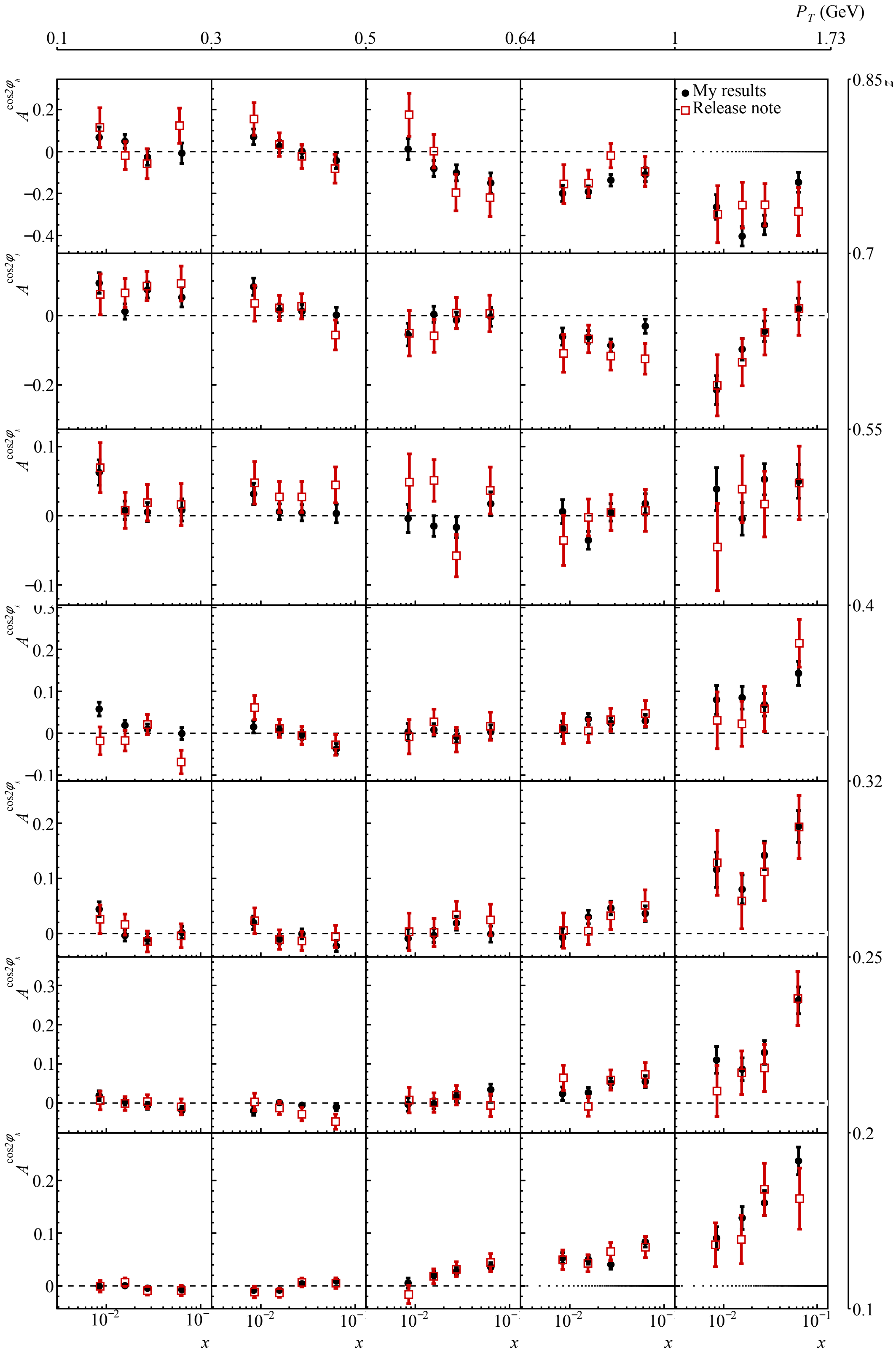

Figure 4.39: $A^{\cos 2\phi_h}$ for positive hadrons – comparison between 3D binning results of this thesis and September 2020 release note

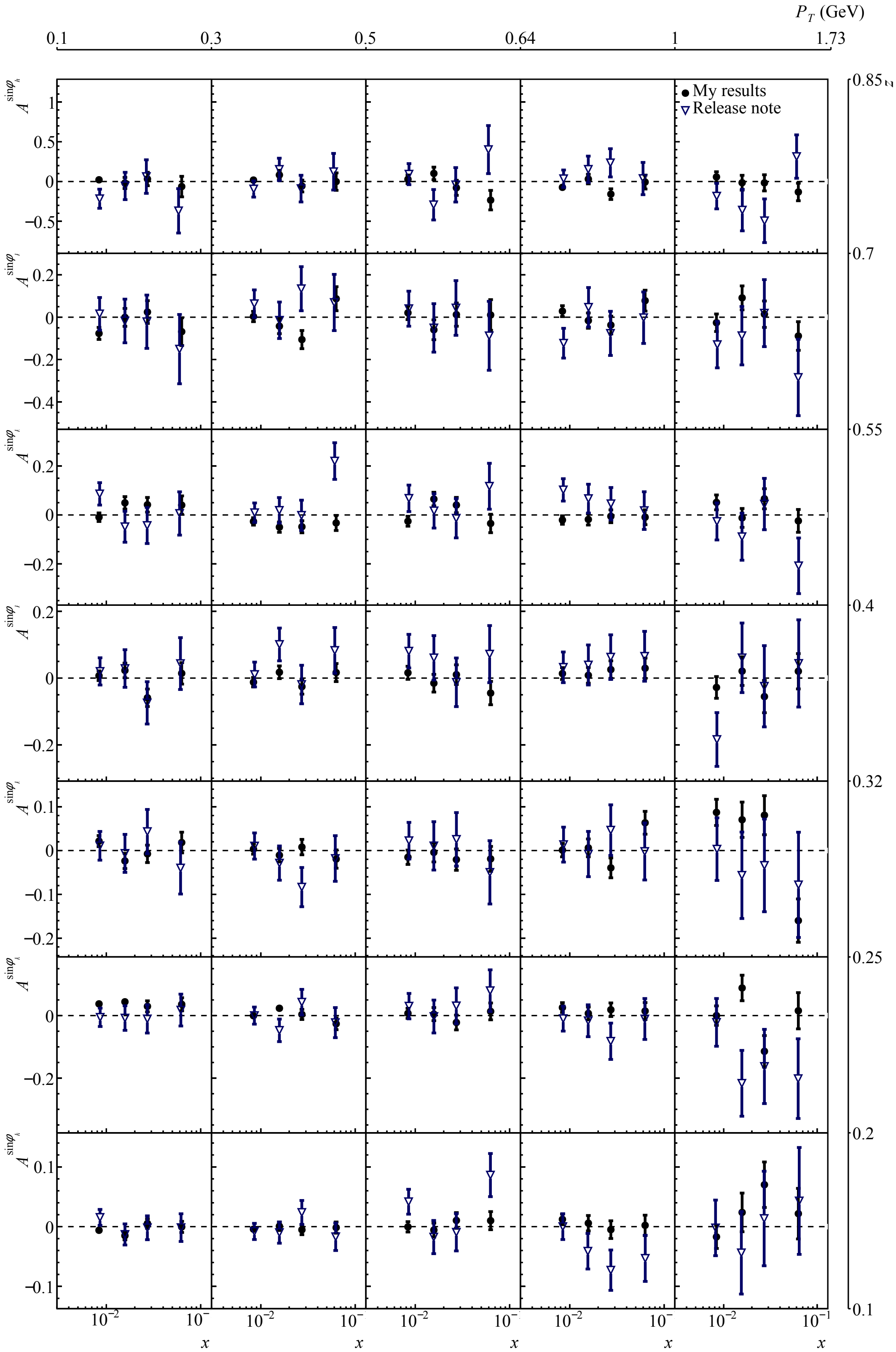

Figure 4.40: $A^{\sin\phi_h}$ for negative hadrons – comparison between 3D binning results of this thesis and September 2020 release note

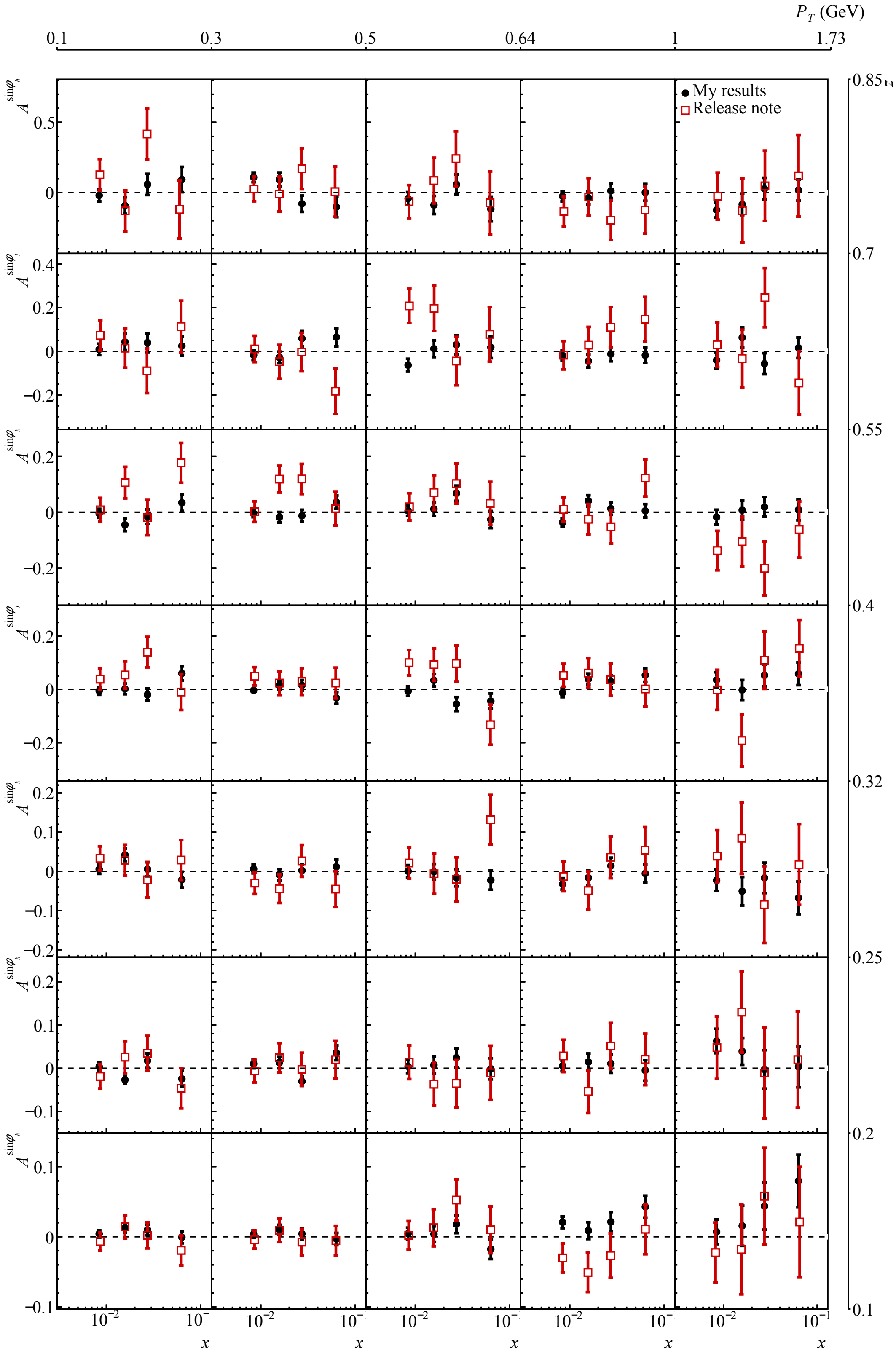

Figure 4.41: $A^{\sin\phi_h}$ for positive hadrons – comparison between 3D binning results of this thesis and September 2020 release note

Conclusion

We presented a brief introduction to the kinematics of the DIS and SIDIS, which included observable variables and conventions commonly used for the description of these processes. Introduction to the theory of the TMD-PDFs was given and specific examples of the functions involved in SIDIS off unpolarized target were introduced together with a way to obtain them from experimental measurements of azimuthal asymmetries. Specifically, *Boer-Mulders* function $h_1^\perp$ is dominant in the $\cos 2\phi_h$ modulation and thus can be extracted from measurements of $A^{\cos 2\phi_h}$. We also discussed the *Cahn* effect, which causes negative $\cos \phi_h$ modulation.

COMPASS experiment was designed to study the structure of nucleons by investigating data collected by a 60 m long two-staged spectrometer dedicated to HEMP, DVCS, and SIDIS measurements. In this thesis, the full COMPASS experimental setup was described with an emphasis on the setup of 2016–2017 for SIDIS off unpolarized liquid hydrogen target.

Extraction of the azimuthal asymmetries from the SIDIS measurements requires correcting the data in such a way, that they reflect only true physical SIDIS asymmetries. This process requires extensive use of MC simulations. When generating MC, information about incoming beam particle in the form of an ASCII beam file is required as input. The technical part of this thesis describes the extraction of the beam file and examines the beam parameters. Beam momentum and XY intensity were visualized to prevent selection mistakes within the beam file extraction. A comparison of the beam parameters with a report from 2004 was performed and no unreasonable differences were found. The work presented in this thesis indicates that the code for extracting beam file is ready to meet the needs of COMPASS collaboration for generating 2017 and 2022 beam files and MC samples.

Results of the 2016 data analysis, which consist of measurement of azimuthal asymmetries in SIDIS of muons off unpolarized protons, are presented in this thesis. As expected, the measured modulation of $\cos \phi_h$ was negative with a few exceptions in some low x and P_T bins. We also obtained a non-zero $\cos 2\phi_h$ modulation, which can be utilized for a potential extraction of *Boer-Mulders* function. We observed different values of $A^{\cos 2\phi_h}$ and $A^{\cos \phi_h}$ asymmetries for positive and negative hadrons, which can be interpreted as possible flavor dependence of $|\boldsymbol{k_T}|$. In most cases, zero $\sin \phi_h$ modulation was visible.

In further analysis, we focused on the estimation of systematic uncertainties and studied two systematic effects in detail: period incompatibility and incompatibility in vertex dependence. While the period incompatibility in 1D binning gave mostly reasonable contributions, which didn't overreach the size of statistical error, in some 3D bins the statistical error was overreached up to $\sigma_{A,\text{sp}} = 1.49\sigma_{A,\text{stat}}$. In multi-dimensional binning, worse period compatibility was observed in higher z bins, where the number of hadrons is generally lower thus larger fluctuations between periods are possible. However, the bigger problem was identified – large disagreement between asymmetries in vertex bins especially for $A^{\cos \phi_h}$ in higher x bins. According to the chosen expression, the contribution to the systematic error reached $\sigma_{A,\text{sv}} = 9.88\sigma_{A,\text{stat}}$ for the lowest z bin. Generally, a larger number of hadrons are produced with lower z thus the error obtained as an average over

x bins was high relative to the statistical error in the lower z bins. However, the overall contribution of the vertex incompatibility to the systematic error was high as inequality $\sigma_{A,\mathrm{sv}} < \sigma_{A,\mathrm{stat}}$ was rarely satisfied. The vertex incompatibility reflects how the MC samples correspond to reality. From the results of this thesis, we can conclude that current MC fails to reproduce the $\cos\phi_h$ modulation in the acceptance for charged hadrons. In fact, it seems that the MC generates a stronger $\cos\phi_h$ modulation in the acceptance, than the one observed in real data.

The final azimuthal asymmetries and their statistical uncertainties were compared to the results released by the COMPASS collaboration in September 2020. The comparison showed good compatibility and the expected statistical error reduction of 0.5.

Bibliography

[1] A.V. Belitsky and A.V. Radyushkin. Unraveling hadron structure with generalized parton distributions. *Physics Reports*, 418(1-6):1–387, 10 2005.

[2] The SLAC-MIT experiment, NobelPrize.org.

[3] J. Wan, , Ch. Tan, and Z. Lu. The cos2ϕ azimuthal asymmetry in $e^+e^- \to \pi^+\pi^-$ X process. *Phys. Lett. B*, 811:135884, 2020.

[4] X. Ji. Parton physics on a euclidean lattice. *Physical Review Letters*, 110(26), 06 2013.

[5] M. Diehl. Introduction to GPDs and TMDs. *The European Physical Journal A*, 52(6), 06 2016.

[6] J. Matousek. Azimuthal Asymmetries in Unpolarised Semi-Inclusive DIS at COMPASS. *JPS Conf. Proc.*, 37:020104, 2022.

[7] J. Chyla. Quarks, partons and Quantum Chromodynamics.

[8] W.S.C. Williams. *Nuclear and particle physics*. Oxford at the Clarendon, 1991.

[9] A. Bacchetta, M. Diehl, K. Goeke, A. Metz, P.J. Mulders, and M. Schlegel. Semi-inclusive deep inelastic scattering at small transverse momentum. *Journal of High Energy Physics*, 2007(02):093–093, 02 2007.

[10] V. Barone, M. Boglione, J. O. Gonzalez Hernandez, and S. Melis. Phenomenological analysis of azimuthal asymmetries in unpolarized semi-inclusive deep inelastic scattering. *Physical Review D*, 91(7), 04 2015.

[11] A. Moretti. *Study of the Transverse-Momentum-Dependent structure of the nucleon in Semi-Inclusive DIS*. PhD thesis, University of Trieste, 01 2021.

[12] S. Bhattacharya, K. Cichy, M. Constantinou, A. Scapellato A. Metz, and F. Steffens. Twist-3 partonic distributions from lattice QCD, 07 2021.

[13] C. Adolph et. al. Measurement of azimuthal hadron asymmetries in semi-inclusive deep inelastic scattering off unpolarised nucleons. *Nuclear Physics B*, 886:1046–1077, 09 2014.

[14] J. D. Bjorken. Asymptotic sum rules at infinite momentum. *Phys. Rev.*, 179:1547–1553, Mar 1969.

[15] S. Bastami, H. Avakian, A. V. Efremov, A. Kotzinian, B. U. Musch, B. Parsamyan, A. Prokudin, M. Schlegel, G. Schnell, P. Schweitzer, and K. Tezgin. Semi-inclusive deep-inelastic scattering in Wandzura-Wilczek-type approximation. *Journal of High Energy Physics*, 2019(6), 06 2019.

[16] R.N. Cahn. Azimuthal dependence in leptoproduction: A simple parton model calculation. *Physics Letters B*, 78(2):269–273, 1978.

[17] S. Melis V. Barone and A. Prokudin. Boer-mulders effect in unpolarized SIDIS: An analysis of the COMPASS and HERMES data. *Physical Review D*, 81(11), 06 2010.

[18] P. Abbon et al. The COMPASS experiment at CERN. *Nuclear Instruments and Methods in Physics Research Section A: Accelerators, Spectrometers, Detectors and Associated Equipment*, 577(3):455–518, 07 2007.

[19] I. Ludwig. *Azimuthal asymmetries and the Cahn effect at COMPASS*. PhD thesis, freiburg U., 2004.

[20] B. Adeva et. al. Measurement of the polarisation of a high energy muon beam. *Nuclear Instruments and Methods in Physics Research Section A: Accelerators, Spectrometers, Detectors and Associated Equipment*, 343(2):363–373, 1994.

[21] C. Bernet, A. Bravar, J. Hannappel, D.v. Harrach, R. Hermann, E. Kabuß, F. Klein, A. Korzenev, M. Leberig, M. Ostrick, J. Pretz, R. Windmolders, and J. Zhao. The compass trigger system for muon scattering. *Nuclear Instruments and Methods in Physics Research Section A: Accelerators, Spectrometers, Detectors and Associated Equipment*, 550(1):217–240, 2005.

[22] A. Vidon. *Probing the proton structure through deep virtual Compton scattering at COMPASS, CERN*. Theses, Université Paris Saclay (COmUE), 10 2019.

[23] P. Abbon et al. The COMPASS Setup for Physics with Hadron Beams. *Nucl. Instrum. Meth. A*, 779:69–115, 2015.

[24] L. Schmitt, H. Angerer, N. Franz, B. Grube, B. Ketzer, I. Konorov, R. Kuhn, W. Liebl, S. Paul, H. Fischer, A. Grunemaier, F.-H. Heinsius, K. Konigsmann, T. Schmidt, U. Fuchs, and M. Lamanna. The daq of the compass experiment. *IEEE Transactions on Nuclear Science*, 51(3):439–444, 2004.

[25] Y. Bai, M. Bodlak, V. Frolov, V. Jary, S. Huber, I. Konorov, D. Levit, J. Novy, D. Steffen, and M. Virius. Overview and future developments of the fpga-based DAQ of COMPASS. *Journal of Instrumentation*, 11(02):C02025, 02 2016.

[26] A. Edin G. Ingelman and J. Rathsman. LEPTO 6.5 — a monte carlo generator for deep inelastic lepton-nucleon scattering. *Computer Physics Communications*, 101(1-2):108–134, 04 1997.

[27] A. Sandacz and P. Sznajder. Hepgen - generator for hard exclusive leptoproduction, 2012.

[28] T. Szameitat. *New geant4-based Monte Carlo software for the COMPASS-II experiment at CERN*. PhD thesis, 01 2017.

[29] M. Diehl, T. Gousset, and B. Pire. Exclusive electroproduction of vector mesons and transversity distributions. *Physical Review D*, 59(3), 01 1999.

[30] J. Agarwalai et. al. Contribution of exclusive diffractive processes to the measured azimuthal asymmetries in SIDIS. *Nuclear Physics B*, 956:115039, 07 2020.

[31] A. Moretti. Azimuthal asymmetries in unpolarized semi-inclusive deep inelastic scattering at COMPASS. *Nuovo Cim. C*, 44(2-3):61, 2021.

List of Figures

List of Tables

List of Abbreviations

BMS Beam Momentum Station

CASTOR CERN Advanced STORage manage

CCC CERN Control Center

CERN European Organization for Nuclear Research (from the French 'Conseil Européen pour la Recherche Nucléaire')

COMPASS COmmon Muon Proton Apparatus for Structure and Spectroscopy

COOOL COMPASS Object-Oriented OnLine

CORAL COMPASS Reconstruction and AnaLysis

DAQ Data Acquisition System

DCs Drift Chambers

DCS Detector Control System

DIS Deep Inelastic Scattering

DVCS Deeply Virtual Compton Scattering

ECAL Electromagnetic CALorimeter

FPGAs Field Programmable Gate Arrays

GEMs Gas Electron Multipliers

GNS Gamma Nucleon System

GPDs Generalized Parton Distributions

HCAL Hadronic CALorimeter

HEMP Hard Exclusive Meson Production

IT Inner Trigger

LAS Large Angle Spectrometer

LAST Large Angle Spectrometer Trigger

LAT Large Area Trackers

LT Ladder Trigger

MC Monte Carlo

mDSTs mini Data Summary Trees

MF Muon Filter

Micromegas Micromesh Gaseous Structures

MIT Massachusetts Institute of Technology

MT Middle Trigger

MW Muon Wall

MWPCs Multi-Wire Proportional Chambers

OT Outer Trigger

PHAST PHysics Analysis Software Tools

QCD Quantum ChromoDynamics

RICH Ring Imaging CHerenkov

RPD Recoil Proton Detector

SAS Small Angle Spectrometer

SAT Small Area Trackers

SciFi Scintillating Fibre

SIDIS Semi-Inclusive Deep Inelastic Scattering

SLAC Stanford Linear Accelerator Center

SM Spectrometer Magnet

SPS Super Proton Synchrotron

SW Straw Tube Drift Chambers

TiS Time in Spill

TMDs Transverse Momentum Dependent functions - referring to TMD-PDFs and TMD-FFs

TMD-FFs Transverse Momentum Dependent Fragmentation Functions

TMD-PDFs Transverse Momentum Dependent Parton Distribution Functions

uDSTs micro Data Summary Trees

VSAT Very Small Area Trackers